Thermal Properties of Nanowires and Nanotubes: Modeling and Experiments

by

Christopher Eric Dames

M.S., Mechanical Engineering (2001)
University of California, Berkeley

B.S., Mechanical Engineering (1998)
University of California, Berkeley

Submitted to the Department of Mechanical Engineering
in Partial Fulfillment of the Requirements for the Degree of
Doctor of Philosophy in Mechanical Engineering

at the
Massachusetts Institute of Technology
June 2006

Signature of Author...
Department of Mechanical Engineering
May 19, 2006

Certified by...
Gang Chen
Professor of Mechanical Engineering
Thesis Supervisor

Accepted by...
Lallit Anand
Chairman, Department Committee on Graduate Students

Thermal Properties of Nanowires and Nanotubes: Modeling and Experiments

by

Christopher Eric Dames

Submitted to the Department of Mechanical Engineering on May 19, 2006
in Partial Fulfillment of the Requirements for the Degree of
Doctor of Philosophy in Mechanical Engineering

Abstract

Nanowires and nanotubes have drawn a great deal of recent attention for such potential applications as lasers, transistors, biosensors, and thermoelectric energy converters. Although the thermal properties of nanowires can differ greatly from their bulk counterparts, the theoretical and experimental understanding of these differences is still limited. Thermal performance is especially important for nanowire thermoelectrics, which are expected to have energy conversion efficiencies far superior to bulk materials. This efficiency increase may lead to a broad range of applications for reliable, solid-state energy conversion, including household refrigeration and waste heat scavenging for power generation.

In this thesis, the fundamental thermal properties of nanowires and nanotubes are explored from both theoretical and experimental perspectives. Modeling and experiments on titanium dioxide nanotubes confirm that quantum size effects can cause enhancements in the specific heat at low temperature, while modeling of classical size effects in nanowires and superlattice nanowires shows that the thermal conductivity can be reduced by several orders of magnitude compared to bulk, in agreement with available experimental data. To facilitate further experimental studies of individual nanowires, the "3-omega" methods for thermal properties measurements were made more rigorous, simpler to implement, and generalized to 1-omega and 2-omega methods which may be advantageous for nanoscale systems. These methods are used to deduce the thermal properties of a system from its electrical response at the first, second, or third harmonic of a driving current. Finally, a detailed design and preliminary measurements are presented for a new type of hot-wire probe based on Wollaston wire and used to measure the thermoelectric properties of individual nanowires and nanotubes inside a transmission electron microscope.

Thesis Supervisor: Gang Chen
Title: Professor of Mechanical Engineering

Acknowledgements

This Ph.D. thesis marks an important milestone on a long and continuing journey, and I owe a great deal to the many people who have helped along the way. There is only room to briefly thank a few of them here.

Working with my thesis adviser, Prof. Gang Chen, has been a wonderful experience. There is much that I hope to emulate about his approach to research: not only his superb technical skills but also his open mind and positive spirit. I am also grateful for the encouragement and guidance of the other members of my thesis committee, Prof. John H. Lienhard V and the remarkable Prof. Mildred S. Dresselhaus.

I have benefited both technically and personally from half a decade of interactions with my labmates at MIT, particularly C. Thomas Harris, Hohyun Lee, Arvind Narayanaswamy, Aaron Schmidt, and Prof. Ronggui Yang, as well as the other graduate students, postdocs, and visitors to our lab who have made my PhD experience rich and challenging in many dimensions.

My fledgling academic identity was shaped in many ways by six years in Berkeley, California, and I would like to acknowledge Prof. Robert Dibble, Prof. Ralph Greif, Prof. George Johnson, Dr. Rajiv Mongia, Joe and Joyce Shumate, and especially Prof. Arun Majumdar and my former colleagues in his lab.

I also have had the good fortune to collaborate with several other research groups at MIT and Boston College during my PhD years. I learned a great deal both technically and professionally while working under the guidance of Prof. Henry I. Smith and Prof. Karl Berggren in the NanoStructures Lab (NSL). Dr. Fernando Castaño, Jim Daley, Mark Mondol, Dr. Tim Savas, Dr. Mike Walsh, and Dr. Feng Zheng were particularly helpful, and I enjoyed the stimulating partnership with Brian Cord. The Physics Department at Boston College has been like a second academic home for me. I am grateful for the crash course in low-temperature experimental physics provided by Prof. Michael Naughton, Prof. Cyrus Opeil, Dr. J. I Oh, and Yong Sun, and the many long experimental runs shared with the ever-cheerful Bed Poudel. I also have benefited greatly from ongoing collaboration with Prof. Zhifeng Ren and Dr. Shuo Chen, without whom this thesis would be missing its last chapter.

Finally, to my parents, my grandparents, my sister, and Dorothy: thank you for your support, encouragement, and love.

Table of Contents

List of Figures

List of Tables

Chapter 1: Introduction

Nanowires and nanotubes have attracted a great deal of attention in recent years. The initial research focused on the synthesis of many varieties of these remarkable structures, including single-walled [1,2] and multi-walled [3] carbon nanotubes with diameters down to about one nm [4, 5], as well as nanowires with diameters typically ranging from 10-100 nm and morphologies that can be homogeneous [6], segmented [7-10], or core-and-shell [11]. The electrical, optical, mechanical, and thermal properties of these small structures can differ from bulk materials in many exciting ways [12, 13]. Consequently, nanowires and nanotubes have proven to be fertile areas for fundamental studies of nanoscience. The extraordinary properties of nanowires and nanotubes make them appealing for a broad range of technological applications (Fig. 1-1), including non-volatile memory [14, 15], biosensors [16], lasers [17, 18], dye-sensitized (Grätzel) solar cells [19, 20], and thermoelectric energy conversion [21-23], and there are high hopes that some of these applications may be commercialized within a decade. This chapter introduces some of the unique physical properties of nanowires and nanotubes and their potential applications. Of particular interest are nanowire-based thermoelectric devices, which can be used for the direct conversion of heat to electricity, with no fluids or moving parts.

1.1 Nanowires and nanotubes

The unique physical properties of nanowires and nanotubes can be divided into at least four different categories, listed in order of increasingly interesting and challenging physics: smaller size, the increased importance of surfaces and interfaces, classical / particle size effects, and quantum / wave size effects (Fig. 1-2).

(a) Smaller size

The most obvious benefit of making devices from nanowires and nanotubes is that more devices can be packed in a given area or volume [Fig. 1-2(a)]. Although this phenomenon does not invoke any exotic physics, it is important for most nanowire and nanotube devices, including non-volatile memory, biosensors, and lasers [Figs. 1-1(a-c)]. Nanowires and nanotubes may even permit Moore's law (governing the rate of progress in manufacturing transistors of ever-smaller size) to scale to dimensions smaller than the current limits of photolithography, an application with the potential for tremendous economic impact.

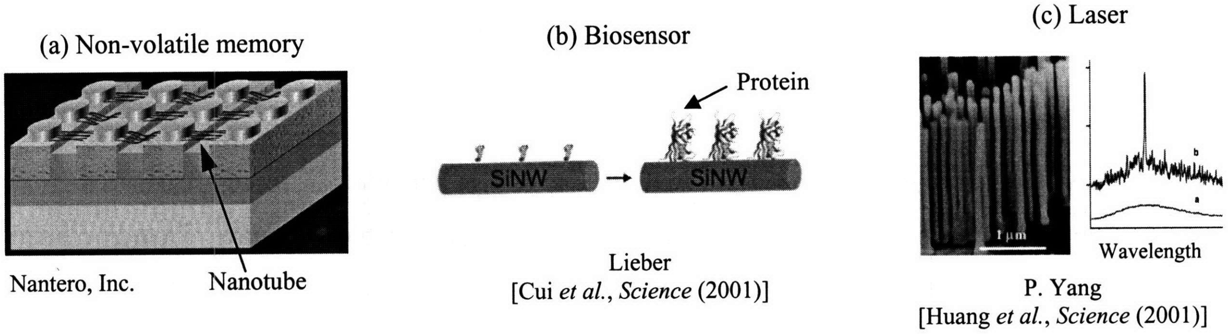

(a) Non-volatile memory

Nantero, Inc.

(b) Biosensor

Lieber
[Cui *et al.*, *Science* (2001)]

(c) Laser

P. Yang
[Huang *et al.*, *Science* (2001)]

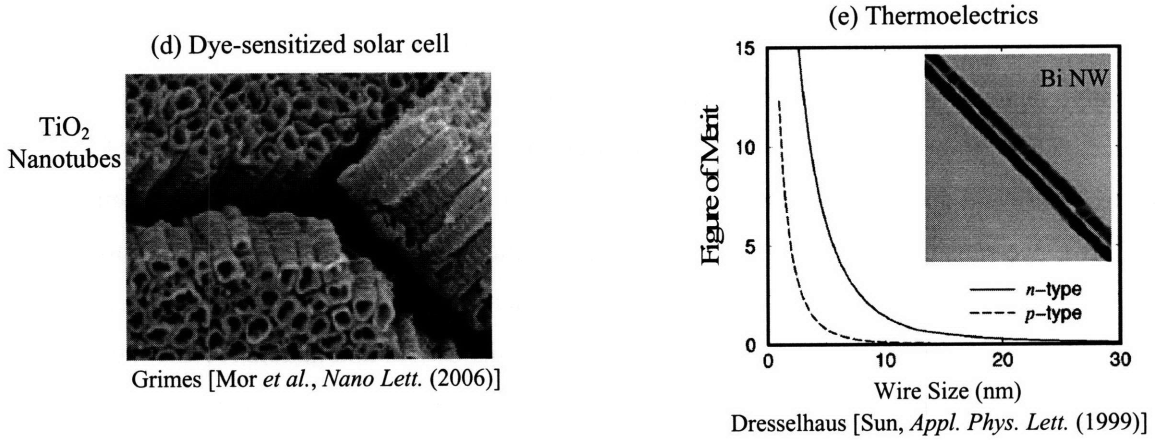

(d) Dye-sensitized solar cell

Grimes [Mor *et al.*, *Nano Lett.* (2006)]

(e) Thermoelectrics

Dresselhaus [Sun, *Appl. Phys. Lett.* (1999)]

Figure 1-1. Examples of devices made with nanowires and nanotubes.

(b) Increased importance of surfaces

The ratio of surface area to volume increases as the characteristic length scale is reduced [Fig. 1-2(b)]. For example, the ratio of surface area to volume for a nanowire of diameter D and length L (with $L >> D$) is proportional to the inverse of the diameter. Thus, the surfaces of a nanowire with 10 nm diameter can in some sense be considered 10,000 times more important than a conventional wire of 100 μm diameter. This scaling places relatively more emphasis on the surface properties compared to bulk properties, which is particularly important for such applications as sensing, catalysis, and dye-sensitized (Grätzel) solar cells [Figs. 1-1(b,d)].

(c) Classical / particle size effects

As nanowires and nanotubes are made smaller, their characteristic length may become comparable to, or smaller than, the mean free path of the fundamental carriers of charge, mass, energy, etc. This "classical" (or "particle") size effect is analogous to rarified gas flow inside a tube, except that

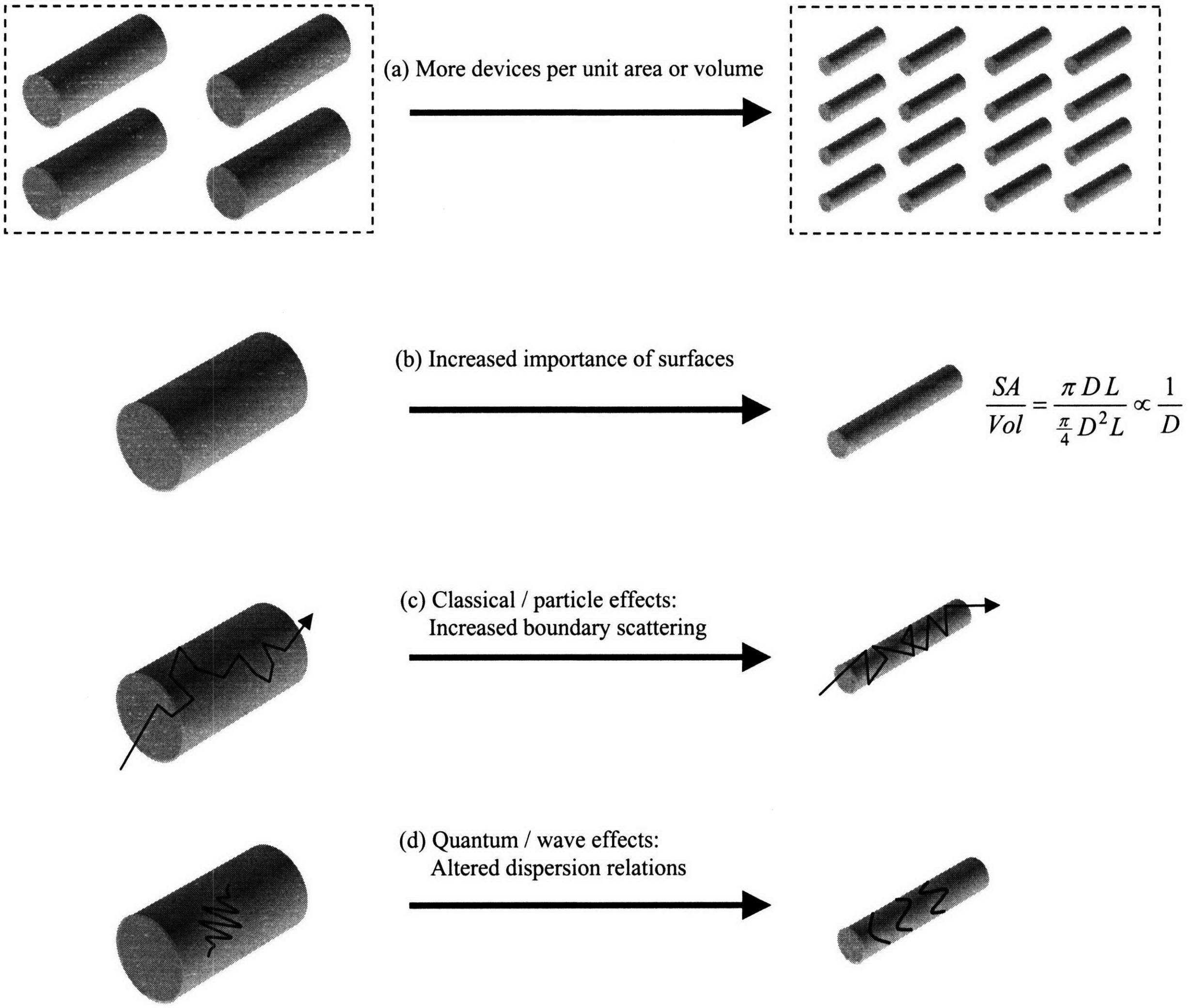

Figure 1-2. Size effects when shrinking large wires down into nanowires.

in most solids of interest the carriers are not gas molecules but rather electrons or phonons (the quanta of sound waves). In the classical regime the electrons and phonons can still be treated as point particles. The thermal conductivity of such a collection of particles can be understood using kinetic theory,

$$k = \tfrac{1}{3} C v L_{eff} \tag{1-1}$$

which states that the thermal conductivity is proportional to the specific heat per unit volume, C, the velocity of the particles, v, and the effective mean free path of the particles between collisions, L_{eff}. If the phonons are constrained inside a nanostructure, the classical size effect of increased scattering at the boundaries and interfaces tends to impede transport [Fig. 1-2(c)]. For example, in bulk silicon at 300 K, the mean free paths of most phonons are in the range of 100 nm to 10 μm, so phonons in a silicon nanowire of 50 nm diameter will experience greatly increased scattering due to collisions with the rough sidewalls. The reductions in mean free path due to boundary scattering can be understood approximately using Matthiessen's rule,

$$L_{eff}^{-1} = L_{bulk}^{-1} + L_{boundary}^{-1} \tag{1-2}$$

which shows how boundary scattering reduces the effective mean free path compared to purely bulk scattering mechanisms. The boundary scattering mean free path for a rough-walled nanowire is simply the diameter [24]. An additional boundary scattering effect is important for samples of finite length, including carbon nanotubes [25] and macro-sized cylinders [26]. Although Matthiessen's rule is rarely exactly correct, it is widely used to capture the essential physics of the increased scattering when multiple scattering mechanisms are active [27, 28].

Equations (1-1) and (1-2) show that boundary scattering in nanostructures reduces the mean free path and thus the thermal conductivity. In most applications this increased boundary scattering introduces potentially serious problems in thermal management because of the increased heat generation and reduced thermal conductivity [Fig. 1-1(a-d)], but in thermoelectric applications the reduced thermal conductivity is actually very helpful [Fig 1-1(e)] [12, 21-23]. It should also be noted that the bulk scattering mechanisms and boundary scattering mechanisms may be manipulated somewhat independently, because they have different dependencies on temperature, material properties, and geometry.

(d) Quantum / wave size effects

Nanowires and nanotubes can also be made so small as to be comparable to or even smaller than the wavelength of the fundamental energy carriers [Fig. 1-2(d)]. This "quantum" (or "wave") size effect is closely related to the interference of light in thin-film optics, and also the guiding of electromagnetic waves in optical fibers and microwave waveguides, because in all of these cases the wave nature of the energy carrier (phonon, electron, photon, or atom/molecule [29]) is essential to understanding its behavior inside the host structure. These quantum confinement effects can change the dispersion relations, the relationship between energy and wavelength. For example, the bandgap of electrons in a nanowire may be increased compared to a bulk material [30], potentially allowing the wavelength of nanowire lasers [Fig. 1-1(c)] to be tuned by synthesizing nanowires of different diameters. Quantum confinement can also introduce sharp features in the electron density of states, with potentially beneficial impacts on the thermoelectric performance [Fig. 1-1(e)] [12, 21-23]. Quantum confinement is also important for the phonon specific heat, which may be increased or decreased compared to bulk depending on whether the boundary conditions are free or fixed [31-33]. Broadly speaking, quantum confinement becomes a new variable to tailor the properties of materials in many exciting ways that are simply not possible in bulk, three-dimensional systems.

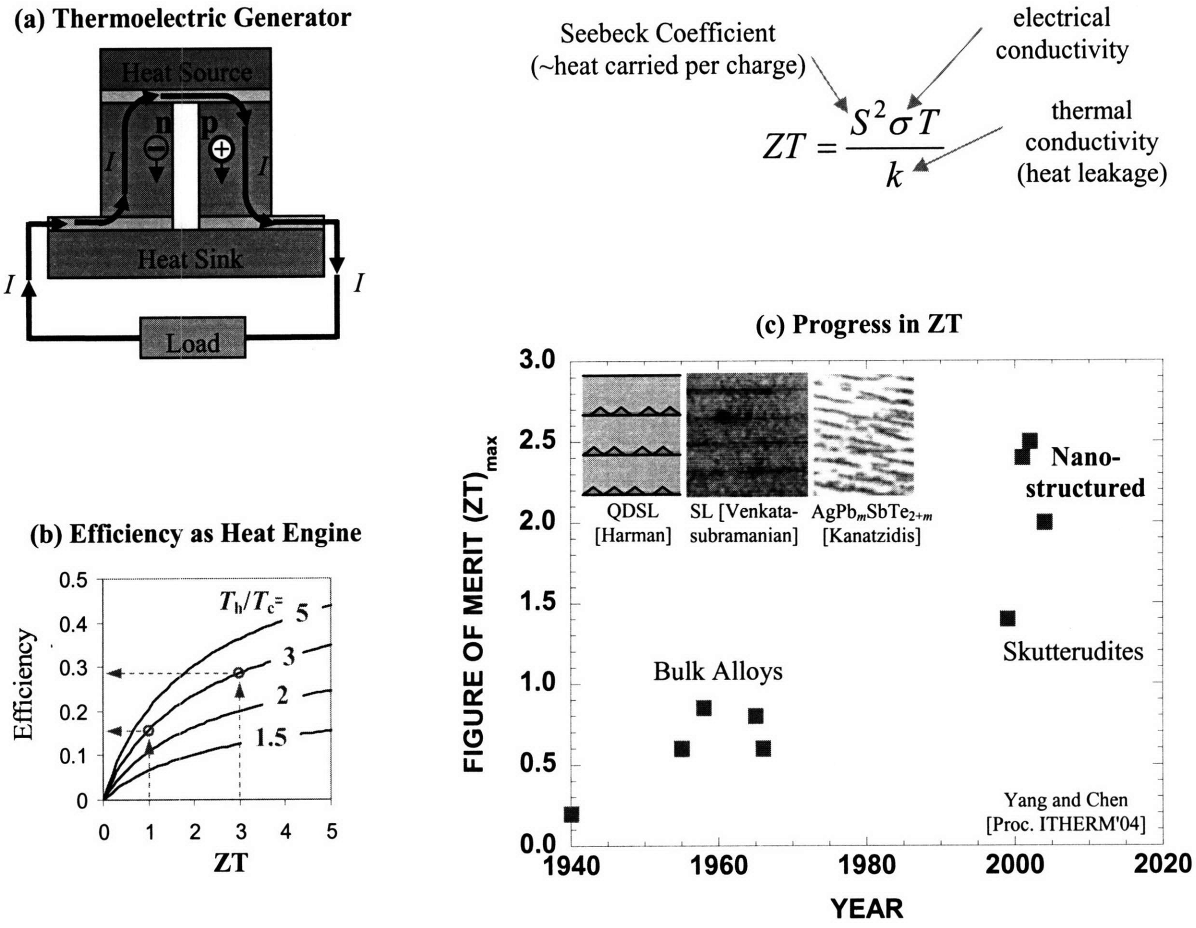

Figure 1-3. Thermoelectric devices and their performance. (a) Thermoelectric generator. (b) Efficiency as a function of temperature and ZT. (c) 65 years of progress in ZT [39].

1.2 Thermoelectricity in low-dimensional structures

At the heart of all thermoelectric phenomena is the coupling between heat and electricity [34-36]. The most familiar example is a thermocouple, where the open circuit voltage of a junction between two dissimilar conductors is determined by the temperature of the junction. If instead of open-circuit operation, the thermocouple is allowed to do work across an electrical load, then the device operates as a thermoelectric heat engine [Fig. 1-3(a)]. Alternatively, if the load is replaced with an electrical power source to reverse the current flow, then the device operates as a refrigerator or heat pump.

Compared to traditional refrigerators and heat engines, thermoelectric energy converters have the advantages of simplicity, reliability, and no vibrations. Furthermore, because they use no refrigerants or working fluids, thermoelectric devices may be expected to have negligible direct emissions of greenhouse gases over their lifetime, likely reducing their contribution to global warming compared to conventional technologies [37]. The greatest disadvantage of thermoelectric energy converters is their low efficiency and high cost. Therefore, applications are currently limited to certain niches, including power generation for deep space probes [35, 38], seat warmers and coolers for luxury automobiles, and temperature control of some laboratory equipment.

The efficiency of a thermoelectric generator operating between absolute temperatures T_h (hot side) and T_c (cold side) is given by

$$\eta = \left(1 - \frac{T_c}{T_h}\right)\left(\frac{\sqrt{1+Z\bar{T}} - 1}{\sqrt{1+Z\bar{T}} + T_c / T_h}\right) \tag{1-3}$$

where $\bar{T}$ is the average temperature and ZT is the dimensionless figure of merit, discussed below [34, 35]. The second term in parentheses is always less than unity, showing that the efficiency for thermoelectric energy conversion can never exceed the fundamental thermodynamic limit of the Carnot efficiency (the first term in parentheses). This efficiency function is depicted in Fig. 1-3(b) for several values of T_h / T_c.

The derivation of Eq. (1-3) reveals that ZT depends on several underlying material properties [34, 35]:

$$ZT = \frac{S^2 \sigma T}{k_e + k_p}. \tag{1-4}$$

Here S the Seebeck coefficient, σ the electrical conductivity, and k_e and k_p the electron and phonon contributions to the thermal conductivity, respectively. A material with good efficiency for thermoelectric energy conversion will have: a large Seebeck coefficient, to optimize coupling between thermal and electrical energy; a large electrical conductivity, to minimize resistive losses; and a low thermal conductivity, to minimize the parasitic heat leakage by conduction from hot to cold sides. However, it is important to recognize that σ and k_e are closely coupled in most materials through the Wiedemann-Franz law:

$$\frac{k_e}{\sigma T} = L_0. \tag{1-5}$$

Here L_0 is the Lorentz number which is typically around 2 x 10^{-8} to 3 x 10^{-8} V^2/K^2 (or $\sqrt{L_0} \approx 140$-170 μV/K) for bulk materials at room temperature [28], although in semiconductors the Lorentz number depends on doping. The figure of merit can then be expressed as

$$ZT = \frac{\left(S/\sqrt{L_0}\right)^2}{1 + k_p/k_e}. \tag{1-6}$$

		Quantum Dot Superlattice PbSeTe / PbTe [Harman *et al.*]		Superlattice Bi_2Te_3 / Sb_2Te_3 [Venkatasubramanian *et al.*]	
		Bulk	Nanostructure	Bulk	Nanostructure
ZT (at 300 K)		0.36	1.6	1.0	2.4
Power Factor, $S^2\sigma$	[μW / cm K^2]	24	34	35	40
Thermal conductivity, k	[W / m K]	2.0	0.6	2.0	0.5

Table 1-1. Thermoelectric properties of two superlattice material systems with high ZT [40, 41].

Compared to Eq. (1-4), this form breaks ZT into two different dimensionless groups and shows that the criterion for a "small" phonon thermal conductivity is to compare it to the electron thermal conductivity.

More than 60 years of progress in ZT are summarized briefly in Fig. 1-3(c) [39]. Traditional bulk thermoelectric materials include alloys such as Bi_2Te_3, PbTe, and SiGe, with ZT up to around 1. Figure 1-3(b) shows that the efficiency of such materials for energy conversion with $T_h / T_c=3$ is about 16%. This situation might apply to waste heat scavenging from automobile exhaust ($T_h \approx 630$ C, $T_c \approx 30$ C) [38]. However, the last decade has seen tremendous progress in pushing ZT beyond 2, thanks to novel nanostructured materials [40-42]. If nanostructured materials can be pushed further to $ZT=3$, the efficiency of the same waste heat scavenging application almost doubles to 29% [Fig. 1-3(b)]. This vastly improved efficiency could open up many more potential applications for thermoelectric energy conversion by lowering the operating cost, although the important issue of the capital cost of the materials still needs to be addressed.

Table 1-1 shows that the increased ZT reported in the literature for two representative nanostructured materials is largely due to reduced thermal conductivity, with some additional help from the electrical performance. Both the quantum dot superlattice of Harman *et al.* [41] and the superlattice of Venkatasubramanian *et al.* [42] show increases in the power factor by about 15-40%, although even larger increases in the power factor $(S^2\sigma)$ are expected [43, 44]. Table 1-1 shows that the thermal conductivity of the nanostructures is 3 to 4 times smaller than bulk, and thus dominates the overall increase in ZT.

The high-ZT measurements reported to date have all been for superlattices, which are essentially 2-dimensional systems. The mechanisms of increased ZT are expected to be even stronger in 1-dimensional nanowires [Fig. 1-1(e)]: the power factor should increase further due to stronger singularities in the electron density of states, and the thermal conductivity should decrease further due to increased phonon scattering at the nanowire sidewalls [21 - 23]. However, this expected enhancement in nanowire ZT has yet to be confirmed experimentally, and remains an important open challenge in the field.

1.3 Outline of the thesis

This thesis is broadly concerned with the thermal properties of nanowire and nanotubes, from both theoretical and experimental perspectives.

Chapter 2 is the most fundamental of the thesis, focusing on quantum / wave effects on phonons in nanostructures. A low-dimensional Debye-Einstein model is developed and compared with measurements of the specific heat TiO_2 nanotubes down to 1.4 K.

Chapter 3 transitions to classical / particle size effects, using kinetic theory to model the reduced thermal conductivity in nanowires and superlattice nanowires. Careful consideration is given to the frequency-dependence of the phonon properties and to the broad range of mean free paths that are important for heat transport.

Chapter 4 generalizes the existing "3ω" method for thermal measurements, to "2ω" and "1ω." These techniques are used to deduce the thermal properties of a system from the electrical response at the first, second, or third harmonic of a driving current. Several practical improvements over the traditional 3ω methods are also presented, making the experiments easier to implement and the data analysis more rigorous.

Chapter 5 describes the detailed design and preliminary testing of a new probe which can be used to measure the thermoelectric properties of individual nanowires and nanotubes inside a transmission electron microscope (TEM). To overcome problems arising from poor thermal contact, the TEM was modified for local electron-beam induced deposition of metals at either end of the nanowire.

Finally, Chapter 6 summarizes the major contributions of this thesis and identifies some important directions for future work.

1.4 References

1. S. Iijima and T. Ichihashi, *Nature* **363**, 603 (1993).
2. D. S. Bethune, C. H. Klang, M. S. de Vries, G. Gorman, R. Savoy, J. Vazquez, and R. Beyers, *Nature* **363**, 605 (1993).
3. S. Iijima, *Nature* **354**, 56 (1991).
4. M. S. Dresselhaus, G. Dresselhaus, and P. C. Eklund, *Science of Fullerenes and Carbon Nanotubes,* Academic Press (1996).

5. R. Saito, G. Dresselhaus, and M. S. Dresselhaus, *Physical Properties of Carbon Nanotubes*, Imperial College Press (1998).

6. X. F. Duan and C. M. Lieber, *Adv. Mater.* **12**, 298 (2000).

7. N. I. Kovtyukhova, B. R. Martin, J. K. N. Mbindyo, P. A. Smith, B. Razavi, T. S. Mayer, and T. E. J. Mallouk, *J. Phys. Chem. B*, **105**, 8762 (2001).

8. S. Nicewarner-Pena, R. G. Freeman, B. D. Reiss, L. He, D. J. Pena, I. D. Walton, R. Cromer, C. D. Keating, and M. J. Natan, *Science* **294**, 137 (2001).

9. Yiying Wu, Rong Fan, and Peidong Yang, *Nano Lett.* **2**, 83 (2002).

10. M. S. Gudiksen, L. J. Lauhon, J. Wang, D. C. Smith, and C. M. Lieber, *Nature* **415**, 617 (2002).

11. L. J. Lauhon, M. S. Gudiksen, D. Wang, and C. M. Lieber, *Nature* **420,** 57 (2002).

12. M. S. Dresselhaus, Y. M. Lin, O. Rabin, M. R. Black, and G. Dresselhaus, "Nanowires," in *Nanotechnology Handbook*, ed. B. Bhushan (Springer-Verlag, 2004).

13. M. S. Dresselhaus, Y. M. Lin, O. Rabin, A. Jorio, A. G. Souza Filho, M. A. Pimenta, R. Saito, Ge. G. Samsonidze, and G. Dresselhaus, *Mater. Sci. Engin. C* **23**, 129 (2003).

14. T. Rueckes, K. Kim, E. Joselevich, G. Y. Tseng, C.-L. Cheung, and C. M. Lieber, *Science* **289**, 94 (2000).

15. Nantero Inc., 25-D Olympia Avenue, Woburn, MA 01801. http://www.nantero.com/

16. Y. Cui, Q. Wei, H. Park, and C. M. Lieber, *Science* **293**, 1289 (2001).

17. M. H. Huang, S. Mao, H. Feick, H. Yan, Y. Wu,, H. Kind, E. Weber, R. Russo, and P. Yang, *Science* **292**, 1897 (2001).

18. X. Duan, Y. Huang, R. Agarwal, and C. M. Lieber, *Nature* **421**, 241 (2003).

19. G. K. Mor, K. Shankar, M. Paulose, O. K. Varghese, and C. A. Grimes, *Nano Lett.* **6**, 215 (2006).

20. M. Grätzel, *Nature* **414**, 338 (2001).

21. L. D Hicks and M. S. Dresselhaus, *Phys. Rev. B* **47**, 16631 (1993).

22. X. Sun, Z. Zhang, and M. S. Dresselhaus, *Appl. Phys. Lett.* **74**, 4005 (1999).

23. Y. M. Lin, X. Sun, and M. S. Dresselhaus, *Phys. Rev. B* **62**, 4610 (2000).

24. H. B. G. Casimir, *Physica* **5**, 495 (1938).

25. N. Mingo and D. A. Broido, *Nano Lett.* **5**, 1221 (2005).

26. R. Berman, F. E. Simon, and J. M. Ziman, *Proc. R. Soc. Lond. A, Math. Phys. Sci.* **220**, 171 (1953).

27. J. M. Ziman, *Electrons and Phonons* (Oxford University Press, 1960).

28. N. W. Ashcroft & N. D. Mermin, *Solid State Physics* (Harcourt, 1976).

29. D. W. Keith, M. L. Schattenburg, Henry I. Smith, and D. E. Pritchard, *Phys. Rev. Lett.* **61**, 1580 (1988).

30. M. S. Gudiksen, J. Wang, and C. M. Lieber, *J. Phys. Chem. B* **106**, 4036 (2002).

31 E. W. Montroll, *J. Chem. Phys.* **18**, 183 (1950)

32. H. P. Baltes and E. R. Hilf, *Solid State Commun.* **12**, 369 (1973).

33. R. Lautenschlager, *Solid State Commun.* **16**, 1331 (1975).

34. H. J. Goldsmid, *Electronic refrigeration* (Pion Press, 1986).
35. D. M. Rowe, ed., *CRC Handbook of Thermoelectrics* (CRC Press, 1995).
36. D. M. Rowe, ed., *Thermoelectrics Handbook: Macro to Nano* (CRC Press, 2005).
37. However, it is still important to consider the entire product life cycle, including manufacturing and disposal, before reaching any firm conclusions about the net contribution to global warming.
38. J. Yang and T. Caillat, *MRS Bull.* **31**, 224 (2006).
39. G. Chen and R. Yang, panel on "Challenges in Chip/Processor Level Thermal Engineering" 9th IEEE/ASME Intersociety Conference on Thermal and Thermomechanical Phenomena in Electronic Systems (ITHERM2004), Las Vegas, NV, June 1-4, 2004.
40. R. Venkatasubramanian, E. Siivola, T. Colpitts, and B. O'Quinn, *Nature* **413**, 597 (2001).
41. T. C. Harman, P. J. Taylor, M. P. Walsh, and B. E. LaForge, *Science* **297**, 2229 (2002).
42. K. F. Hsu, S. Loo, F. Guo, W. Chen, J. S. Dyck, C. Uher, T. Hogan, E. K. Polychroniadis, and M. G. Kanatzidis, *Science* **303**, 818 (2004).
43. L. D. Hicks and M. S. Dresselhaus, *Phys. Rev. B* **47**, 12727 (1993).
44. L. D. Hicks, T. C. Harman, X. Sun, and M. S. Dresselhaus, *Phys. Rev. B* **53**, 10493 (1996).

Chapter 2: Quantum size effects on the specific heat

2.1 Introduction

This portion of the thesis is concerned with phonons in nanostructures. The first half of the chapter develops a model for the phonon dispersion, density of states, and specific heat in low dimensional systems, including thin-walled nanotubes. This model begins from continuum elasticity and includes the effects of phonon confinement, the discreteness of the lattice, and optical modes. The second half of the chapter describes an experimental test of the model against measurements of the specific heat of TiO_2 nanotubes (anatase phase, wall thickness 2.6 nm) from 1.5 to 95 K. The most important conclusion from both modeling and experiments is that low dimensional behavior is only important when the thermally averaged wavelength is comparable to, or longer than, the nanostructure size. The model successfully explains a shift from T^3 to T^2 behavior in the nanotube specific heat for temperatures T below about 10 K, with the nanotube specific heat becoming more than double the bulk value. At higher temperatures the nanotube specific heat is the same as bulk. However, below about 2 K the measured nanotube specific heat is enhanced even more than expected. This may be due in part to low energy vibrations amongst adjacent nanotubes, which can be captured phenomenologically by adding an additional term to the model.

The experimental portion of this chapter has been presented in a previous publication, along with a very brief description of the model [1]. More details about the modeling will appear in a subsequent publication.

2.2 Model

2.2.1 Phonons and specific heat

The specific heat C is defined as

$$C = \frac{\partial E}{\partial T} \tag{2-1}$$

where E is the internal energy and T the absolute temperature. For materials such as insulators and most semiconductors, the internal energy is dominated by phonons rather than electrons, and can be expressed as

$$E(T) = \int \hbar\omega \; f(\omega,T)\, DOS(\omega)\, d\omega \tag{2-2}$$

where $\hbar$ is Planck's constant divided by 2π, ω is the phonon frequency, *DOS* the phonon density of states, and f is the Bose-Einstein factor:

$$f = \frac{1}{\exp(\hbar\omega/k_B T) - 1}, \tag{2-3}$$

where k_B is Boltzmann's constant. Thus,

$$C(T) = \int \hbar\omega \frac{\partial f(\omega,T)}{\partial T} DOS(\omega) d\omega \tag{2-4}$$

The density of states is the only term of Eq. (2-4) that varies from material to material, and is also the only term that changes in a low-dimensional system.

Although $C(T)$ is easily measured, the full phonon dispersion relation is of greater fundamental interest. The dispersion relations are commonly studied with inelastic neutron scattering, as well as scattering of x-ray and visible photons (e.g. Brillouin and Raman scattering) [2, 3]. Equation (2-4) shows that the specific heat also contains useful information about the phonon dispersion relation, through the density of states. It is tempting to consider the possibility of inverting $C(T)$ to yield $DOS(\omega)$. However, for any reasonable level of experimental uncertainty in $C(T)$, such an inversion is known to be impractical [4]. Nonetheless, $C(T)$ is still useful for characterizing model dispersion relations with only a few parameters, such as the Debye and Einstein temperatures. In the following section we derive a similar simple model for low-dimensional systems.

2.2.2 Elastic continuum model of an elastic box: A low-dimensional Debye model

As a first step, consider the well-established Debye model for the density of states and specific heat [2, 3]. The Debye model can be derived beginning from the wave equation for an elastic continuum with isotropic properties,

$$\rho \frac{\partial^2 \mathbf{u}}{\partial t^2} = (\mu + \lambda)\nabla(\nabla \cdot \mathbf{u}) + \mu\nabla^2 \mathbf{u} \tag{2-5}$$

where ρ is the mass density, **u** the local displacement vector, and μ and λ the Lame constants. To simplify further, we approximate the material as incompressible so that $\nabla \cdot \mathbf{u} = 0$. Then

$$\frac{\partial^2 \mathbf{u}}{\partial t^2} = v^2 \nabla^2 \mathbf{u} \tag{2-6}$$

where v is the sound velocity. This simplification neglects the distinction between longitudinal and transverse polarizations. The displacement field **u** can be expressed as a Fourier transform,

$$\mathbf{u}(\mathbf{x},t)=\int\frac{d\omega}{2\pi}\int\frac{d^3\mathbf{q}}{(2\pi)^3}\mathbf{U}(\mathbf{q},\omega)\exp[i(\mathbf{q}\cdot\mathbf{x}-\omega t)] \tag{2-7}$$

where **x** is the position, **q** is the wavevector, and **U** is the polarization vector. Thus, for each eigenmode indexed by a particular value of **q**,

$$\mathbf{u}(\mathbf{x},t)=\mathbf{U}(\mathbf{q},\omega(\mathbf{q}))\exp[i(\mathbf{q}\cdot\mathbf{x}-\omega t)] \tag{2-8}$$

Substituting Eq. (2-8) into Eq. (2-6) yields

$$\omega^2\mathbf{U}=v^2q^2\mathbf{U} \tag{2-9}$$

where $q=|\mathbf{q}|$. This shows that the dispersion relation is

$$\omega(\mathbf{q})=v|\mathbf{q}|\,. \tag{2-10}$$

That is, the frequency is linearly proportional to the wavevector. Thus, these are acoustic modes.

The Debye model is usually presented using periodic boundary conditions because those are the simplest to analyze for bulk materials. For low dimensional structures we need to revisit the boundary conditions. For an isolated sample, the boundaries are free and experience no force. This implies that there are no gradients in the displacement field (i.e. no strain) at the boundaries. For further simplification we restrict the analysis to a rectangular box of size (L_X, L_Y, L_Z), and place the origin at one corner of the box. Then the governing equation and boundary conditions are satisfied by the standing-wave product solution

$$\mathbf{u}=\mathbf{U}(\cos q_x x)(\cos q_y y)(\cos q_z z)(\cos\omega t) \tag{2-11}$$

where each component of the wavevector must satisfy

$$q_i=\frac{\pi\gamma_i}{L_i},\qquad i=x,y,z,\qquad \gamma_i=0,1,2,\ldots \tag{2-12}$$

Note that the traditional Debye analysis using periodic boundary conditions results in wavevectors spaced by $2\pi/L$ rather than π/L.

If the sample is assumed to have fixed rather than free boundaries, then the displacement itself must go to zero at the boundaries. In this case the solutions are of the form

$$\mathbf{u}=\mathbf{U}(\sin q_x x)(\sin q_y y)(\sin q_z z)(\cos\omega t) \tag{2-13}$$

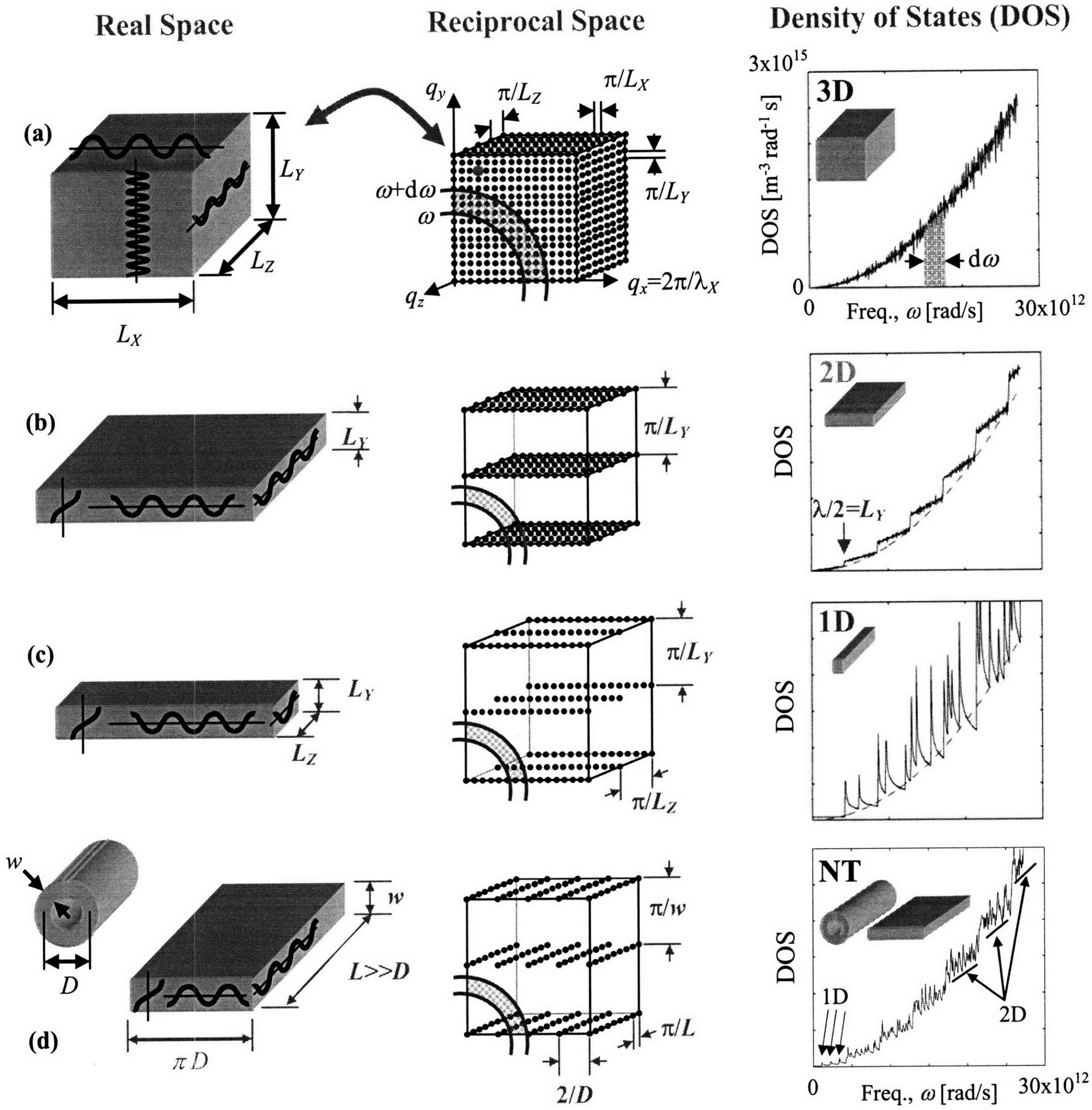

Figure 2-1. Modeling the phonon density of states in low dimensional structures. Columns: (Left) real space, (Center) reciprocal space, (Right) density of states. Rows: (a) bulk / 3D. (b) thin film / 2D, (c) nanowire / 1D, (d) nanotube (NT) unrolled into a sheet. The characteristic lengths of the thin film and nanowire are 2.6 nm. The nanotube has 2.6 nm wall thickness and 6.5 nm average diameter. In all cases the sound velocity is 3560 m/s and the Debye temperature is 260 K. In 3D, 2D, and 1D the low-frequency power-law exponent of the density of states is one less than the dimensionality. The nanotube density of states shows behavior reminiscent of 3D, 2D, and 1D over various different energy ranges.

with each component of the wavevector satisfying

$$q_i = \frac{\pi \gamma_i}{L_i}, \quad i = x, y, z, \quad \gamma_i = 1, 2, \ldots \tag{2-14}$$

Note that $\gamma_i=0$ is allowed for free boundaries but forbidden for fixed boundaries. This is because substituting $\gamma_i=0$ into Eq. (2-13) would force the entire displacement field to be zero. This seemingly minor distinction turns out to be the difference between enhanced specific heat (free boundaries) and reduced specific heat (fixed boundaries).

Focusing on free boundaries, Eq. (2-12) shows that the vibrations are discrete eigenmodes, each of which is conveniently represented by a (q_x, q_y, q_z) point in reciprocal space. The allowed energy of each eigenmode is quantized into discrete levels, each of which corresponds to a phonon. While the traditional Debye analysis passes into the limit $L_i \rightarrow \infty$, to model nanostructures we focus here on the case when one or more of the length scales L_i is small. The resulting calculations are depicted in Fig. 2-1(a-c) for bulk, 2D, and 1D systems. The left-hand column shows a typical eigenmode for each system. The center column shows many such eigenmodes as represented in reciprocal space (notice that wavevectors with $q_i=0$ are permitted). The right-hand column shows the resulting density of states, discussed next.

Density of states for 3D, 2D, and 1D systems

The right-hand column of Fig. 2-1(a-c) shows the density of states for 3D, 2D, and 1D systems, for a model system with sound velocity 3560 m/s and characteristic length 2.6 nm in the thin direction. These parameters were chosen to be a good approximation to TiO_2 (anatase phase), as discussed below. Although the calculations shown in Fig. 2-1 were performed numerically by directly summing all of the allowed eigenmodes according to Eqs. (2-10) and (2-12), these density of states are also readily obtained analytically, as discussed later in this section.

For the simplest interpretation, consider the limiting behavior of the DOS at low energies. From the fundamental definition of DOS:

$$DOS(\omega)d\omega \equiv (\text{\# of phonon modes between } \omega \text{ and } \omega + d\omega) \,/\, (\text{generalized volume}) \qquad (2\text{-}15)$$

where "generalized volume" refers to volume, area, or length, for 3D, 2D, and 1D systems, respectively. By considering the density of dots in reciprocal space near the origin in the center column of Fig. 2-1(a-c), the appropriate expressions are readily derived:

$$DOS_{3D}(\omega \rightarrow 0)d\omega = \left(\frac{1}{L_x L_y L_z}\right)\frac{\pi q^2 dq}{2\left(\pi^3 / L_x L_y L_z\right)}$$

$$DOS_{2D}(\omega \rightarrow 0)d\omega = \left(\frac{1}{L_x L_z}\right)\frac{\pi q dq}{2\left(\pi^2 / L_x L_z\right)} \qquad (2\text{-}16a\text{-}c)$$

$$DOS_{1D}(\omega \rightarrow 0)d\omega = \left(\frac{1}{L_x}\right)\frac{dq}{\left(\pi / L_x\right)}$$

where in each equation the first term in parentheses is the inverse of the generalized volume, and the second term in parentheses is the volume of a single phonon mode in reciprocal space according to Eq. (2-12). These simple expressions are only valid for the lowest acoustic subband, that is, the limit $\omega \rightarrow 0$. Expressions for the higher subbands are given later in this section. For the lowest subband, substituting the linear dispersion of Eq. (2-10) and simplifying leads to

$$DOS_{3D}(\omega \to 0) = \frac{\omega^2}{2\pi^2 v^3}$$

$$DOS_{2D}(\omega \to 0) = \frac{\omega}{2\pi v^2} \qquad \text{(2-17a-c)}$$

$$DOS_{1D}(\omega \to 0) = \frac{1}{\pi v}$$

The pattern is clear: for dimensionality $n \geq 1$, the density of states has the limiting behavior at low frequency

$$DOS_{nD}(\omega \to 0) \propto \frac{\omega^{n-1}}{v^n} \ , \ n \geq 1 \qquad \text{(2-18)}$$

where the numerical prefactors are different for the different dimensionalities.

The simple result of Eq. (2-18) only holds for phonon systems with linear dispersion, which is a good approximation for the vast majority of materials in the limit of low-frequency. However, parabolic phonon dispersion is also present in some materials such as graphene [6]. In general

$$DOS_{nD}(\omega \to 0) \propto \frac{q^{n-1} dq}{d\omega}, \qquad \text{(2-19)}$$

regardless of the type of dispersion. For a more general analysis consider the power-law dispersion:

$$\omega \propto q^p \qquad \text{(2-20)}$$

This form describes both acoustic phonons (p=1) and electrons in a parabolic band (p=2). For the power-law dispersion,

$$q \propto \omega^{1/p} \qquad \text{(2-21)}$$

and

$$dq \propto (1/p)\omega^{\left(\frac{1}{p}-1\right)} d\omega \qquad \text{(2-22)}$$

Substituting Eqs. (2-21) and (2-22) into Eq. (2-19) yields

$$DOS_{nD,power\ law}(\omega \to 0) \propto \omega^{\left(\frac{n}{p}-1\right)} \tag{2-23}$$

which is a generalization of Eq. (2-18).

The pattern of Eq. (2-18) for the power-law exponents of $DOS(\omega)$ is apparent from the small-ω portion of the DOS plots of Fig. 2-1(a-c). In 3D systems, $DOS_{3D} \propto \omega^2$. For the 2D system, each acoustic subband has $DOS_{2D} \propto \omega^1$. And for the 1D system, the lowest subband has a constant DOS ($DOS_{1D} \propto \omega^0$).

Analysis of Fig. 2-1(c, center) shows that the DOS for higher acoustic subbands in the 1D system are given by

$$DOS_{1D}(\omega > vq_0) = \frac{1}{\pi v}\sqrt{\frac{\omega^2}{\omega^2 - v^2 q_0^2}} \tag{2-24}$$

where q_0 is the offset in reciprocal space between the origin and the subband of interest. For example, for the nanowire of Fig. 2-1(c), the offsets are given by

$$q_{0,1D}(\gamma_y, \gamma_z) = \sqrt{\left(\frac{\pi \gamma_y}{L_y}\right)^2 + \left(\frac{\pi \gamma_z}{L_z}\right)^2}, \qquad \gamma_y = 0,1,2,..., \quad \gamma_z = 0,1,2,... \tag{2-25}$$

Eq. (2-24) shows that the singularities apparent in Fig. 2-1(c) are integrable, and each approaches the constant value $1/\pi v$ as $\omega >> vq_0$, regardless of the subband offset q_0.

Interestingly, analysis of Fig. 2-1(b, center) shows that the DOS for higher acoustic subbands in 2D do not have any singularities, but rather are given by

$$DOS_{2D}(\omega > vq_0) = \frac{\omega}{2\pi v^2} \tag{2-26}$$

where the offset wavevectors are given simply by

$$q_{0,2D}(\gamma_y) = \frac{\pi \gamma_y}{L_y}, \qquad \gamma_y = 0,1,2,... \tag{2-27}$$

Equations (24-27) form the basis of a fully analytic solution for the phonon density of states in a thin film or nanowire of square cross-section, by simply summing over all the subbands indexed by γ_y and γ_z. Although the plots of Fig. 2-1(right) were obtained by direct numerical summation over all allowed points in reciprocal space (q_x was discretized by assuming some large but finite value of L_x), the analytic expressions were used to check the numerical results for several cases.

A very important feature of the DOS plots in the right-hand column of Fig. 2-1 is that the averaged trend over a broad range of energies is still quadratic in ω. This is because high energies correspond to short wavelengths. At sufficiently high energies the wavelengths become far smaller than the nanostructure size, for example $\lambda \ll L_Y$ in Fig 2-1(b), and so the confinement effects become unimportant. This transition occurs when $\lambda \approx 2L$, which is expected when

$$\omega_{trans} \approx \frac{\pi v}{L} \tag{2-28}$$

Minimum length scale: Debye cutoff

Because the model described so far assumes a continuum, there is no minimum length scale, and thus the wavelengths can become arbitrarily small. Equivalently, there is no upper limit on the energy or wavevector. In reality, the wavelength cannot be smaller than two unit cells of the underlying crystal lattice. Thus, following the traditional Debye model [2, 3], we define a cutoff wavevector as

$$q_{\max} = \left(6\pi^2 \eta\right)^{1/3} \tag{2-29}$$

where η is the number density of primitive unit cells. This corresponds to a maximum frequency of

$$\omega_{\max} = v q_{\max} = \left(6\pi^2 v^3 \eta\right)^{1/3} \tag{2-30}$$

which is the cutoff used in the *DOS* plots of Fig. 2-1. The corresponding Debye temperature is given by

$$\theta_D \equiv \frac{\hbar \omega_{\max}}{k_B} = \frac{\hbar v}{k_B} \left(6\pi^2 \eta\right)^{1/3} \tag{2-31}$$

Specific heat for 3D, 2D, and 1D systems

Having modeled the density of states, it is straightforward to compute the specific heat numerically from Eq. (2-4). Figure 2-2(a) shows the results for 3D, 2D, and 1D systems. It is clear that the limiting behavior in $C(T)$ at low temperature is a power law whose exponent is the same as the dimensionality of the system, n:

$$C_{nD}(T \to 0) \propto T^n \quad , \quad n \geq 1 . \tag{2-32}$$

We now demonstrate that this simple pattern is a direct consequence of the limiting density of states given by Eq. (2-18). Ignoring numerical constants, according to Eqs. (2-3), (2-4), and (2-18) the specific heat can be expressed as

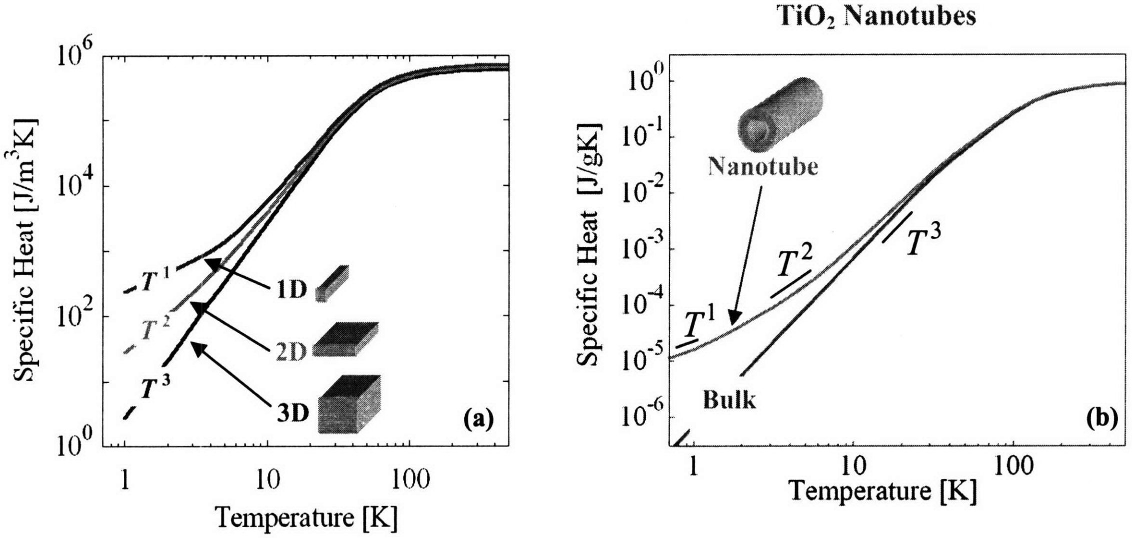

Figure 2-2. Calculated specific heat of the low-dimensional structures shown in Fig. 2-1. (a) Bulk (3D), thin film (2D), and nanowire (1D), showing that the power law exponent of the low-temperature specific heat is equal to the dimensionality. (b) Nanotube compared to bulk. The nanotube specific heat transitions from 3D ($C \propto T^3$) to 2D ($C \propto T^2$) to 1D ($C \propto T^1$) behavior with decreasing temperature. In all cases the high-temperature specific heat approaches a constant value, in accordance with the law of DuLong and Petit.

$$C_{nD}(T) \propto \frac{\hbar^2}{k_B T^2} \int_0^{\omega_{max}} \frac{\omega^2 \exp(\hbar\omega / k_B T)}{[\exp(\hbar\omega / k_B T) - 1]^2} \left(\frac{\omega^{n-1}}{v^n} \right) d\omega \tag{2-33}$$

where the last term in parentheses reflects the dependence of the density of states on dimensionality. Making the usual substitution $r = \hbar\omega / k_B T$ [2, 3], the integral simplifies to

$$C_{nD}(T) \propto k_B \left(\frac{k_B T}{\hbar v} \right)^n \int_0^{r_{max}} \frac{r^{n+1} \exp(r)}{[\exp(r) - 1]^2} dr \tag{2-34}$$

For any dimensionality n, the integrand decays exponentially for $r >> 1$, and so the integration is dominated by relatively small values of r (of order unity). Thus, there always exists a low enough temperature such that $r_{max} = \hbar\omega_{max} / k_B T$ can be approximated as infinity, in which case the integral loses all temperature dependence and becomes simply a numerical constant depending only on n. For example, in 3D the integral approaches $4\pi^4/15$ as $r_{max} \rightarrow \infty$ [2]. Thus, the low temperature limit becomes

$$C_{nD}(T \rightarrow 0) \propto k_B \left(\frac{k_B T}{\hbar v} \right)^n \propto T^n \tag{2-35}$$

justifying the observation of Eq. (2-32).

The transition from bulk to low-dimensional specific heat is expected at temperatures so low that the average wavevector is too small to populate anything beyond the first acoustic subband, for example, $\lambda \approx 2L_Y$ in the thin film of Fig. 2-1(b). The average wavelength can be estimated roughly from the energy criterion of Eq. (2-28) and $\hbar\omega_{trans} \approx k_B T_{trans}$,

$$\lambda_{avg} \approx \frac{2\pi\hbar v}{k_B T} \tag{2-36}$$

Thus we would expect

$$\lambda_{avg} T \sim 240\,\mathrm{nm\,K}(v/5000\,\mathrm{m/s}), \tag{2-37}$$

where the fundamental constants k_B and $\hbar$ have been re-expressed in more convenient units using nm, K, and m/s. However, a better estimate for the numerical prefactor in Eq. (2-37) is found by analogy to Wien's displacement law for thermal radiation, $\lambda T \approx 2898$ μm K (here v=speed of light) [5].

$$\lambda_{avg} T \approx 50\,\mathrm{nm\,K}(v/5000\,\mathrm{m/s}). \tag{2-38}$$

This expression assumes linear dispersion and is useful for quick, approximate estimates in 3D, 2D, or 1D (but not necessarily 0D) systems. Careful consideration of the transitions in $C(T)$ show that the full range of the transition spans from approximately 12 nm K to 200 nm K:

$$12\,\mathrm{nm\,K} < \left(\frac{T_{trans}L}{(v/5000\,\mathrm{m/s})}\right) < 200\,\mathrm{nm\,K} \tag{2-39}$$

For example, we would expect a 5 nm thin film made of material with sound velocity 2500 m/s to be dominated by 2D phonon behavior ($C \sim T^2$) at temperatures below 1.2 K ($L_Y T$=6 nm K), and revert to fully 3D behavior ($C \sim T^3$) above 20 K ($L_Y T$=100 nm K).

2.2.3 Elastic continuum model of an unrolled nanotube

The analysis described above in Eqs. (2-11) through (2-28) is limited to rectangular parallelepipeds. However, it can also be used to approximate the phonons in a nanotube as long as the nanotube wall is thin compared to its diameter. This is done by imagining cutting along the length of the nanotube and unrolling it into a flat, narrow sheet [Fig. 2-1(d, left)]. Like some models for the phonon specific heat in carbon nanotubes, this model neglects the effects of curvature in changing the energy of some out-of-plane modes that correspond to radial breathing modes [6, 7]. As shown in Fig. 2-1(d, left), the unrolled sheet is as thick as the nanotube wall, w, and as wide as the nanotube circumference, πD. Now a periodic boundary condition must be applied in the circumferential direction:

$$q_{circumf} = \frac{2\gamma_{circumf}}{D}, \qquad \gamma_{circumf} = 0,1,2,... \tag{2-40}$$

while the thickness and length directions still have free boundaries and are described in Eq. (2-12). This is essentially a zone-folding scheme similar to those that have been applied to carbon nanotubes [6, 7]. Although this model does not explicitly distinguish between longitudinal, transverse, and twist acoustic modes, the method for counting modes should ensure the correct density of states at low energies as long as curvature effects can be neglected. The nanotube phonon modes are depicted in reciprocal space in Fig. 2-1(d, center).

Density of states for a nanotube

The density of states for this model nanotube is shown in Fig. 2-1(d, right). This plot shows three different types of behavior depending on the energy range of interest. As with the 1D and 2D systems, the smoothed nanotube DOS follows a parabolic trend, corresponding to the 3D behavior of Fig. 2-1(a). Again, this is because large energies correspond to short wavelengths, which become smaller than all of the nanotube length scales, causing confinement effects to be negligible.

Looking somewhat more closely at the nanotube DOS, several noisy steps are apparent, each proportional to ω^1 and spanning about 5 x 10^{12} rad/s. These are clearly reminiscent of the steps in the 2D DOS of Fig. 2-1(b), and are caused by phonon confinement in the nanotube wall-thickness direction. The boundary condition of Eq. (2-12) requires that an integer number of half-wavelengths span the nanotube wall. As ω increases, the set of allowed wavevectors in the radial direction progress from $q_{radial}=0$ to include $q_{radial}=\pi/w$, $2\pi/w$, $3\pi/w$, ... Each additional q_{radial} corresponds to accessing another radial acoustic subband, leading to the stepwise increase in the DOS.

At the finest level of detail, the nanotube DOS in Fig 2-1(d) shows many small spikes, for example at $\omega \approx 1$, 2, and 3 x 10^{12} rad/s. These are 1D singularities similar to Fig. 2-1(c) and Eq. (2-24). In this regime the wavelengths are so long as to be comparable to the circumference of the nanotube. These first three singularities correspond to the circumferential acoustic subbands when 1, 2, and 3 wavelengths span the circumference: $q_{circumferential}=2/D$, $4/D$, and $6/D$.

Specific heat for a nanotube

The DOS of Fig. 2-1(d) suggests that the phonon properties of a nanotube may exhibit 3D, 2D, or 1D behavior, depending on the energy range of interest. This pattern is indeed apparent in the calculated specific heat shown in Fig. 2-2(b). As the temperature decreases, the average wavelengths increase, and we see a transition from 3D, to 2D, to 1D behavior. Well above the Debye temperature, the bulk and nanotube specific heats both saturate, in accordance with the law of Dulong & Petit. From ~100 K down to ~30 K, the nanotube specific heat follows a T^3 trend, corresponding to 3D behavior. At around 5 K, the nanotube specific heat transitions to a T^2 trend, corresponding to 2D behavior. This is because the average wavelengths are long enough to feel the constraint in the wall thickness direction. With that dimension "frozen out", there are effectively only two free dimensions remaining. Below ~1 K, the nanotube specific heat follows a T^1 trend, corresponding to 1D behavior. Here the average wavelengths are long compared to both the wall thickness and the circumference. With two dimensions frozen out, only one free dimension remains.

2.2.4 Accounting for optical modes: Einstein model

The generalized Debye model described thus far is appropriate for materials with only acoustic phonons, that is, crystal structures with only one atom per primitive unit cell (i.e., a monatomic basis). However, most materials of technological interest have polyatomic bases, which introduces optical phonon modes as well. For example, a material with η primitive unit cells per unit volume, and a basis of b atoms, has 3η acoustic modes, leaving

$$\eta_{optical} = 3\eta(b-1) \tag{2-41}$$

optical modes per unit volume. In the Einstein model [2, 3] these optical modes are assumed to all have the same frequency ω_E, corresponding to an Einstein temperature of

$$\theta_E \equiv \hbar\omega_E / k_B . \tag{2-42}$$

That is, the dispersion relation for Einstein modes is

$$\omega(q) = \omega_E . \tag{2-43}$$

Thus, the DOS for an Einstein model is simply a delta function:

$$DOS_E(\omega) = \eta_{optical}\delta(\omega - \omega_E) \tag{2-44}$$

Applying this DOS to the specific heat integral Eq. (2-4) gives the optical contribution to the specific heat:

$$C_{optical}(T) = \eta_{optical} k_B \left(\frac{\theta_E}{T}\right)^2 \frac{\exp(\theta_E/T)}{[\exp(\theta_E/T)-1]^2} \tag{2-45}$$

Like the Debye model outlined above, this Einstein specific heat saturates to the Dulong and Petit value well above its characteristic temperature (θ_D and θ_E, respectively), but at low temperatures $C_{optical}(T)$ falls off much more sharply than the Debye specific heat.

Like acoustic phonons, optical phonons in nanostructures will also have their wavevectors quantized due to subband folding effects. However, because of the assumed Einstein dispersion relation, this does not have any effect on the resulting specific heat calculation. The key difference is that the density of states for acoustic phonons is sensitive to confinement effects, because the frequency depends on the wavevector [Eq. (2-10)]. Thus, altering the allowed wavevectors alters the density of states (Fig. 2-1, right). However, for the Einstein dispersion relation [Eq. (2-43)] the density of states is always a delta function at $\omega=\omega_E$, regardless of the altered wavevectors.

2.2.5 Accounting for intertube modes

The low-dimensional Debye-Einstein model described above is appropriate for an isolated nanotube, but experimentally it is far easier to measure the specific heat of a collection of many nanotubes, which may be pressed together as a loose pellet. In this case we would expect some amount of coupling between adjacent nanotubes. It is difficult to calculate the precise coupling strength, but we can estimate the influence of the coupling on the specific heat by considering the following limiting case. Each nanotube can be thought of as a new super-unit cell, with many hundreds or thousands of atoms in the basis. The analysis above deals with the phonon modes internal to each nanotube, while the modes among nanotubes would be a new set of acoustic phonons. These supercell acoustic phonons would be expected to have very low energies, because the coupling is only through the few atomic sites between the adjacent nanotubes, while the mass is due to many thousands of atoms within each nanotube. Stated another way, the characteristic frequency can be estimated as $\omega \sim \sqrt{g/m}$, where g is the stiffness and m is the mass. For the supercell acoustic phonon, g is expected to be comparable to or somewhat larger than the covalent bonding stiffness between adjacent atoms, while m should be many thousands of times larger than the mass of a single atom. Thus, the characteristic frequency for intertube modes is expected to be much lower than the characteristic phonon frequencies of the bulk. Thus, for sufficiently weak intertube coupling, the intertube modes will already be saturated in the Dulong and Petit regime for all temperatures of interest. Therefore the contribution from intertube modes is expected to be a small constant, independent of temperature:

$$C_{\text{intertube}}(T) = \eta_{\text{intertube}} k_B \tag{2-46}$$

Here $\eta_{intertube}$ is the number of intertube phonon modes per unit volume, expected to be much smaller than the number density of primitive unit cells, η. Equation (2-46) applies for temperatures well above the characteristic intertube temperature given by

$$\theta_{\text{intertube}} \equiv \hbar\omega_{\text{intertube}} / k_B \tag{2-47}$$

Submodel	Low-Dimensional Elastic Box	Debye Cutoff	Optical Modes (Einstein)	Intertube Modes
Temperature range of importance	$T < \sim\theta_D$	$T \geq\sim\theta_D$	$T \geq\sim\theta_E$	Very low
Sound velocity, v	√	√		
Geometry: L_x, L_y, L_z	√			
Boundary conditions (fixed, free, or periodic)	√			
Number density of primitive unit cells, η		√	√	
Number of atoms in the basis, b			√	
Number density of intertube phonon modes, $\eta_{intertube}$				√
Einstein energy, ω_E, or temperature, θ_E			√	
Upper limit on intertube phonon energy, $\omega_{intertube,max}$, or temperature, $\theta_{intertube,max}$				√

Table 2-1. Required input parameters for the 4 sub-models for the specific heat of nanostructures (The Debye temperature, θ_D, is not an independent parameter because it is determined by v and η.) For example, the number density of primitive unit cells is required for both the Debye cutoff sub-model and the optical modes sub-model. Values of these parameters are given in Tables 3 and 4.

It is difficult to estimate this temperature but it is expected to be well below 1 K. To model the intertube contribution to the specific heat below $\theta_{intertube}$, either a Debye or Einstein model may be appropriate.

2.2.6 Summary of model

As summarized in Table 2-1, the model described above has 3 key elements, as well as a 4th phenomenological element which may be relevant at very low temperatures:

(1) The heart of the model is the low-dimensional Debye sub-model for an elastic continuum box or nanotube. For this sub-model, a material is fully specified by its sound velocity, geometry, and boundary conditions (fixed, free, or periodic). The resulting temperature-dependent specific heat shows a power law exponent equal to the dimensionality.

(2) At high temperatures a Debye cutoff wavevector is introduced. This takes into account the granularity of the atomic lattice, which imposes a minimum wavelength and ensures that the specific heat saturates to a constant value at high temperature. The sound velocity and number density of primitive unit cells are required to specify the specific heat of a material for this sub-model.

(3) At high temperatures the sub-model for optical modes is also important. To specify the appropriate Einstein contribution, the number density of primitive unit cells, number of atoms in the basis, and Einstein energy or temperature are necessary.

(4) At very low temperatures the model can be speculatively extended to account for intertube vibrational modes, by specifying a number density of intertube phonons and an upper limit on the characteristic intertube frequency or temperature.

2.3 Experiment

2.3.1 Previous work

Limited experimental data are available to test models for the specific heat of nanostructures. The first experiments were on zero-dimensional (0D) metallic nanoparticles of ~2-10 nm diameter, where experiments [8, 9] show a specific heat enhanced by 50%-100% at temperatures where the average wavelength is comparable to the diameter, an exponential decay at lower temperatures, and an asymptotic return to bulk values at higher temperatures. These results have been successfully explained by theories which sum over all of the normal modes of an elastic sphere with free boundaries [10, 11], similar to the principle of the low-dimensional Debye sub-model described above.

More recently, there has been considerable effort to study the specific heat of carbon nanotubes (CNT). Yi et al. [12] observed a linear temperature dependence from 300 K down to 10 K in multi-walled (MW) CNT, in close agreement with isolated sheets of graphene. In contrast, another MWCNT experiment by Mizel et al. [13] showed a much steeper decay with temperature of about $T^{2.5}$ down to ~1 K, a better match to graphite. Bundles of single-walled (SW) CNT were studied by both Hone et al. [14] and Mizel et al. [13], and the specific heat exhibited a linear or slightly superlinear temperature dependence from ~100 K down to ~2-4 K, consistent with multiple 1D acoustic subbands. At lower temperatures Lasjaunias et al. [15, 16] reported a transition to a T^3 dependence, attributed to the filling up of inter-tube modes, plus a surprising additional term proportional to $T^{0.34}$ or $T^{0.62}$ below ~1 K. The additional contribution below 1 K was qualitatively attributed to localized excitations of atomic

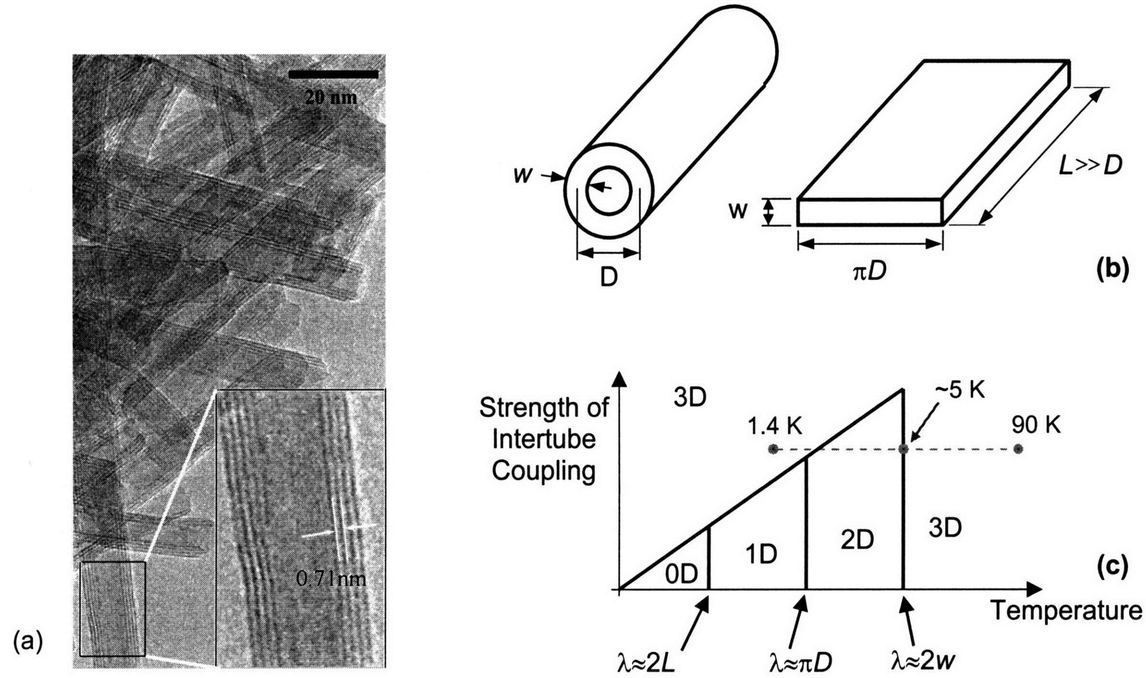

Figure 2-3. Modeling the specific heat of TiO_2 nanotubes. (a) Transmission electron micrograph of typical anatase nanotubes used in this experiment. (b) Unrolling a nanotube into a sheet. (c) Phonon phase diagram indicating the dimensionality for various temperatures and intertube coupling strengths, after Hone *et al.* [14]. The dashed line indicates approximately the regime explored in these experiments. Intertube coupling may have prevented 1D behavior from being observed.

rearrangements, as in glasses and amorphous materials. In all of these studies, the temperature dependence of the specific heat is bounded between that of graphite and graphene. Various theoretical efforts have had mixed success at explaining these MWCNT and SWCNT measurements by extending isolated tube models [7] to include the effects of interlayer coupling (in MWCNT) and intertube coupling [13, 14, 17, 18]. Overall, more work is still needed to reconcile the diverse experimental results with theory [6].

2.3.2 TiO_2 nanotubes (anatase phase)

As a test of the model for low-dimensional specific heat described above, we have measured the specific heat of multi-walled TiO_2 nanotubes (anatase phase) from 1.4 to 90 K, and we have compared these results with measurements of anatase powder. Because the powder size is several microns, it represents the intrinsic specific heat of bulk anatase. Powders of the rutile phase of TiO_2 were also measured for comparison. These are the first measurements of the specific heat of any non-carbon nanotubes, and the results show that the nanotube specific heat is enhanced by up to an order of magnitude or more compared to bulk.

Sample	Purity	Crystallinity (qualitative)	Cold Press Pressure [MPa]	Comment
NT1	<0.5 at% Na	Excellent	160	Highest quality sample.
NT2	~10 at% Na	Poor	480	
NT3	~7 at% Na	Excellent	160	
NT4	~10 at% Na	Poor	160	
Anatase Bulk	99.9%	Excellent	800	Particle size <44 μm.
Rutile Bulk	99.5%	Excellent	800	Average particle size 1 - 2 μm.

Table 2-2. Properties of the nanotube and bulk samples used in the specific heat experiments.

Although these anatase nanotubes were chosen primarily for their small size and availability in large quantities, they have potential applications for solar cells, electrolysis, and photocatalysis [19]. Compared to the strongly anisotropic layering of graphite, anatase is more nearly isotropic, making this material system distinct from CNT. Our nanotubes were synthesized by a hydrothermal method, described in more detail elsewhere [20]. The optimized synthesis conditions result in very pure, crystalline nanotubes [Fig 2-3(a)]. Typical dimensions are L=500 - 1000 nm in length, w=2.5 nm in wall thickness, and D=6.5 nm average diameter (9 nm outside diameter). The spacing between adjacent wall layers is about 0.70 to 0.75 nm, about double the spacing between [100] anatase planes. In contrast to carbon nanotubes, these anatase nanotubes are believed to form by the rolling up of a flat sheet [21]. We also tested nanotubes with poor crystallinity and various levels of sodium contamination obtained from sub-optimal synthesis conditions [20]. Energy dispersive x-ray analysis (EDX) was used to estimate the level of sodium contamination, ranging from about 10 at% to less than 0.5 at%, the detection limit. Table 2-2 summarizes the properties of the nanotube samples as well as the anatase and rutile powder samples.

2.3.3 Experimental method

For each measurement, the as-prepared nanotubes, or as-received powders, were cold-pressed into a pellet and then cleaved into a mm-scale sample weighing about 5 - 15 mg. In an effort to study the effects of inter-tube coupling, the cold-press pressure was varied from 80 to 800 MPa. Although no systematic relationship between pressure and specific heat was observed, in the samples contaminated

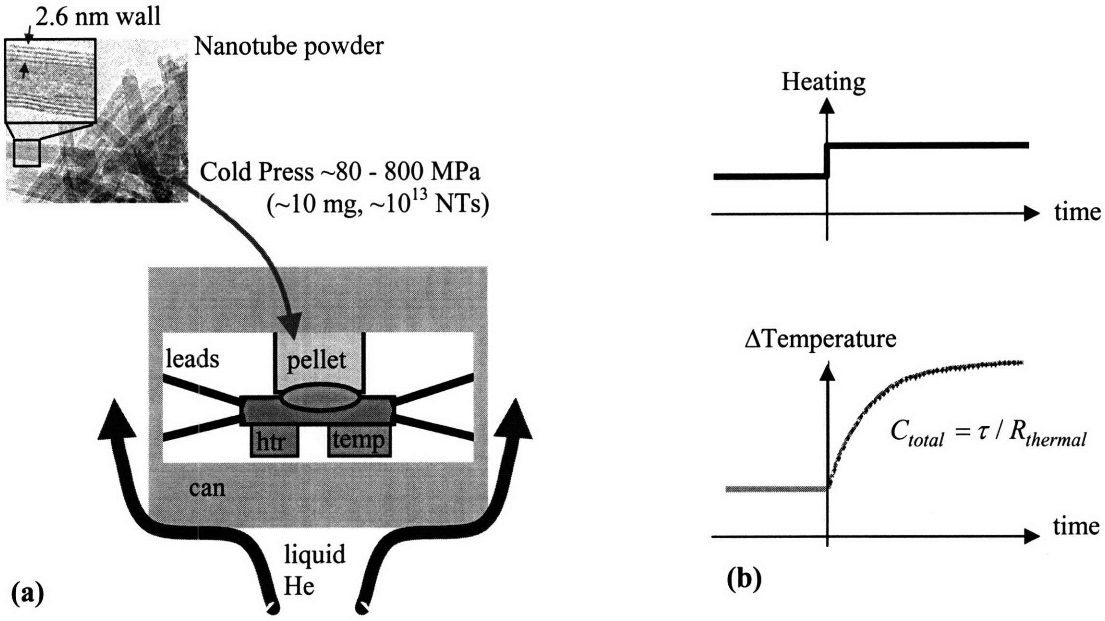

Figure 2-4. Experimental apparatus to measure specific heat. (a) Schematic of the calorimeter The sample comprises a mm-scale pellet of ~10 mg mass, cold-pressed from loose powder. It is mounted on a small sapphire stage using grease. The stage includes a heater (htr) and temperature sensor (temp), and is suspended on fine wires inside a copper can, which itself is placed a continuous-flow liquid helium cryostat. (b) Thermal relaxation method used to determine the total heat capacity from the thermal time constant in response to a step change in heat input. The points are from an actual data trace. The thermal resistance and background heat capacity of the stage were calibrated previously, allowing the change in specific heat due to the sample to be calculated.

with sodium we did notice a surprising green tint that became more prominent with increasing pressure. Seven nanotube samples were measured but for clarity only four are reported here. A small amount of thermal grease (Wakefield 120-2) was used to attach the sample to the sapphire stage of a calorimeter (Oxford Instruments) for measurements by a standard relaxation method in a liquid helium cryostat (Figure 2-4). This relaxation method uses one time constant. For the powder samples below ~10 K there was slight evidence of a secondary time constant due to internal thermalization (a "two-tau" problem), which using the method suggested by Tsujii et al. [22] we estimate to contribute ~5-10% uncertainty in this temperature range.

The contributions of the grease and addenda heat capacities (calibrated separately) were subtracted from the total measured heat capacity before calculating the sample's specific heat. For nanotube samples, this adjustment for grease and addenda represented about 10 -30% of the total heat capacity over this temperature range, although for the anatase and rutile powders the adjustment ranged up to about 70%. The uncertainties are dominated by the scatter in the total heat capacity data, and are estimated as ±4% (±1 standard deviation) for the nanotube specific heat. Because the powder samples require a relatively larger addenda correction, their uncertainty is magnified to about ±10% at low temperatures. The temperature sensor (Cernox) is believed to be accurate to better than ±1%.

The measurements were repeatable without hysterisis, even after He was introduced into the sample space and then pumped off at elevated temperatures (~70 K). Most of the sodium impurities are thought to be distributed and taken up in sodium titanate [20] ($Na_xH_{1-x}Ti_3O_7$, $x \sim 0.75$) with unknown specific heat, but if clusters of metallic Na are assumed, then the contribution to the specific heat would be less than 10% for the most-contaminated samples. However, we cannot rule out the possibility of adsorbed gases influencing the low-temperature NT data because the samples typically were degassed only briefly (~30 minutes) under vacuum at 300 K prior to cooling [14-16]. A later annealing study at 573 K in vacuum for 24 hours suggests that the NT samples may have been contaminated by up to ~7.3% (NT1) or ~11% (NT2) by mass by an unknown adsorbate. EDX analysis leads us to suspect the contaminant was water. The bulk powder samples showed no evidence of similar contamination. Although it is difficult to account for the contribution of monolayers of water, we have used the mass-averaged properties of bulk anatase (our measurements) and bulk ice [23] to estimate the impact of possible ice contamination below.

2.3.4 Results and discussion: bulk

Figure 2-5 shows the measured specific heat for bulk anatase, bulk rutile, and anatase nanotubes.

The bulk rutile data are in good agreement with literature values above 20 K [24-26]. Below 5 K, both the current and literature data follow a T^3 trend down to 2.5 K where they transition to a $T^{2.2}$ trend. However, below 9 K the current values are over twice as large as the only literature source [27], an unexplained discrepancy which far exceeds our experimental uncertainty.

The bulk anatase data are in good agreement with literature values above 50 K [25, 26]. We are unaware of any literature values at lower temperatures. As shown in Fig. 2-6, these data can be described to within 10% by a combined Debye and Einstein model (θ_D= 260 K, θ_E= 475 K, obtained by fitting), implying an average sound velocity of 3560 m/s. This calculation uses the known number density of primitive cells for anatase of $\eta = 1.47 \times 10^{28}$ m^{-3} and the fact that anatase has a 6-atom basis. The properties used in this calculation are summarized in Table 2-3.

Accounting for possible ice contamination

As mentioned previously, we have reason to suspect that the nanotube samples were contaminated by ice (for example, 7.3 mass% for NT1). This means that the bulk counterpart to compare with nanotube calculations is not the pure anatase measured here, but rather a combination of 92.7% anatase and 7.3% ice. A revised bulk curve for $C(T)$ was obtained from a simple weighted average, by

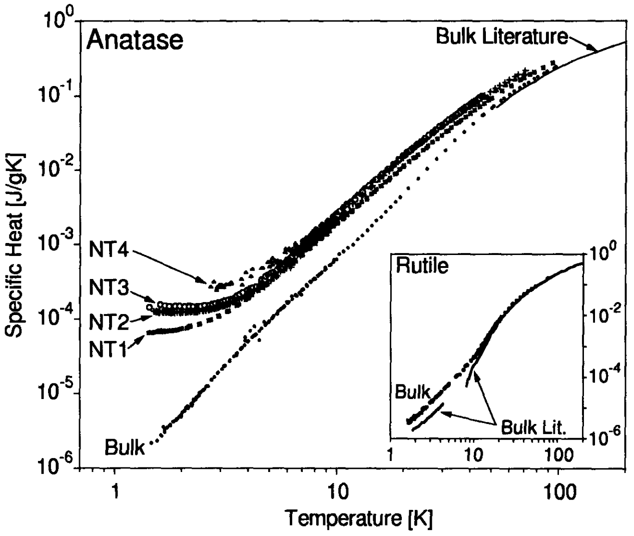

Figure 2-5. Measured specific heat of anatase nanotube samples NT1-NT4 and bulk anatase compared to literature. [25] Inset: measured specific heat of bulk rutile compared to literature [24-27].

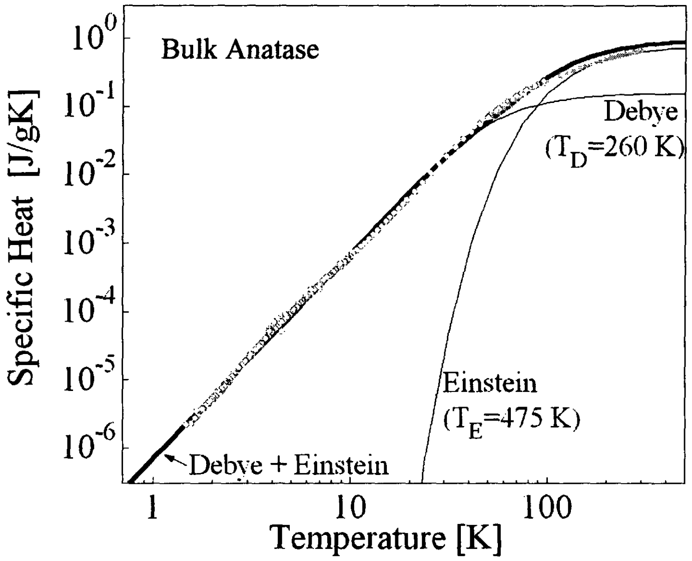

Figure 2-6. Extracting Debye and Einstein temperatures from the measured specific heat of bulk anatase. This calculation also requires the number density of primitive unit cells and the number of atoms in the basis.

assuming that the contributions from ice and anatase added linearly. This new bulk curve was then reanalyzed for revised Debye and Einstein temperatures (θ_D=235 K, θ_E=550 K) to be used in the modeling below designated "adjusted for ice" [Fig. 2-7(b)].

Property	Symbol	Value
Average sound velocity	v	3560 m/s
Number density of primitive unit cells	η	1.47×10^{28}
Debye temperature	θ_D	260 K
Einstein temperature	θ_E	475 K
Number of atoms in the basis	b	6

Table 2-3. Properties used in modeling the specific heat of bulk anatase, without any ice contamination.

2.3.5 Results and discussion: nanotubes

As shown in Fig. 2-5 and Fig. 2-7, the anatase nanotube specific heat data always exceed those of bulk anatase. From 100 K down to about 60 K, the excess is about 20 - 30%, with the highest-quality sample (NT1) showing the least enhancement. From 50 K down to about 5 K, all of the nanotube curves shift to a $T^{2.6}$ dependence, clearly diverging from the bulk anatase. Below about 4 K the available nanotube data shows a second transition to a nearly constant value, exceeding the bulk anatase values by factors of 25 to 50 at 1.5 K. Again, the highest quality nanotube sample shows the least enhancement, about half that of the lower-quality samples (NT2-4). After adjusting the bulk specific heat for possible ice contamination, however, the bulk and NT1 specific heats are very similar above about 10 K [Fig. 2-7(b)].

Phonon phase diagram

The transitions in the specific heat can be interpreted in terms of a conceptual phase diagram [Fig 2-3(c)] which shows the dimensionality of a nanotube as a function of temperature and the strength of intertube coupling. This has been generalized from a similar diagram by Hone et al. [14] for CNT by including 3D behavior in the high temperature limit for anatase nanotubes, in contrast to the limiting 2D graphitic behavior for CNT. The dashed line indicates approximately the regime explored in this experiment.

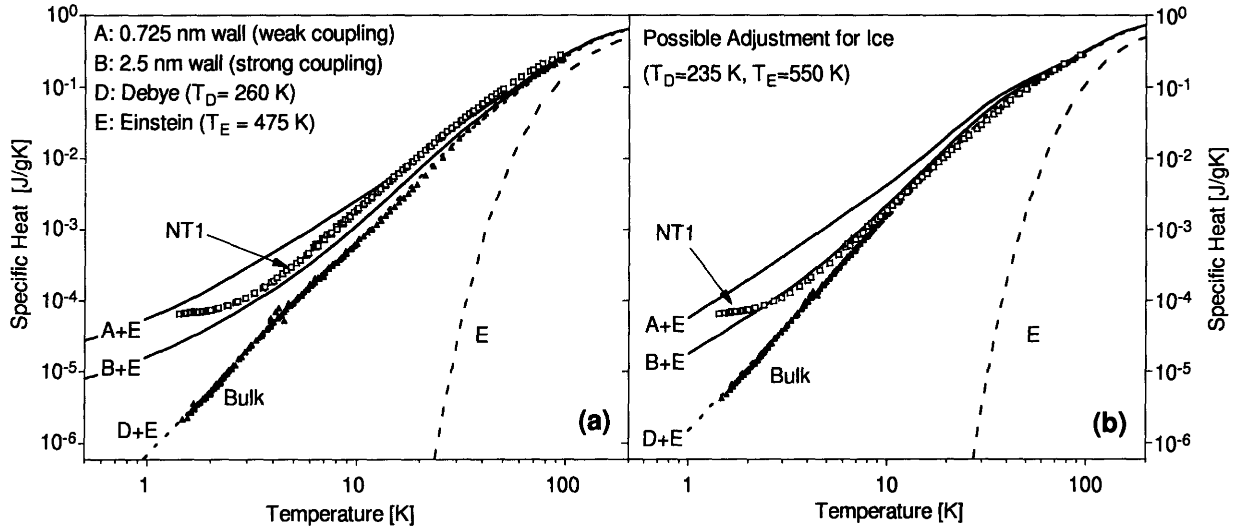

Figure 2-7. (a) Modeled and measured specific heat for anatase nanotube sample NT1 and bulk anatase. (b) Possible adjustment to analysis of NT1 assuming 7.3% contamination by ice. The NT1 data is the same as (a), while the bulk data from (a) has been adjusted to incorporate 7.3% ice.

Transition from 3D to 2D

Using the model described earlier, the upper transition in the nanotube specific heat is interpreted as a shift from 3D to 2D behavior. As shown in Fig. 2-3(c), a transition is expected because the average thermal wavelength λ is comparable to the nanotube wall thickness. Because of the uncertain coupling strength between layers of the wall, we have performed the calculation for assumed wall thickness of both 0.725 nm (model A: weak coupling) and 2.5 nm (model B: strong coupling). These and other parameters are summarized in Table 2-4. The circumferential periodic boundary condition in a rolled-up structure still requires the assumption of some coupling between layers. A more advanced model would take this into account by using an adjustable coupling strength or radial sound velocity. As shown in Fig. 2-7, these two calculations approximately bound the measurements of NT1. Above about 15 K model A (weak wall coupling / thin wall) is a good fit to the unadjusted data [Fig. 2-7(a)]. However, below 15 K the nanotube specific heat decreases more quickly than the models, and below about 6 K, model B (strong wall coupling / thick wall) is a better fit to the unadjusted data. After adjustment for possible ice contamination, $C(T)$ is well-described by the strong-coupling/thick-wall limit for all temperatures above about 3 K [Fig. 2-7(b)].

Property	Symbol	Value		
Average sound velocity	v	2970 m/s		
Number density of primitive unit cells	η	1.87 x 10^{28}		
Boundary conditions	---	Free (radial and axial), Periodic (circumferential)		
Debye temperature	θ_D	235 K		
Einstein temperature	θ_E	550 K		
Number of atoms in the basis	b	6		
Average diameter	D	6.5 nm		
		A: weak wall coupling, no intertube modes	B: strong wall coupling, no intertube modes	C: strong wall coupling, yes intertube modes
Wall thickness	w	0.725 nm	2.5 nm	2.5 nm
Number density of intertube phonon modes	$\eta_{\text{intertube}}$	0	0	1.23 x 10^{25} m^{-3}
Maximum intertube phonon energy	$\theta_{\text{intertube}} = \hbar\omega_{\text{intertube}} / k_B$	na	na	0.6 K

Table 2-4. Properties used in modeling the specific heat of bulk and nanotubes, assuming 92.7% anatase and 7.3% ice by mass. "na"=not applicable.

Possible transition from 2D to 1D?

Around 3 K the average phonon wavelength becomes comparable to the nanotube circumference, and the model predicts another transition from 2D to 1D behavior [Fig 2-3(c)]. However, instead of the expected T^1 trend at the lowest temperatures, the data become essentially constant. Zero-dimensional behavior can be ruled out because λ is still much shorter than the nanotube length, and furthermore the 0D specific heat is known to fall off exponentially at low temperatures just like Einstein modes. The trend of flattening $C(T)$ at low T is present in all of the samples, suggesting that the underlying mechanism is not dependent on Na contamination or large amorphous fractions. One tentative explanation is the low

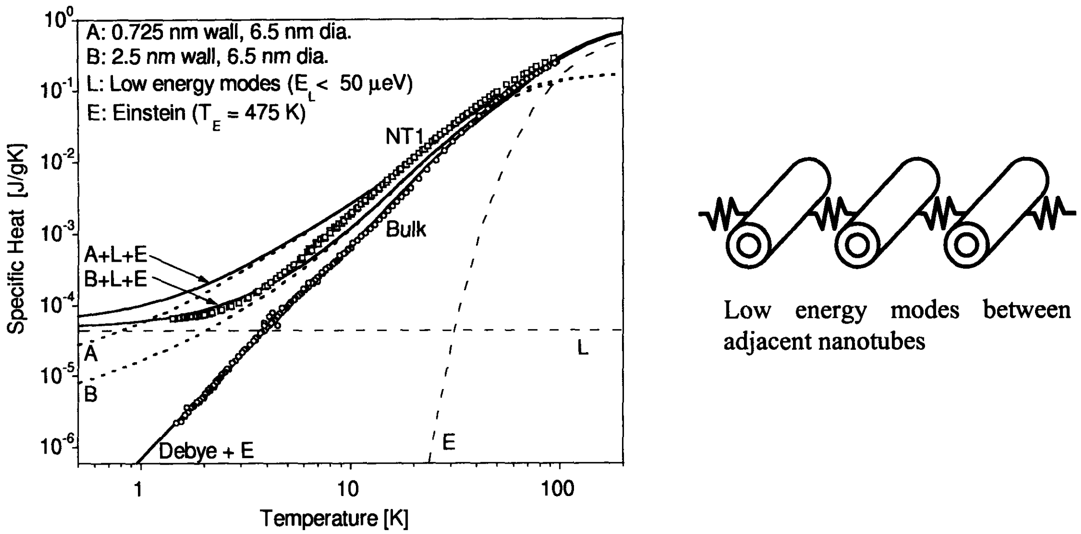

Low energy modes between adjacent nanotubes

Figure 2-8. Possible contribution to the specific heat from low-energy intertube phonons. These modes add a constant term indicated by the dashed line labeled "L", increasing the specific heat below about 2 K.

energy vibrations of nanotubes against their neighbors. Since this contribution appears to be a constant, if the intertube phonons are treated as Einstein modes, their characteristic temperature must be less than about 0.6 K, corresponding to an intertube coupling energy of less than 50 μeV. The solid lines in Fig. 2-8 show the effect of adding this sub-model for intertube modes. As indicated by the low-temperature end of the dashed line in Fig. 2-3(c), this regime would be a return to an effectively 3D regime. The concentration of intertube phonon modes is treated as an adjustable parameter, with the best agreement found for approximately one low energy mode per every 7200 atoms ($\eta_{intertube} = 1.23 \times 10^{25}$ m^{-3}).

The flattening in $C(T)$ is also reminiscent of that reported below about 0.6 K for single-walled CNT ropes [15-16], which was attributed to localized two-level systems of atomic rearrangement. The two-level system was thought to be the transitions of an individual carbon atom between two bi-stable sites, for example at a Stone-Wales (pentagon-heptagon) defect in the otherwise perfect hexagonal lattice. Although the anatase nanotube structure is quite different from CNT, similar atomic-level rearrangements might still occur near defects, and the fact that the anatase nanotubes with more amorphous character show greater enhancement at low T is consistent with this interpretation. A related explanation would be the rearrangement not of individual atomic bonds but rather of entire layers, by sliding which may be permitted by the weak interlayer bonds. Although we are unable to draw any firm conclusions from the data here, with further experiments on nanotubes of various diameters and wall thicknesses it might be possible to identify if either of these mechanisms is correct.

2.4 Summary

This portion of the thesis focused on modeling and experiments on low-dimensional phonons. The familiar Debye model for phonon dispersion was generalized to an elastic box of finite size. The resulting density of states and specific heat differ markedly from bulk. In particular, the specific heat at low temperature is proportional to T^n, where n is the dimensionality. Einstein modes and a Debye cutoff wavevector were also incorporated to make the model relevant for real materials over a wide range of temperatures. The model was also extended to thin-walled nanotubes. This model has no free parameters but requires as inputs the sound velocity, atomic number density, number of atoms in the basis, and geometry and boundary conditions of the sample. The most important feature of the model is that the phonons in a nanostructure transition from bulk to low-dimensional behavior when the average thermal wavelength is comparable to the nanostructure size, freezing out energy storage in that dimension.

The model was tested against measurements of anatase nanotubes from 1.5 to 95 K. The data show that the nanotube specific heat can be enhanced by more than an order of magnitude compared to bulk anatase. Two transitions are clearly observed which can be understood as changes in dimensionality. At about 50 K the average phonon wavelength is comparable to the wall thickness, and there is a transition from 3D to 2D behavior. At about 3 K an expected transition from 2D to 1D is obscured by a surprising flattening in the $C(T)$ curve, which may be due to low-energy intertube phonon modes (E_L<50 μeV), or to localized two-level systems of atomic and/or layer rearrangement. Quantitative interpretation of the experimental data was complicated by the likely presence of a contaminant, probably ice. Attempts to correct the data for ice contamination were particularly complicated at lower temperatures where a relatively larger fraction of the total specific heat is thought to be due to the contaminant, because the Debye temperature of ice is lower than that of anatase. Nonetheless, the results presented in this chapter confirm the guideline that transitions to low dimensionality can be determined by comparing the average phonon wavelength to the structure size, and that low dimensional systems can have a specific heat much larger than in bulk.

2.5 References

1. C. Dames, B. Poudel, W. Wang, J. Huang, Z. Ren, Y. Sun, J. I. Oh, C. Opeil, M. J. Naughton, and G. Chen, *Appl. Phys. Lett.* **87**, 031901 (2005).
2. C. Kittel, *Introduction to Solid State Physics*, 7th Edition (Wiley, 1996).
3. N. W. Ashcroft & N. D. Mermin, *Solid State Physics* (Harcourt, 1976).
4. R. G. Chambers, *Proc. Phys. Soc.* **78**, 941 (1961).
5. M. F. Modest, *Radiative Heat Transfer* (McGraw-Hill, 1993).
6. M. S. Dresselhaus and P. C. Eklund, *Adv. Phys.* 49, 705 (2000).
7. L. X. Benedict, S. G. Louie, M. L. Cohen, *Solid State Commun.* 100, 177 (1986).
8. V. Novotny and P. P. M. Meincke, *Phys. Rev. B* 8, 4186 (1973).
9. Y. Y. Chen, Y. D. Yao, S. S. Hsiao, S. U. Jen, B. T. Lin, H. M. Lin, and C. Y. Tung, *Phys. Rev. B* 52, 9364 (1995).
10. R. Lautenschlager, *Solid State Commun.* 16, 1331 (1975).
11. H. P. Baltes and E. R. Hilf, *Solid State Commun.* 12 369 (1973).
12. W. Yi, L. Lu, Z. Dian-lin, Z. W. Pan, and S. S. Xie, *Phys. Rev. B* 59, 9015 (1999).
13. A. Mizel, L. X. Benedict, M. L. Cohen, S. G. Louie, A. Zettl, N. K. Budraa, and W. P. Beyermann, *Phys. Rev. B* 60, 3264 (1999).
14. J. Hone, B. Batlogg, Z. Benes, A. T. Johnson, and J. E. Fischer, *Science* 289, 1730 (2000).
15. J. C. Lasjaunias, K. Biljakovic, Z. Benes, and J. E. Fischer, *Physica B* 316-317, 468 (2002).
16. J. C. Lasjaunias, K. Biljakovic, P. Monceau, and J. L. Sauvajol, *Nanotechnology* 14, 998 (2003).
17. V. N. Popov, *Phys. Rev. B* 66, 153408 (2002).
18. S. Zhang, M. Xia, S. Zhao, T. Xu, and E. Zhang, *Phys. Rev. B* 68, 075415 (2003).
19. M. Grätzel, *Nature* (London) **414**, 338 (2001).
20. B Poudel, W Z Wang, C Dames, J Y Huang, S Kunwar, D Z Wang, D Banerjee and Z F Ren, *Nanotechnology* **16**, 1935 (2005).
21. B. D. Yao, Y. F. Chan, X. Y. Zhang, W. F. Zhang, Z. Y. Yang, and N. Wang, *Appl. Phys. Lett.* **82,** 281 (2003).
22. H. Tsujii, B.Andraka, K. A. Muttalib, and Y. Takano, *Physica B* **329-333,** 1552 (2003).
23. P. Flubacher, A. J. Leadbetter, and J. A. Morrison, *J. Chem. Phys.* **33,** 1751 (1960).
24. J. S. Dugdale, J. A. Morrison, and D. Patterson, *Proc. Roy. Soc. A* (London) **224**, 228 (1954).
25. C. H. Shomate, *J. Am. Chem. Soc.* **69**, 218 (1947).
26. X. M. Wu, L. Wang, Z. C. Tan, G. H. Li, and S.S. Qu, *J. Solid State Chem.* **156**, 220 (2001).
27. P. H. Keesom and N. Pearlman, *Phys. Rev.* **112**, 800 (1958).

Chapter 3: Classical size effects on thermal conductivity

3.1 Introduction

In the last chapter we focused on the wave nature of phonons, and the quantum size effects that arise when phonons are confined in nanostructures that are comparable in size to the phonon wavelength in bulk. In this chapter we move on to study the particle nature of phonons, and the classical size effects that arise when phonons are confined in nanostructures that are comparable in size to the phonon mean free path in bulk. As pointed out in Chapter 1, these classical size effects can lead to thermal conductivities that are reduced by an order of magnitude or more compared to bulk. This reduced conductivity leads to potentially serious challenges in the thermal management of most nanowire devices, but is also of great benefit for the efficiency of nanowire thermoelectrics.

This chapter begins by considering the conditions for quantum size effects to be neglected. Fortuitously, it turns out that quantum size effects on phonons can indeed be neglected in many nanowire systems of practical interest, and in this limit we can safely treat the phonons as classical particles. Having made this considerable simplification, we then develop a model for the phonon thermal conductivity. The model is based on a spectral (frequency-dependent) form of kinetic theory, and includes several scattering mechanisms in bulk and nanostructures. In developing this model there is a tension between simplicity and accuracy. Here we pay particular attention to approximating the nonlinear phonon dispersion relations, and accounting for the frequency dependence of the various scattering mechanisms, while using as few adjustable parameters as possible. The resulting calculations of thermal conductivity are in good agreement with literature measurements of nanowires and superlattice nanowires, including diameters as small as 56 nm and reductions in thermal conductivity by more than 100-fold compared to bulk.

The analysis shows that we can expect significant reductions in thermal conductivity for nanostructures of sizes that are comparable to, or smaller than, the mean free path of phonons in bulk. However, we further show that it is important to consider the full range of mean free paths for bulk phonons, rather than lumping all of the bulk phonons into a single effective mean fee path. This point is quantified by deriving distribution functions for the range of mean free paths that contribute to thermal conductivity, showing that long mean free paths are more important for heat transfer than is commonly realized.

Portions of the work described in this chapter have appeared in previous publications [1-3].

(a) Wavelength vs. Diameter

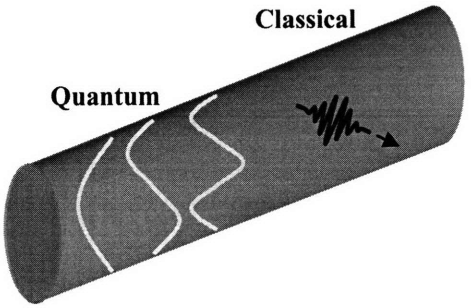

(b) Wavelength vs. Roughness
[Ziman]

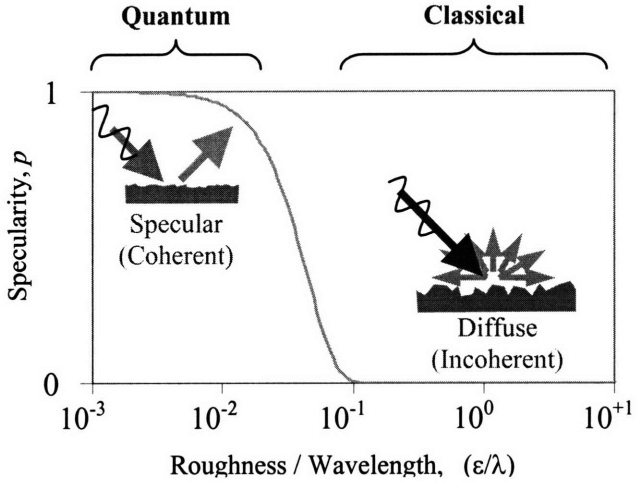

Figure 3-1. Transitions from quantum/wave to classical/particle behavior. (a) Comparison of wavelength and nanostructure size. When the nanostructure is much larger than the wavelength, phonons can be treated as wavepackets, corresponding to classical particles. (b) Comparison of wavelength and surface/interface roughness [Eq. (3-1)]. When the nanostructure surface is rough compared to the wavelength, phonons scatter diffusely ($p \to 0$) rather than specularly ($p \to 1$). This randomizes the phase of the scattered phonons, so that the resulting interferences are incoherent, again corresponding to classical particles.

3.2 Transition from quantum to classical behavior

In Chapter 2 we focused on the wave nature of phonons. Classical models for phonons, such as kinetic theory, are considerably easier to work with than quantum models, but classical models are only appropriate when the phonons can be treated as particles. To answer the important question of whether phonons are in the quantum or classical regime for size effects, there are two different mechanisms to consider, having to do with both the *size* and *roughness* of the nanostructure as compared to the average wavelength (Fig. 3-1).

3.2.1 Wavelength vs. diameter

The most obvious transition from wave to particle behavior occurs when the nanostructure size is much larger than the phonon wavelength [Fig. 3-1(a)]. In this regime we can consider isolated phonon wavepackets. Because each wavepacket is only a few wavelengths in size, it can travel around freely throughout the bulk of the nanostructure, scattering at the surfaces only occasionally. As the analysis of Chapter 2 showed, in such "large" nanostructures the confinement effects on the dispersion relation and density of states is negligible, and we can make the very important simplification of using the bulk dispersion relations to model the phonon transport. Each phonon wavepacket travels with the group velocity $\partial\omega/\partial q$ corresponding to its wavelength and polarization from bulk, where ω is the frequency of the phonon and q is its wavevector.

As we saw in Chapter 2, this transition is responsible for the onset of enhanced specific heat C at temperatures T below ~10 K for the TiO_2 nanotubes (Fig. 2-7). At high temperatures the average wavelengths are smaller than the nanotube wall thickness, so the confinement effects were unimportant and the phonon dispersion, density of states, and specific heat were all similar to bulk. Below ~10 K, the average wavelengths were long enough to be comparable to the nanotube wall thickness. This changes the phonon dispersion and density of states as shown in Fig. 2-1(d) of Chapter 2, leading to the enhanced specific heat. Thus the transition in $C(T)$ at ~10 K in Fig. 2-7(b) of Chapter 2 can interpreted as transition from quantum/wave behavior to classical/particle behavior. For these TiO_2 nanotubes, we would expect kinetic theory to be a good model for the phonon thermal conductivity well above ~10 K.

This guideline of comparing the phonon wavelength to the characteristic length of the nanostructure should be used with some caution, however, in systems where many surface scattering events can happen within the distance equivalent to one bulk mean free path. This is because surface scattering is elastic, preserving the phonon phase, so there is still the potential for coherent interference from multiple surface scattering events, until an inelastic bulk scattering event truly randomizes the phase. This concern is most common in superlattices, where previous work has shown that coherent wave interference effects may be important for the shortest periods [4, 5]. Localization is a related concern, especially for 2D and 1D systems at temperatures of ~1 K or below [6-9]. However, the equivalent localization mean free path for a nanowire (1D) is typically ~100-1000 times larger than the nanowire diameter [7-9], so this effect should only be important for smooth surfaces where the equivalent boundary scattering mean free path is even longer than the localization mean free path.

3.2.2 Wavelength vs. roughness

The other type of transition from wave to particle behavior is more subtle. Consider the scattering of a nearly monochromatic wave at a surface with some root-mean-square roughness ε. If the roughness is very small compared to the wavelength λ, then we expect the wave to reflect specularly, and if there is a second material on the back side of this smooth surface, we also expect there to be a transmitted wave obeying Snell's law. On the other hand, if the roughness is very large compared to the wavelength, then we expect both reflected and transmitted waves to scatter diffusely in all directions. Importantly, this diffuse scattering will also effectively randomize the phase of the reflected and transmitted waves that are scattered from different portions of the rough surface. If many such waves superpose with each other, there will be no net constructive or destructive interference, because there is no coherence between the different waves. Thus, in the limit of diffuse scattering we can also ignore the wave nature of the phonons, and treat them as particles (albeit with a random distribution of directions after scattering).

For intermediate levels of roughness, we can define a "specularity," p, as the fraction of incident phonons that are scattered specularly. (Thus $1-p$ is the fraction of phonons scattered diffusely.) The specularity can be estimated from the result of Berman, Ziman, and co-workers for a continuum [10-12] [Fig. 3-1(b)]

$$p = \exp\left(\frac{-16\pi^3\varepsilon^2}{\lambda^2}\right) \tag{3-1}$$

Although this relation was derived for a continuum, we expect the essential physics of a transition from diffuse to specular scattering to be similar for a discrete lattice. Equation (3-1) shows that the diffuse limit is reached ($p<0.01$) when the rms roughness is greater than about $\lambda/10$. We now show that this is usually true.

3.2.3 Most nanowires should behave classically

As we saw in Eq. (2-38) of Chapter 2, the typical thermal wavelength can be estimated from

$$\lambda T \approx 50\,\mathrm{nm\,K}\,(v/5000\,\mathrm{m/s}) \tag{3-2}$$

for an elastic continuum, where v is the sound velocity. For typical materials at 300 K, this estimated wavelength is only ~0.16 nm. However, for real materials a lower bound on the wavelength is approximately double the primitive lattice constant, for example, about 0.5 nm in bulk silicon. Thus, based on the comparison of diameter to wavelength, we expect the phonons in Si nanowires at 300 K to behave classically for diameters greater than $D\sim2.5$ nm ($D>5\lambda$). Similarly, for a 20 nm diameter Si nanowire, we would expect classical phonon behavior down to T~15 K.

Furthermore, most nanowires synthesized by either the vapor-liquid-solid method or by filling of alumina templates typically exhibit 1 or 2 nm of roughness [13-16], and even carefully grown epitaxial superlattices may have 1 - 3 monolayers of interface interdiffusion [17]. Because this roughness is greater than $\lambda/10$ at room temperature, we can expect the phonon scattering to be highly diffuse and incoherent. There is also some experimental evidence that diffuse scattering dominates nanostructures at temperatures of about 10 K and up [11, 12, 18, 19]. Thus, the comparison of roughness to wavelength further supports treating phonons classically in most realistic nanowires at typical temperatures of interest.

3.3 Spectral form of kinetic theory

In Chapter 1 we introduced the simplest form of kinetic theory for the thermal conductivity of a collection of phonons treated as particles,

$$k = \tfrac{1}{3} C v L_{eff} \tag{3-3}$$

where C is the specific heat, v the velocity, and L_{eff} the effective mean free path which incorporates bulk and boundary scattering through Matthiessen's rule:

$$L_{eff}^{-1} = L_{bulk}^{-1} + L_{boundary}^{-1} \tag{3-4}$$

Although the Matthiessen's rule assumption that the scattering mechanisms are independent of each other is rarely satisfied rigorously [20, 21] it is widely used with reasonable accuracy [10]. For more refined calculations, the Boltzmann transport equation is often used, where the boundary scattering is implemented as a boundary condition rather than a correction to the effective mean free path [10, 22].

The frequency-independent model of Eqs. (3-3) and (3-4) captures in a crude way the physics of phonon scattering in bulk materials and the additional scattering in nanostructures, including nanowires, superlattices, and superlattice nanowires (Fig. 3-2). However, it is well known that the properties of phonons in real solids have a strong frequency dependence. Therefore it is much better to use the spectral form of kinetic theory:

$$k = \tfrac{1}{3} \int C_\omega \, v \, L_{eff} \, d\omega, \tag{3-5}$$

Now the specific heat, group velocity, and mean free paths are all frequency-dependent:

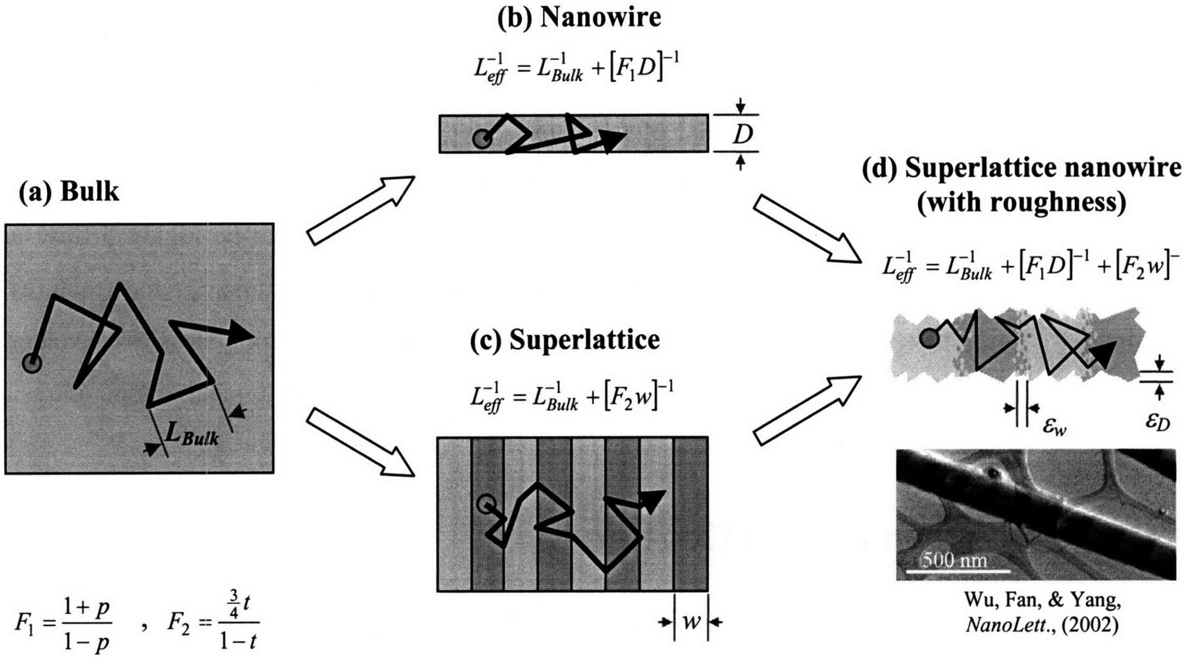

Figure 3-2. Boundary and interface scattering in nanowires, superlattices, and superlattice nanowires. The diameter and segment length act as boundary scattering terms which reduce the thermal conductivity in accordance with Matthiessen's rule [Eqs. (3-4) or (3-8)]. In a nanowire, the equivalent diameter $F_1 D$ is comparable to or smaller than the bulk mean free path L_{Bulk}. Similarly, a superlattice is characterized by an equivalent segment length $F_2 w$ that is comparable to or smaller than L_{Bulk}. In a superlattice nanowire both $F_1 D$ and $F_2 w$ are less than L_{Bulk}. The coefficients F_1 [Eq. (3-23)] and F_2 [Eq. (3-22)] depend on the specularity p and transmissivity t, which in turn depend on the phonon wavelength and the roughness at sidewalls (ε_D) and between segments (ε_w).

$$v(\omega) = \frac{\partial \omega}{\partial q} \tag{3-6}$$

$$C_\omega(\omega,T) = \hbar\omega \; DOS(\omega)\frac{\partial f(\omega,T)}{\partial T} \tag{3-7}$$

$$L_{eff}^{-1}(\omega,T) = L_{bulk}^{-1}(\omega,T) + L_{boundary}^{-1}(\omega) \tag{3-8}$$

Note that C_ω can be thought of as a specific heat per unit frequency.

To proceed further we need three pieces of information: the dispersion relation $\omega(q)$, the bulk mean free paths $L_{bulk}(\omega,T)$, and the boundary scattering mean free path $L_{boundary}(\omega)$. These inputs are discussed next.

3.3.1 Approximating dispersion relations

In Chapter 2 we used continuum elasticity to model bulk materials. This led to a linear dispersion relation, $\omega=vq$, which is a good approximation at low temperatures when only long-wavelength acoustic modes are excited. This simplification was also necessary so that the resulting low-dimensional dispersion relations could be easily derived and presented. Here we have argued that for most practical nanowire systems at reasonable temperatures, the quantum confinement effects on the dispersion relation can be neglected, so now we can afford to relax the assumption of linear dispersion and consider the true nonlinear dispersion relation more carefully.

The experimentally-measured phonon dispersion relation for bulk silicon is depicted in Fig. 3-3(a) [51, 52]. The longitudinal acoustic (LA) and transverse acoustic (TA) branches are shown again in Fig. 3-3(b) for the [100] and [111] directions. It is clear that the sound velocities of the two polarizations differs by about a factor of two, and that the assumption of linear dispersion is only valid for less than half of the first Brillouin zone. Figure 3-3(b) also depicts two approximations for the acoustic branches of the dispersion relation, the Debye and Born von Karman models, both of which are discussed below.

Debye dispersion

The Debye model, $\omega=vq$, is the simplest approximation for the real phonon dispersion relation. It is straightforward to extend kinetic theory to multiple phonon branches simply by summing over each polarization. In this case there would be three Debye branches: a single LA branch with the longitudinal sound velocity, and a doubly-degenerate TA branch with the transverse sound velocity. However, for simplicity it is sometimes desirable to combine these 3 branches into one, triply-degenerate branch with one effective sound velocity. Given literature values for the longitudinal and transverse speeds of sound, what is the best choice for the effective speed of sound? It turns out that the weighted average, $v_{eff}=\frac{1}{3}v_L+\frac{2}{3}v_T$, is not the best choice. Instead, by focusing on the limiting case of low temperature and long mean free path phonons, we can derive an analytical solution [3]. At low temperature the mean free path is limited by boundary scattering, and so is independent of phonon frequency. Furthermore, dispersion can be neglected and all of the phonons can be approximated as traveling at the sound velocity. Then the kinetic theory expression for thermal conductivity of these three phonon branches simplifies to

$$k=\frac{1}{3}\left[\frac{1}{3}CvL\right]_{LA}+\frac{2}{3}\left[\frac{1}{3}CvL\right]_{TA} \tag{3-9}$$

which we would like to equate to the effective expression

$$k=\left[\frac{1}{3}CvL\right]_{eff} \tag{3-10}$$

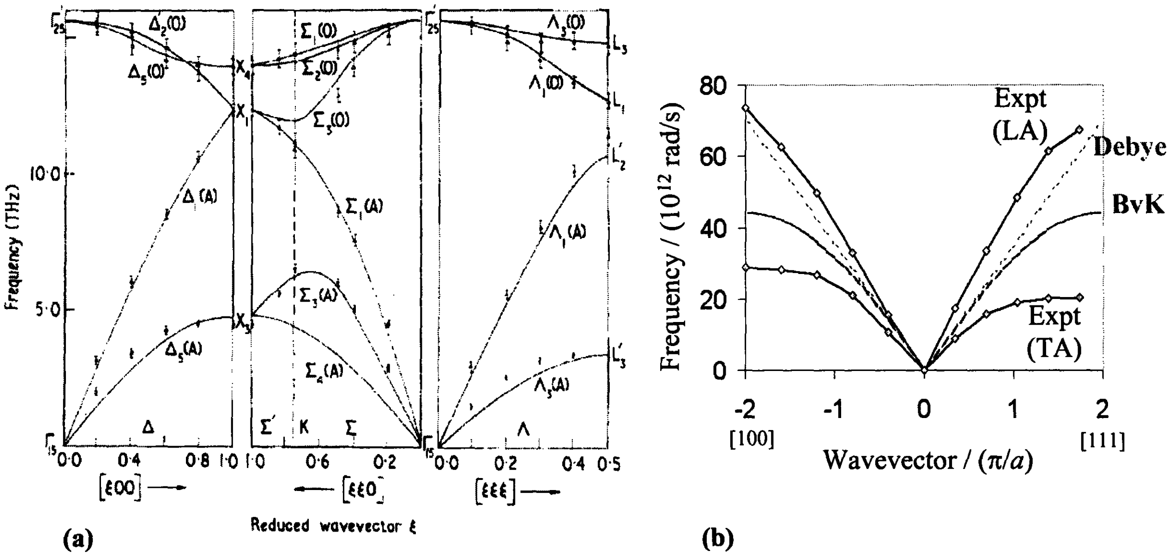

Figure 3-3. Phonon dispersion relations in bulk silicon. (a) Calculated [51] and experimental [52] phonon dispersion relation for bulk silicon. (b) Detail of the dispersion relations for the acoustic branches in the [100] and [111] directions, comparing the experimentally measured dispersion with both the Debye and Born-von Karman (BvK) approximations. The Born-von Karman approximation is much better than the Debye approximation at capturing the rolloff of the dispersion relation at high frequencies.

From the analysis in Chapter 2 of the density of states for bulk systems with linear dispersion, we know that the specific heat is proportional to v^{-3}:

$$C(T \to 0) = \frac{4\pi^4 k_B}{15}\left(\frac{k_B T}{\hbar v}\right)^3 \tag{3-11}$$

Substituting Eq. (3-11) into Eqs. (3-9) and (3-10) and canceling out constant terms including the boundary-limited mean free path yields

$$v_{eff}^{-2} = \tfrac{1}{3} v_L^{-2} + \tfrac{2}{3} v_T^{-2} \tag{3-12}$$

Thus, a better estimate for the effective sound velocity is

$$v_{eff} = \left(\tfrac{1}{3} v_L^{-2} + \tfrac{2}{3} v_T^{-2}\right)^{-1/2} \tag{3-13}$$

That is, we should take the weighted average of the inverse squares of the velocities, not of the velocities themselves, This will guarantee the correct limiting behavior at low temperature. For example, in silicon v_L is about 8973 m/s and v_T is about 5398 m/s (Table 1), each taken to be the average of the appropriate velocities in the [100], [110], and [111] directions. The effective velocity according to Eq. (3-13) is

Quantity	Units	Si	Ge	PbTe
k, at 300 K	W/mK	149	53	2.0
η, primitive unit cells	m^{-3}	2.50×10^{28}	2.21×10^{28}	1.45×10^{28}
v_{sL}, longitudinal	m/s	8973	5247	---
v_{sT}, transverse	m/s	5398	3267	---
v_s, effective average	m/s	6084	3662	1730
$\lambda_0=2\pi/q_0$	nm	0.55	0.57	0.66
$T_{\mathrm{Debye}}=\hbar v_s q_0 / k_B$	K	530	306	126
ω_0 / 2π, for Born-von Karman model	THz	7.02	4.06	1.68
A_1, impurity/alloy scattering	s^3	2.4×10^{-45} ($A_2=1.2 \times 10^{-42}$ for $Si_{0.9}Ge_{0.1}$)	---	4×10^{-42}
B_1, umklapp scattering	s/K	1.7×10^{-19}	---	6.2×10^{-18}
B_2, umklapp scattering	K	210	---	30
L_{Naive}, 300 K = $[3k/Cv]_{\mathrm{Lit}}$		5	---	3
L_{Tradl}, 300 K	nm	210	134	---
L_{10}, 300 K	nm	87	---	6
L_{50} (median MFP), 300 K	nm	580	---	42
L_{90}, 300 K	nm	12,800	---	860

Table 3-1. Basic parameters used in the modeling of the thermal conductivity of Si, Ge, and PbTe, with Born-von Karman dispersion relations [1-3]. Entries marked "---" are either unavailable or were not evaluated as part of this work.

v_{eff}=6084 m/s, and the resulting Debye dispersion is depicted by the dashed line in Fig. 3-3(b). For comparison, the direct weighted average is about 6590 m/s, which is about 8% too high (possibly an acceptably small error for these types of models).

Born-von Karman dispersion

Although the Debye dispersion gives satisfactory results for the specific heat at all temperatures, it leads to serious errors when calculating the thermal conductivity (except at temperatures well below the Debye temperature). This is because all Debye phonons have the same group velocity, namely the speed of sound, while it is clear from Fig. 3-3(b) that the acoustic phonon branches flatten out to a much lower group velocity for a significant portion of the dispersion relation, approaching zero group velocity at the boundary of the first Brillouin zone. This well-known phenomena is present even in the simplest model lattice of a 1D monatomic chain [20, 21]. In this "Born-von Karman" model the dispersion relation is

$$\omega = \omega_0 \sin\left(\frac{\pi q}{2q_0}\right) \tag{3-14}$$

where ω_0 and q_0 depend on the mass, stiffness, and atomic spacing of the model lattice. We now adapt this expression to approximate a dispersion relation in 3D. Although in general ω_0 and q_0 could be treated as adjustable parameters to give the best fit to experimental dispersion relations, we can define them uniquely from well-known material properties without any fitting. First, to ensure the correct number of phonon modes, q_0 is simply the Debye cutoff wavevector:

$$q_0 = \left(6\pi^2\eta\right)^{1/3} \tag{3-15}$$

where η is the number density of primitive unit cells. Then, we define ω_0 to ensure the correct limiting behavior at low temperature. In this limit only small-q phonons are active, and Eq. (3-14) reduces to the linear form:

$$\omega = \left(\frac{\pi\omega_0}{2q_0}\right)q \tag{3-16}$$

Thus, the term in parentheses should simply be the sound velocity, requiring

$$\omega_0 = 2vq_0/\pi \tag{3-17}$$

Finally, substituting Eqs. (3-15) and (3-17) into Eq. (3-14), the Born-von Karman dispersion can be expressed as

$$\omega = \frac{2v}{\pi}\left(6\pi^2\eta\right)^{1/3} \sin\left(\frac{\pi q}{2\left(6\pi^2\eta\right)^{1/3}}\right) \tag{3-18}$$

For dispersions with multiple branches, this velocity should be averaged according to Eq. (3-13), just like the Debye model. Alternatively, for slightly improved accuracy, the longitudinal and transverse branches could each be fit separately, and the thermal conductivity of each branch treated separately as in Eq. (3-9)

The Born-von Karman (or "sine-type") dispersion relation of Eq. (3-18) is also depicted in Fig. 3-3(b). Notice how it lies naturally in between the experimental LA and TA branches over the entire dispersion relation. The Born-von Karman dispersion is just as easy to specify as the Debye dispersion, requiring only η and v as inputs. However, the Born-von Karman dispersion gives a much better approximation to the high-frequency rolloff seen in the full, experimental dispersion relations, and so it is strongly preferred over the Debye dispersion for calculations involving transport [3].

Besides the Born-von Karman dispersion, several other approaches have been used to approximate the high-frequency rolloff of acoustic phonons, including a two-segment piecewise-linear fit [23] and a truncated Debye model [24], but these are not considered further here.

3.3.2 Scattering mechanisms

Bulk mean free paths

The two most important scattering mechanisms in typical bulk materials are impurity/alloy scattering and phonon-phonon umklapp scattering:

$$L_{bulk}^{-1}(\omega,T)=L_{imp}^{-1}(\omega)+L_{umkl}^{-1}(\omega,T) \tag{3-19}$$

Impurity / alloy scattering

Impurity (and alloy, when present) scattering is usually calculated using the fourth-power dependence of Rayleigh scattering,

$$L_{imp}^{-1}=A_1\omega^4/v\,, \tag{3-20}$$

where A_1 is a fitting parameter which may also be estimated from other properties [25].

Umklapp (phonon-phonon) scattering

There is no uniformly accepted expression for Umklapp scattering, but one common form is [26]

$$L_{umkl}^{-1}=B_1\omega^2T\exp(-B_2/T)/v \tag{3-21}$$

where B_1 and B_2 are fitting parameters. Recent work based on molecular dynamics simulations of umklapp scattering supports the ω^2 dependence of Eq. (3-21) and may also be able to give a more accurate relationship overall [27].

Boundary scattering mean free paths

Transport perpendicular to interfaces

Superlattices and thin films are the model systems for studying transport perpendicular to interfaces, and are of great interest as thermoelectric materials [1, 28-30]. The emerging understanding, reviewed elsewhere [22, 31-33], is that most systems can be explained by the action of incoherent phonon particles scattering sequentially at isolated interfaces. In this view a superlattice is a set of thin films connected by boundary resistances. As mentioned at the beginning of the chapter, coherent interference and localization effects can also play a role for thin, smooth layers, at low temperatures and for materials with long bulk mean free paths. These wave effects are not considered further here. Because of the boundary resistance, the thermal conductivity is well below the simple average based on the Fourier law of heat conduction, and can fall below the alloy limit and even below theories of minimum thermal conductivity [32, 34-36] In this regime the thermal conductivity is proportional to the superlattice period, indicating that the classical size effect of interface scattering dominates the mean free path. A simple energy transmissivity picture yields the following expression for the boundary scattering mean free path perpendicular to superlattice interfaces [3]

$$L_{bdy,SL} = \frac{\frac{3}{4} wt}{(1-t)} \tag{3-22}$$

where w is the thickness of superlattice layers (e.g. half of the period), and t is an energy transmissivity, which may depend on frequency. Understanding the details of this interfacial scattering is a difficult and ongoing research challenge, leading to techniques such as the acoustic mismatch model [37], diffuse mismatch model [37], maximum transmission model [3], lattice dynamics, molecular dynamics, and an adjustable balance between specular and diffuse scattering. To minimize the thermal conductivity perpendicular to interfaces, the transmissivity should be minimized. For materials with weak acoustic contrast, the interfaces should be made rough to maximize the diffuse scattering. Ideal wave calculations predict that materials with strong acoustic contrast have high reflectivity, including the total internal reflection of phonons with high incident angles which effectively cuts them off from participating in heat transport. For these high acoustic contrast materials the overall reflectivity may actually be maximized for specular rather than diffuse interfaces. There are additional complications as the superlattice period becomes very short (~ 3-5 unit cells), where tunneling and coherent wave effects start to become important and there is a slight recovery in the thermal conductivity [38-40]. Modeling in this regime is even more complicated but has been addressed by models allowing for partial phonon coherence [4, 5].

Transport parallel to interfaces

Transport parallel to interfaces is important for thermoelectric nanowires [41, 42] and the in-plane direction of superlattices [28] and thin films. The essential difference compared to cross-plane transport is that for transport parallel to interfaces, specular scattering is not effective at reducing the phonon momentum in the direction of transport. For axial transport in a cylindrical nanowire, the effective mean free path due to boundary scattering is given by [10]

$$L_{bdy,D} = D\left(\frac{1+p}{1-p}\right) \tag{3-23}$$

where p is the specularity parameter given in Eq. (3-1). As noted previously, $p \approx 0$ because of the roughness in most realistic nanowires, so this mean free path is typically simply equal to the diameter. In the opposite limit of specular sidewalls, this mean free path diverges, because specular reflections do not impede the axial phonon transport. Eq. (3-23) applies to an infinitely long circular wire, but can be applied to an infinitely long square wire of side a by replacing D with $1.12a$ [43]. Corrections also exist for the effects of finite sample length, which leads to reduced thermal conductivity [11, 12].

3.3.3 Modeled thermal conductivity of nanostructures

The sequence of steps in a typical modeling calculation are summarized in Fig. 3-4, which is a good summary of the entire chapter. For a new material, the initial inputs to the calculation are literature values for the thermal conductivity as a function of temperature, and also some approximation to the true dispersion relation. Here we focus on the Born-von Karman approximation, which requires the sound velocity and number density of primitive unit cells as inputs. Optical modes are ignored in this approximation because of their small group velocity. Using the spectral kinetic theory model of Eqs. (3-5) through (3-8) and (3-19) through (3-21), values of A_1, B_1, and B_2 are determined to give the best fit to the bulk thermal conductivity $k(T)$ over the entire temperature range (Fig. 3-5). For this example, the optimized values for Si are $A_l = 2.4 \times 10^{-45}$ s^3, $B_l = 1.73 \times 10^{-19}$ s/K, and $B_2 = 210$ K (Table 3-1). The fitting often requires a 4th parameter at low temperature, corresponding to the sample size, because literature reports on the thermal conductivity are still subject to boundary scattering at low temperatures. The resulting mean free paths for bulk silicon are depicted in Fig. 3-6, along with a typical nanowire diameter of 83 nm. It is clear that the nanowire boundary scattering is much stronger than the bulk scattering mechanisms for low frequency phonons, but high frequency phonons will also be affected by impurity scattering and, at higher temperatures, umklapp scattering.

Silicon nanowires

Having fixed all of the adjustable parameters, the next step in the modeling is to input the nanowire diameter and roughness to Eq. (3-23) and calculate the effective mean free path of Eq. (3-8). As mentioned previously, the specularity p is expected to be negligibly small for most practical nanowires and temperatures, so in practice the only input is the nanowire diameter. As shown in Fig. 3-7, this model gives fairly good agreement for literature measurements of silicon nanowires of diameter 56 nm and 115 nm [44]. At low temperature the model underpredicts the thermal conductivity of the 56 nm silicon nanowire by up to ~50%, but is better for the 115 nm diameter nanowire, and the agreement is excellent for both diameters above ~150 K. The reasons for the underprediction are not known, but it could be

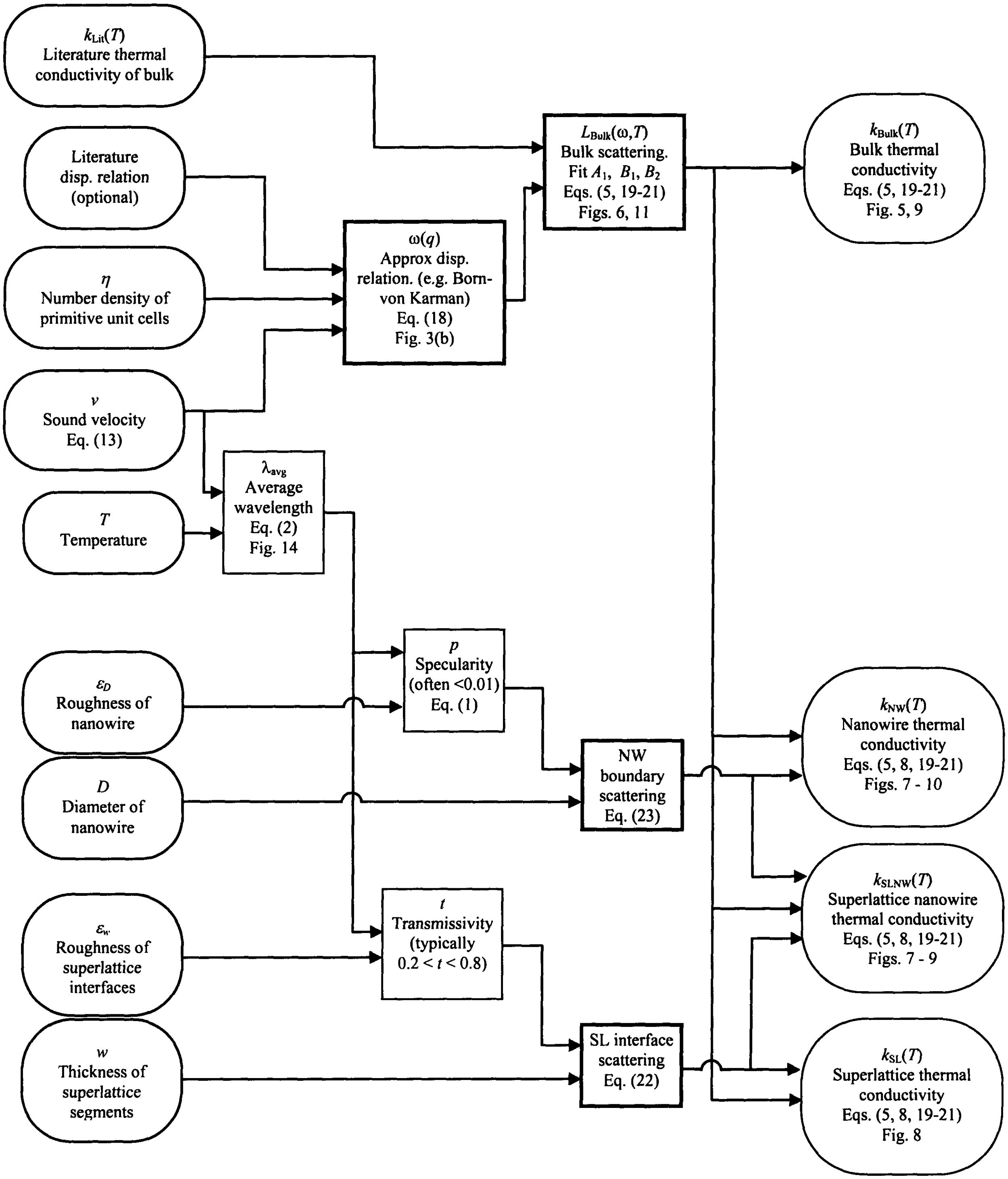

Figure 3-4. Detailed flowchart for modeling the phonon thermal conductivity of nanowire, superlattices, and superlattice nanowires, assuming the phonons can be treated as classical particles.

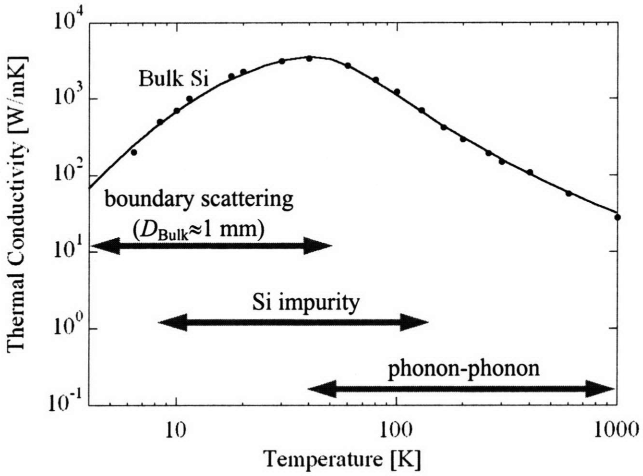

Figure 3-5. The thermal conductivity of bulk silicon [49], fit with the spectral kinetic theory model described in the text. The important regime for each scattering mechanism has been indicated approximately.

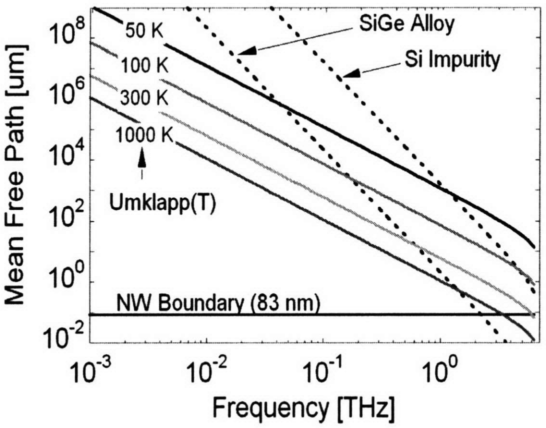

Figure 3-6. The frequency dependence of the phonon mean free paths for various scattering mechanisms in bulk silicon at various temperatures [2]. For comparison, the boundary scattering due to a typical nanowire diameter of 83 nm is also shown. In this example the boundary scattering is the most important scattering mechanism, with additional scattering of high-frequency phonons by impurity scattering and, at high temperatures, umklapp scattering.

caused by the true nanowire diameters being larger than reported, or the nanowire boundaries having finite specularity (p>0).

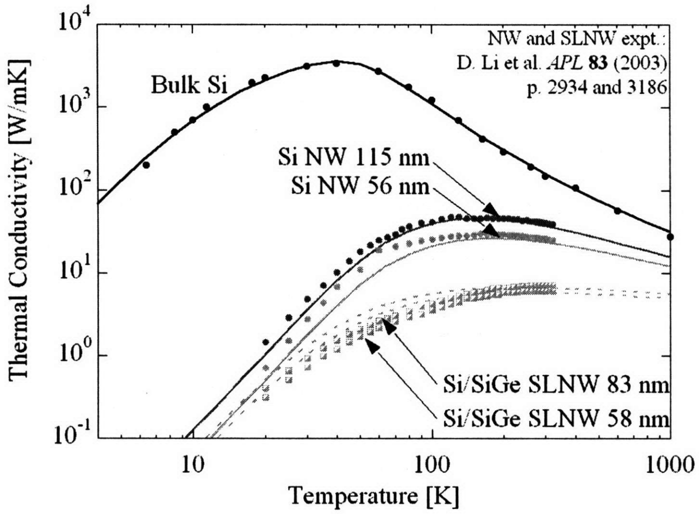

Figure 3-7. Modeled thermal conductivity of silicon nanowires (NW) and Si/SiGe superlattice nanowires (SLNW), compared with experimental data from the literature [44, 45]. Boundary scattering reduces the thermal conductivity of the nanowires over the entire temperature range, and at 20 K the thermal conductivity of the nanowires is reduced by more than 100-fold compared to bulk Si. Compared to the pure Si nanowires, the superlattice nanowires show additional reductions in thermal conductivity. This is not due to interface scattering between segments, but rather due to alloy scattering within the SiGe segments.

Si/SiGe superlattice nanowires

To extend the model from a nanowire to a superlattice or superlattice nanowire, the next step is to input the superlattice period and transmissivity to Eqs. (3-17) and (3-8). We have applied this calculation to the $Si/Si_{1-x}Ge_x$, (x~0.05-0.10) superlattice nanowire shown in Fig. 3-2 [16]. Because the Ge concentration in the SiGe segment is relatively small, there is not much acoustic contrast between the two segment types. Thus the transmissivity t is close to unity, and $L_{\mathrm{bdy},SL}$ should be large enough to be unimportant (that is, the scattering rate proportional to $L_{bdy,SL}^{-1}$ is negligibly small). Because of the uncertain stochiometry of the $Si_{1-x}Ge_x$ segment, it is, however, necessary to introduce another fitting parameter to account for the alloy scattering. This alloy scattering has the same form as the impurity scattering expression of Eq. (3-20), but with a different coefficient A_2. Using the same values for A_1, B_1, and B_2 determined previously, the best value for the alloy parameter A_2 was found to be 1.19 x 10^{-42} s^3. This value for A_2 is close to what would be predicted with standard theory for $Si_{0.9}Ge_{0.1}$ [25]. As shown in Fig. 3-7, the resulting model calculations again compare favorably with the experimental values from the literature [45], especially at temperatures above ~150 K. A comparison of the 56 nm nanowire and the 58 nm superlattice nanowire reveals that the additional alloy scattering is very important over most of the temperature range considered, although it becomes less important below ~20 K. This is because low temperature phonons have lower frequencies, so both alloy/impurity and umklapp scattering become weaker (Fig. 3-6). Thus the only scattering mechanism remaining at low temperature is boundary scattering, which is independent of the level of alloying.

Regime map

The thermal conductivity of nanowires, superlattices, and superlattice nanowires can be nicely summarized by a regime map indicating the relative importance of bulk vs. nanostructure scattering mechanisms as a function of segment length and diameter (Fig. 3-8).

As shown in the top half of Fig. 3-8(a), for a rough-walled nanowire ($p \approx 0$) the transition from bulk to nanowire behavior occurs when the diameter becomes smaller than the bulk mean free path. For nanowires with smooth walls, the specularity p may become appreciable, in which case the transition from bulk to nanowire behavior will be suppressed to smaller diameters. In the limit of perfect specularity ($p \to 1$), the nanowire regime cannot be accessed no matter how small the diameter.

Similarly, the right half of Fig. 3-8(a) shows that for a superlattice with average energy transmissivity ($t \approx 1/2$), the transition from bulk to superlattice behavior occurs when the superlattice segment length becomes smaller than $\frac{4}{3}$ of the bulk mean free path. However, in the limit of perfect transmissivity ($t \to 1$), the superlattice regime cannot be accessed no matter how small the period.

A quantitative example of this regime map calculation is shown in Fig. 3-8(b) for a Si/Ge system. This calculation assumes diffuse scattering at the sidewalls and interfaces and uses Born-von Karman dispersion relations, but neglects the spectral dependence of the mean free paths. Some of the modeling parameters are given in Table 3-1. It is clear from the figure that the nanowire and/or superlattice effects become very important when the diameter and/or segment length becomes ~300 nm or less. This is expected because it is the order of magnitude of the bulk mean free path in both Si and Ge. The important issue of estimating these bulk mean free paths is taken up in the next section.

Sensitivity analysis

To gain a more complete understanding of the contribution of each phonon scattering mechanism over the entire temperature range, we have performed a sensitivity analysis which is depicted in Fig. 3-9.

The best fits of Fig. 3-7 are repeated in Fig. 3-9(a). The dashed lines of Fig. 3-9(b) show the effect of uniformly scaling all of the diameters by a factor of 1.5. For example, how would the modeled thermal conductivity change if the 56 nm nanowire were replaced with either an 84 nm (56 nm x 1.5) or 37 nm (56 nm / 1.5) nanowire? This plot shows that the diameter scattering effect is important in all of

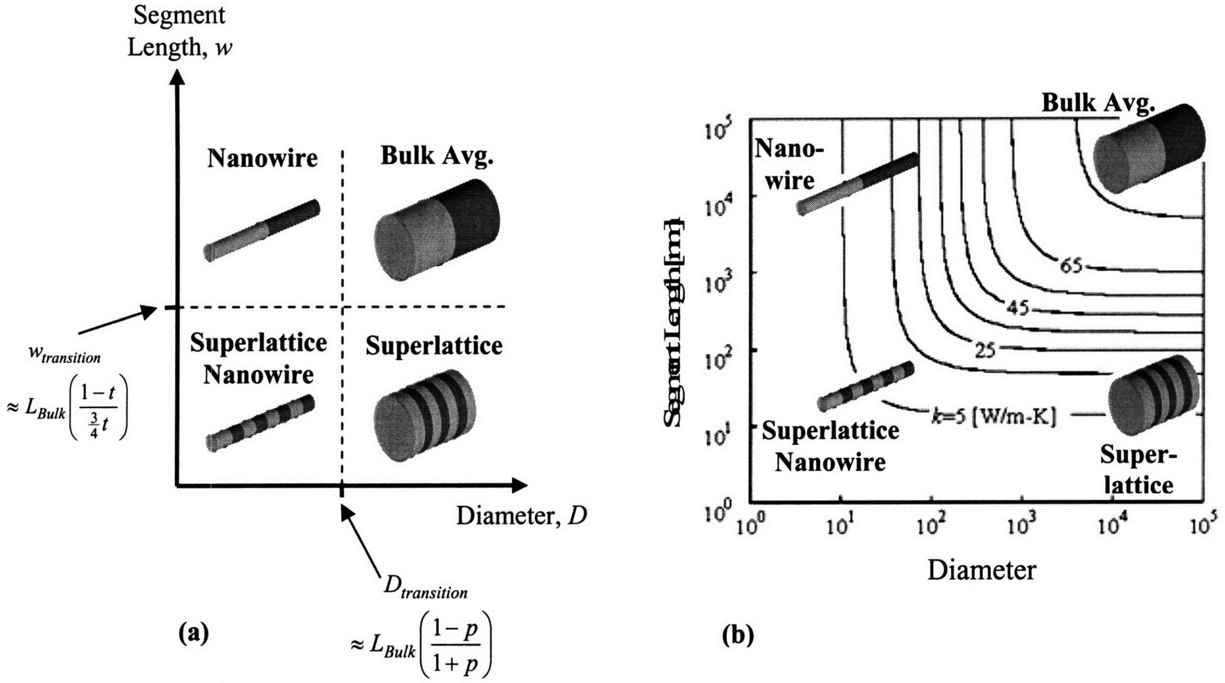

Figure 3-8. (a) Generalized regime map for the thermal conductivity of a superlattice nanowire, as a function of diameter, segment length, sidewall specularity p, and interface transmissivity t. Four limiting cases are apparent: bulk, nanowire, superlattice, and superlattice nanowire. (b) A particular regime map for Si/Ge segments at 300 K. The lines are contours of constant thermal conductivity ("isoconductivity lines"). The calculation in (b) assumes diffuse scattering at sidewalls (p=0) and a diffuse mismatch model for t, and neglects the frequency dependence of the mean free paths [3].

the nanowires, especially at lower temperatures, and also that the bulk silicon data used here is also sensitive to boundary scattering below ~50 K.

Similarly, the dashed lines of Fig. 3-9(d) show the effect of scaling the Umklapp parameter B_2 [Eq. (3-21)] by a factor of 2. For bulk Si the effect is to shift the location of the peak in $k(T)$. The Si nanowires also show some sensitivity to this parameter, while the Si/SiGe superlattice nanowires are not affected at all. Fig. 3-9(c) shows the effect of scaling the Umklapp parameter B_1 [Eq. (3-21)] by a factor of 1.5. Taken together, panels (c) and (d) show that Umklapp scattering is very important for bulk Si above ~50 K, is somewhat important in these Si nanowires above ~150 K, and is negligible for the Si/SiGe superlattice nanowires at all temperatures. Finally, the dashed lines of Figs. 3-9(e) and 3-9(f) show the effect of scaling the impurity (A_1) and alloy (A_2) scattering parameters, respectively, by a factor of 2. Impurity scattering is only important for bulk Si in the intermediate temperature range ~10-100 K, but is negligible for the nanowires and superlattice nanowires. As expected, alloy scattering is much stronger than impurity scattering, and makes a significant contribution to the superlattice nanowire thermal resistance above ~30 K.

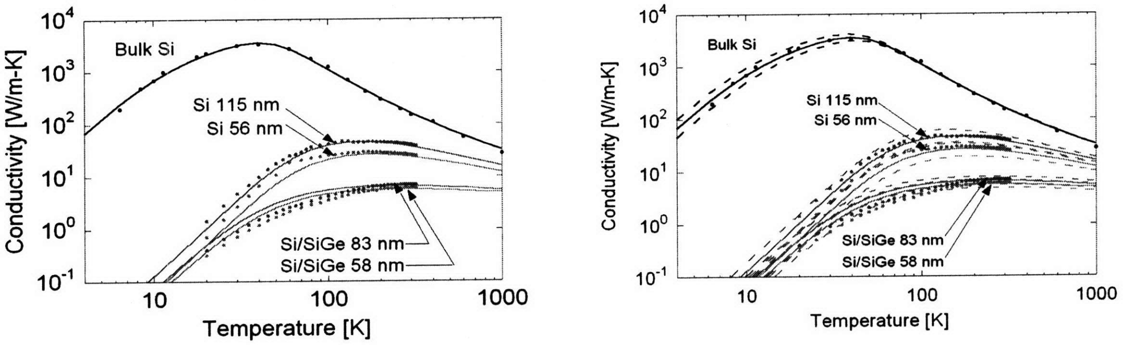

(a) Best Fits

(b) Vary Diameter by 1.5 x

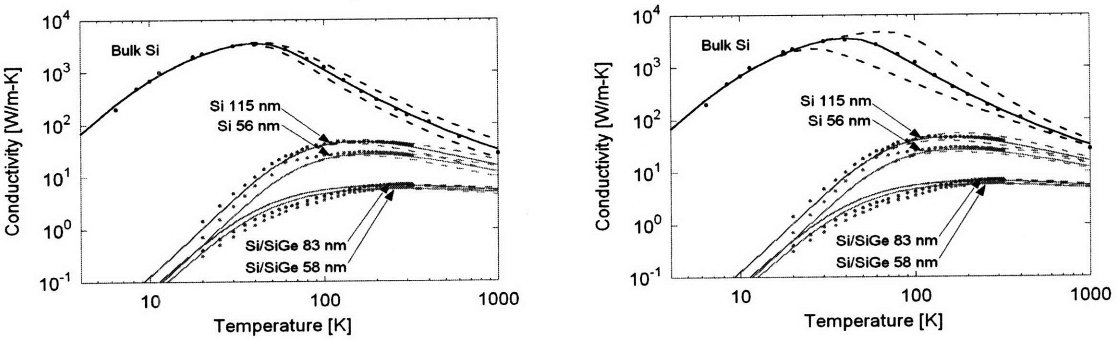

(c) Vary Umklapp B_1 by 1.5 x

(d) Vary Umklapp B_2 by 2 x

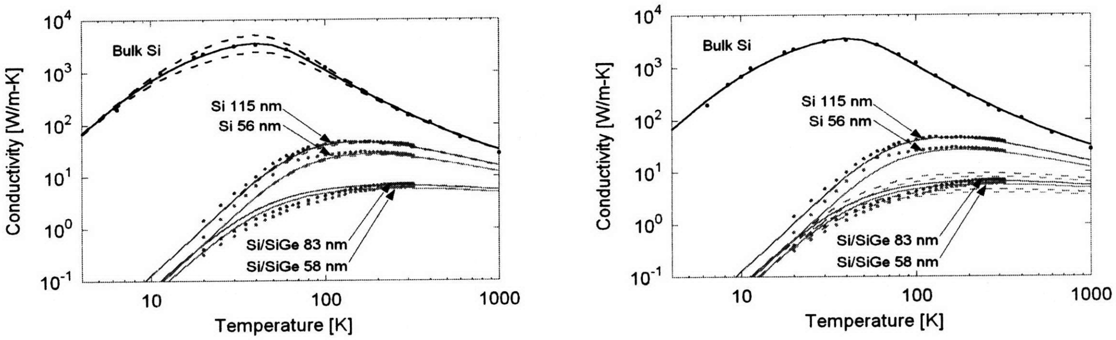

(e) Vary Si impurity A_1 by 2 x

(f) Vary SiGe alloy A_2 by 2 x

Figure 3-9. Sensitivity analysis of the modeled thermal conductivity for silicon nanowires and superlattice nanowires, isolating the effects of each of the fitting parameters. [2]. (a) Best fits, repeated from Fig. 3-7. (b) Multiplying and dividing the diameter by a factor of 1.5, to show where boundary scattering is important. (c&d) Varying the umklapp parameters B_1 and B_2 by a factor of 1.5, to show where phonon-phonon scattering is important. (e) Varying the Si impurity parameter A_1 by a factor of 2. (f) Varying the SiGe alloy parameter A_2 by a factor of 2 (only relevant for the Si/SiGe superlattice nanowire).

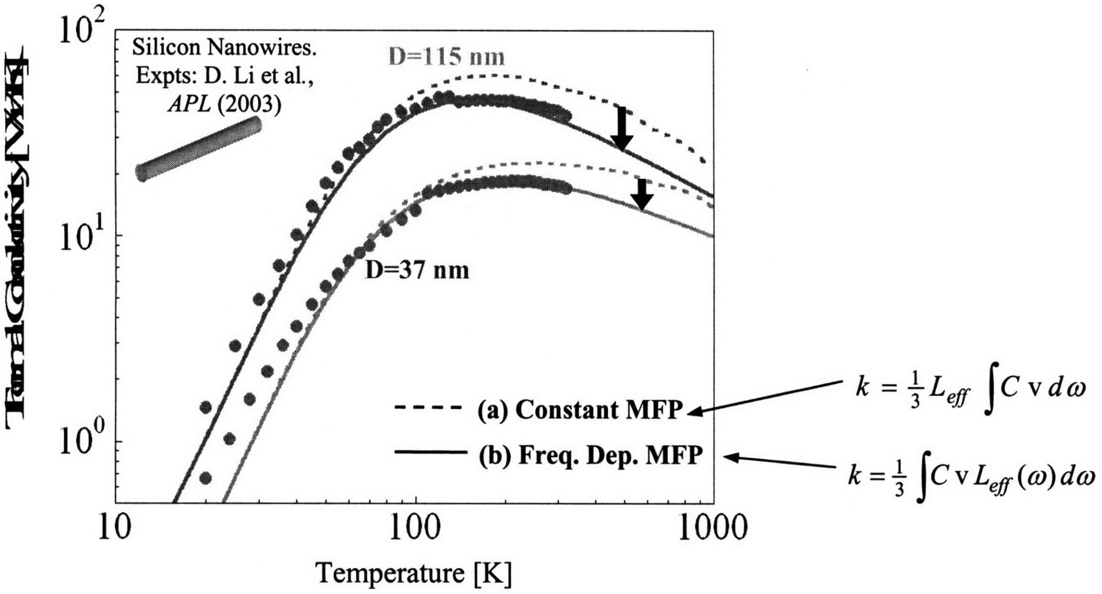

$k = \frac{1}{3} L_{eff} \int C \, \mathrm{v} \, d\omega$

$k = \frac{1}{3} \int C \, \mathrm{v} \, L_{eff}(\omega) \, d\omega$

Figure 3-10. Modeled thermal conductivity of silicon nanowires assuming (a) frequency-independent and (b) frequency-dependent mean free paths. It is important to consider the frequency dependence in order to capture the full reduction in thermal conductivity at temperatures where both boundary scattering and umklapp scattering are important.

Effect of assuming frequency-independent mean free path

To emphasize the importance of the spectral nature of the mean free paths, we have performed the same calculation with and without the frequency dependence of the mean free paths. For the frequency-independent calculation, the effective mean free path was found from Matthiessen's rule:

$$L_{eff}^{-1}(T) = L_{bulk}^{-1}(T) + D^{-1}, \tag{3-24}$$

The average bulk mean free path was estimated using the Born-von Kaman dispersion for C and v and literature values for the thermal conductivity, from

$$L_{bulk}(T) = \frac{k_{Lit}(T)}{\frac{1}{3} \int C v d\omega} \tag{3-25}$$

which is about 210 nm for silicon at 300 K. As shown in Fig. 3-10, treating the mean free path as constant leads to thermal conductivity predictions that are up to ~50% larger than experiment above ~100 K. The frequency-dependent model is in much better agreement with experiment above 100 K, and still in good agreement at lower temperatures. We will see later that part of the problem is that the average bulk mean free path from Eq. (3-25) is too small: most of the phonons in the bulk material have mean free paths much longer than 210 nm, and so boundary scattering is more important than we might otherwise expect.

3.4 The importance of various mean free paths

The regime map of Fig. 3-8(a) shows that the transition from bulk to nanowire (or superlattice) behavior is determined by comparing the bulk mean free path to the characteristic length of the nanostructure. A very important question is: what is the best estimate for the bulk mean free path?

A simple but naive estimate is to calculate the bulk mean free path from the sound velocity and literature value of specific heat in a lumped sense [Fig. 3-11(a)],

$$L_{Naiive} = \frac{k_{Lit}}{\frac{1}{3} C_{Lit} v_s} . \tag{3-26}$$

However, the group velocity and bulk mean free path are both strongly spectral quantities. In particular, most phonons travel far slower than the speed of sound, so the true mean free path should be much longer than the naive estimate of Eq. (3-26). It is now becoming common in the literature to perform some kind of averaging similar to Eq. (3-25). We refer to this as the "traditional" estimate for the mean free path:

$$L_{Tradl}(T) = \frac{k_{Lit}(T)}{\frac{1}{3} \int C v d\omega} , \tag{3-27}$$

which typically results in estimates from 200-300 nm [Fig. 3-11(b)]. However, we saw from Fig. 3-10 that using this traditional mean free path estimate fails to capture the full reduction in thermal conductivity, while performing the frequency integration does.

3.4.1 Thermal conductivity distributions per unit mean free path

To better understand the potential for thermal conductivity reduction by boundary scattering, it is important to understand the full *range* of mean free paths that contribute to heat transfer in a bulk material [1]. The greater the fraction of heat carried by phonons with long mean free paths in the bulk material, the greater the potential reduction in the thermal conductivity in a given nanostructure. This effect can be quantified by changing variables in the kinetic theory expression [Eq. (3-5)], to integrate over the mean free path rather than the frequency as the independent variable [Fig. 3-11(c)]:

$$k = \int_0^\infty k_\omega \, d\omega \quad \Rightarrow \quad k = \int_0^\infty k_L \, dL \tag{3-28}$$

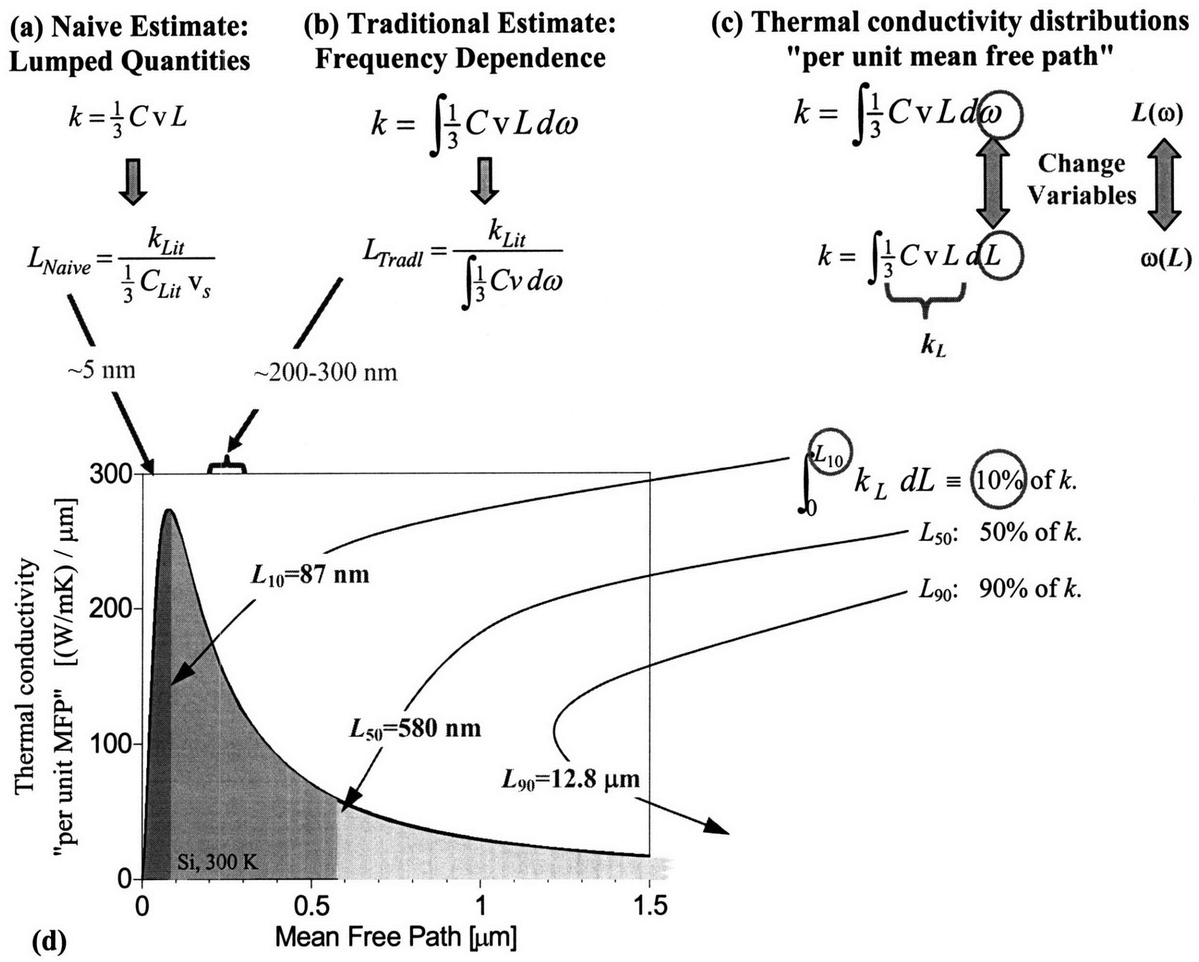

Figure 3-11. Estimating mean free paths in bulk silicon at 300 K. (a) Naive estimate using literature values for thermal conductivity, specific heat, and sound velocity. (b) Improved traditional estimate, using a modeled dispersion relation for C and v. (c,d) Thermal conductivity distributions per unit mean free path. The area of the darkest shaded region, from 0 to L_{10} (87 nm), equals 10% of the total thermal conductivity. Similarly, the area between 0 and L_{50} (580 nm) equals 50 % of the total.

where the integrand changes from

$$k_\omega = \tfrac{1}{3}\hbar\omega \frac{q^2}{2\pi^2}\frac{\partial f}{\partial T} L \tag{3-29}$$

to

$$k_L = -\tfrac{1}{3}\hbar\omega \frac{q^2}{2\pi^2}\frac{\partial f}{\partial T} L \frac{d\omega}{dL} \tag{3-30}$$

The negative sign in Eq. (3-30) comes about from changing the limits of integration, and will be canceled because $d\omega/dL$ is negative (small ω corresponds to large L, and vice versa). Recall that f is the Bose-

Einstein factor and q is the wavevector, which can be uniquely related to ω. We are assuming isotropic properties, and this derivation also takes advantage of the fact that the density of states in 3D is given by

$$DOS = \frac{q^2}{2\pi^2 v} \tag{3-31}$$

To proceed further, the dispersion relation $\omega(q)$ and the spectral mean free paths $L(\omega)$ are necessary. For the sake of illustration, we have performed calculations using the Born-von Karman dispersion for both Si and PbTe. Using the umklapp and impurity/alloy scattering expressions described previously, the parameters A_1, B_1, and B_2 were calculated by fitting literature data for the temperature-dependent thermal conductivity of bulk Si and PbTe (Table 3-1). [46-49]. In these materials, umklapp scattering is dominant at most temperatures of interest for thermoelectric applications. Impurity scattering is only important at lower temperatures, near the peak in $k(T)$. When present, alloy scattering can be important at all temperatures.

The quantity k_L, which can be termed a "thermal conductivity per unit mean free path," is best interpreted as a weighting function for the relative importance of various mean free paths in contributing to the total thermal conductivity. To the best of my knowledge we are the first to present this concept [1]. A representative distribution of this thermal conductivity per unit mean free path is shown in Fig. 3-11(d) for bulk Si at 300 K. Notice how broad the distribution is, and specifically how far the tail extends beyond the naive (5 nm) and traditional (200-300 nm) estimates.

3.4.2 Cutoff mean free paths

A deeper understanding of the *range* of important mean free paths is achieved by defining a cutoff mean free path L_α, which accounts for a fraction α of the total heat flux. These cutoff mean free paths are defined by

$$\alpha \equiv \frac{\int_0^{L_\alpha(T)} k_L(T)\,dL}{\int_0^{\infty} k_L(T)\,dL} = \frac{\int_0^{L_\alpha(T)} k_L(T)\,dL}{k(T)}. \tag{3-32}$$

For example, the area under the curve of Fig. 3-11(d) from L=0 to L=87 nm accounts for 10% of the total area. Thus, for L=87 nm, α=10%, so we have determined that L_{10}=87 nm for bulk Si at 300 K. Similarly, integrating from 0 to 580 nm yields 50% of the total area, so L_{50}=580 nm. Notice that this median mean free path is 2 or 3 times larger than the traditional estimates. Even more important is the quantification of the long tail of the distribution. To capture 90% of the total thermal conductivity in this example, we

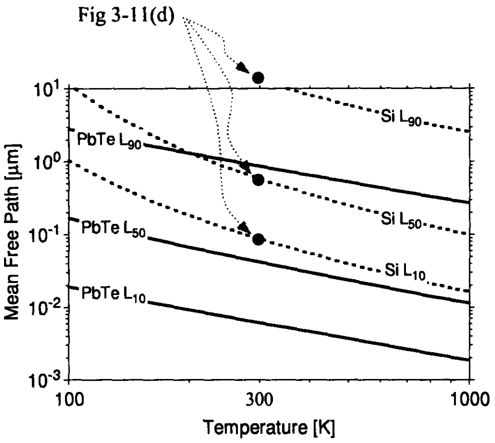

Figure 3-12. The temperature dependence of the range of mean free paths that are important for carrying the heat in bulk Si (dashed lines) and bulk PbTe (solid lines). The 300 K values for L_{10}, L_{50}, and L_{90} in Si were previously depicted in Fig. 3-11(d).

have to integrate out to 12.8 μm (that is, L_{90}=12.8 μm). This is about 40 - 60 times larger than the traditional estimates.

Thus, over two orders of magnitude of mean free paths are important for carrying the heat in bulk Si at 300 K (~87 nm to ~12,800 nm). At lower temperatures the distribution has a similar breadth, while shifting to larger values (Fig. 3-12). Although the large value of L_{90} is surprising compared to the traditional estimates, it is consistent with observations in neutron-irradiated thin films [24] and microporous thin films [50] that an important fraction of the heat is carried by phonons with bulk mean free paths of the order of microns. Thus there is greater potential for thermal conductivity reduction by boundary scattering than might traditionally be thought from L_{Tradl}.

The thermal conductivity of good bulk thermoelectric materials such as PbTe is already much smaller than in bulk Si (2.0 W/mK compared to 150 W/mK at 300 K), and so it may seem that there is no practical potential for further thermal conductivity reduction by nanostructuring. However, the thermal conductivity is proportional to the group velocity which is also significantly lower in PbTe than in Si, and as mentioned previously it is the bulk mean free paths which determine the potential for thermal conductivity reduction in nanostructures. Figure 3-13 shows the thermal conductivity for PbTe bulk and nanostructures of several different sizes. It is clear that there is still ample potential for reducing the thermal conductivity through nanostructuring, especially at lower temperatures and for nanowire diameters of ~56 nm or less. Although Fig. 3-12 shows that the important bulk mean free paths are about an order of magnitude shorter in PbTe than in Si, over a wide range of temperatures, they are still long enough to be significantly impacted by nanostructures. For example, in bulk PbTe at 300 K the median

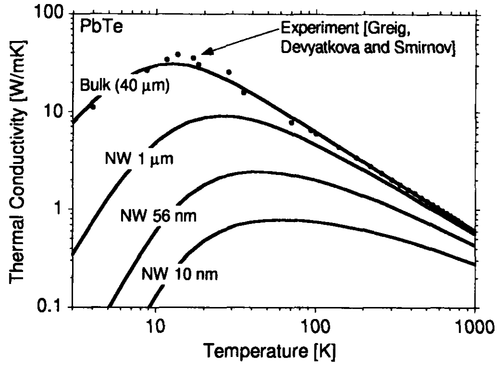

Figure 3-13. Theoretical and experimental thermal conductivity of PbTe bulk and nanowires, showing that boundary scattering can reduce the already low bulk conductivity even further [1].

mean free path (L_{50}) is about 42 nm, and the central 80% of the heat is carried by mean free paths between 6 nm (L_{10}) and 860 nm (L_{90}). These mean free path values are much larger than the naive estimate of only 3 nm (L_{Naive}) at 300 K.

3.5 The importance of various wavelengths

Similar to the transformation of Eq. (3-28), we can express the thermal conductivity integral in terms of the contributions of various wavelengths:

$$k = \int_0^\infty k_\omega \, d\omega \quad \Rightarrow \quad k = \int_0^\infty k_\lambda \, d\lambda \tag{3-33}$$

where the thermal conductivity per unit wavelength is

$$k_\lambda = -\tfrac{1}{3}\hbar\omega \frac{q^2}{2\pi^2} \frac{\partial f}{\partial T} L \frac{d\omega}{d\lambda} \tag{3-34}$$

These distributions have been analyzed for both Debye and Born-von Karman dispersion relations, assuming that the mean free path is dominated by boundary scattering [1]. Cutoff wavelengths are defined analogously to Eq. (3-32):

$$\alpha \equiv \frac{\int_0^{\lambda_\alpha(T)} k_\lambda(T)\, d\lambda}{\int_0^\infty k_\lambda(T)\, d\lambda} = \frac{\int_0^{\lambda_\alpha(T)} k_\lambda(T)\, d\lambda}{k(T)} \tag{3-35}$$

For example, 10% of the heat is carried by phonons with wavelengths shorter than λ_{10}. The resulting cutoff wavelengths for Si and PbTe are shown in Fig. 3-14. At low temperatures the cutoff wavelengths

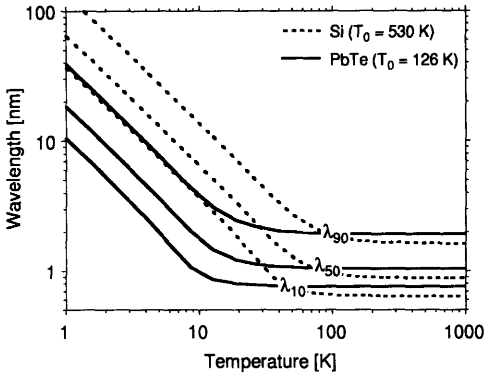

Figure 3-14. The range of wavelengths that are important for carrying the heat in Si and PbTe nanostructures, using the Born-von Karman phonon dispersion and neglecting the frequency dependence of mean free paths [1].

are proportional to $1/T$, in accordance with the phonon analog of Wien's displacement law [Eq. (3-2)]. At higher temperatures the cutoff wavelengths become constant and range from about 0.5 to 2 nm. Thus, at typical temperatures of interest for most thermoelectric applications (100 K and up), classical rather than quantum effects can be expected for nanostructures larger than ~5-10 nm, as we discussed in the beginning of this chapter.

3.6 Summary

This portion of the thesis focused on modeling of thermal conductivity in nanostructures when the phonons can be approximated as classical particles. This approximation is appropriate in most realistic nanostructures above ~100 K because the phonon wavelengths (~1-2 nm) are small compared to the nanostructure size and also small or comparable to the nanostructure roughness. Kinetic theory was combined with Matthiessen's rule to model alloy/impurity scattering, phonon-phonon umklapp scattering, and scattering off of boundaries and interfaces. It is important to account for the frequency dependence of various properties or the full extent of thermal conductivity reduction in nanostructures will not be appreciated. The Born-von Karman dispersion was found to be significantly better than the Debye dispersion at modeling real experimental phonon dispersion relations. The resulting model gives good agreement with literature measurements of the thermal conductivity of silicon nanowires as small as 56 nm diameter, with no adjustable parameters, and good agreement for Si/SiGe superlattice nanowires of similar size with one adjustable parameter. Finally, by introducing a change of variables it was possible to present distribution functions indicating the relative importance of a broad range of mean free paths. In bulk materials the distribution of important mean free paths (10% to 90% of the total thermal conductivity) spans more than two orders of magnitude, indicating that long mean free paths play a more important role than is commonly realized.

3.7 References

1. C. Dames and G. Chen, "Thermal conductivity of nanostructured thermoelectric materials," in *Thermoelectrics Handbook: Macro to Nano*, ed. D. Rowe, CRC Press (2005).
2. C. Dames, M. S. Dresselhaus, and G. Chen, "Phonon Thermal Conductivity of Superlattice Nanowires for Thermoelectric Applications," in *Thermoelectric Materials 2003. Research and Applications, Proc. of Mater. Res. Soc. Fall Meeting*, ed. G. S. Nolas *et al.* (2004).
3. C. Dames and G. Chen, *J. Appl. Phys.*, **95**, 682 (2004).
4. B. Yang and G. Chen, *Phys. Rev. B*, **67**, 195311 (2003).
5. M. V. Simkin and G. D. Mahan, *Phys. Rev. Lett.*, **84**, 927 (2000).
6. Ping Sheng, *Introduction to wave scattering, localization, and mesoscopic phenomena* (Academic Press, 1995).
7. J. Jackle, *Solid State Commun.* **39**, 1261 (1981).
8. M. J. Kelly, *J. Phys. C, Solid State Phys.* **15,** L969 (1982).
9. J. Seyler and M. N. Wybourne, *J. Phys., Condens. Matter.* **2**, 8853 (1990).
10. J. M. Ziman, *Electrons and Phonons* (Oxford University Press, 1960).
11. R. Berman, F. E. Simon, and J. M. Ziman, *Proc. R. Soc. Lond. A, Math. Phys. Sci.* **220**, 171 (1953).
12. R. Berman, E. L. Foster, and J. M. Ziman, *Proc. R. Soc. Lond. A, Math. Phys. Sci.* **231**, 130 (1955).
13. M. S. Gudiksen, L. J. Lauhon, J. Wang, D. C. Smith, and C. M. Lieber, *Nature* (London) **415**, 617 (2002).
14. L. J. Lauhon, M. S. Gudiksen, D. Wang, and C. M. Lieber, *Nature* (London) **420**, 57 (2002).
15. M. T. Bjork *et al.*, *Nano Lett.* **2**, 87 (2002).
16. Y. Wu, R. Fan, and P. Yang, *Nano Lett.* **2**, 83 (2002).
17. D. Bimberg, F. Heinrichsdorff, R. K. Bauer, D. Gerthsen, D. Stenkamp, D. E. Mars, and J. N. Miller, *J. Vac. Sci. Tech. B*, **10**, 1793, (1992).
18. T. S. Tighe, J. M. Worlock, and M. L. Roukes, *Appl. Phys. Lett.* **70**, 2687 (1997)..
19. W. Fon, W. C. Schwab, J. M. Worlock, and M. L. Roukes, *Phys. Rev. B* **66**, 045302 (2002).
20. C. Kittel, *Introduction to Solid State Physics*, 7th Edition (Wiley, 1996).
21. N. W. Ashcroft & N. D. Mermin, *Solid State Physics* (Harcourt, 1976).
22. B. Yang and G. Chen, "Phonon heat conduction in superlattices," in *Chemistry, Physics, and Materials Science of Thermoelectric Materials: Beyond Bismuth Telluride*, ed. M.G. Kanatzidis, *et al.*, Kluwer Academic/Plenum Publishers (2003).

23. M. G. Holland, *Phys. Rev.* **132**, 2461 (1963).

24. N. Savvides and H. J. Goldsmid, *J. Phys. C: Solid State Phys.* **6**, 1701 (1973).

25. B. Abeles, *Phys. Rev.* **131,** 1906 (1963).

26. Y.-J. Han, *Phys. Rev. B.* **54**, 8977 (1996).

27. A. S. Henry and Gang Chen, submitted (2006).

28. T. C. Harman, J. Taylor, M. P. Walsh, and B. E. LaForge, *Science* **297**, 2229.

29. R. Venkatasubramanian, E. Siivola, T. Colpitts, and B. O'Quinn, *Nature* (London) **413**, 597 (2001).

30. Kuei Fang Hsu, Sim Loo, Fu Guo, Wei Chen, J.S. Dyck, C. Uher, T. Hogan, E. K. Polychroniadis, and M. G. Kanatzidis, *Science* **303**, 818 (2004).

31. K. E. Goodson and Y. S. Ju, *Annu. Rev. Mater. Sci.* **29**, 261 (1999).

32. G. Chen, *Semicond. Semimetals* **71**, 203 (2001).

33. G. Chen, *Nanoscale Energy Transfer and Conversion* (Oxford University Press, 2005).

34. G. A. Slack, "The thermal conductivity of nonmetallic crystals," in *Solid State Physics* **34**, ed. by F. Seitz and D. Turnbull, Academic Press (1979).

35. D. G. Cahill, S. K. Watson, and R. O. Pohl, *Phys. Rev. B*, **46**, 6131 (1992).

36. R. M. Costescu, D. G. Cahill, F. H. Fabreguette, Z. A. Sechrist, and S. M. George, *Science* **303**, 989 (2004).

37. E. T. Swartz and R. O. Pohl, "Thermal boundary resistance," *Rev. Mod. Phys.* **61**, 605 (1989).

38. R. Venkatasubramanian, *Phys. Rev. B* **61**, 3091 (2000).

39. I. Yamasaki, R. Yamanaka, M. Mikami, H. Sonobe, Y. Mori, and T. Sasaki, *Proc. 17th Int. Conf. on Thermoelectrics, ICT'98*, pg. 210 (1998).

40. W. S. Capinski, H. J. Maris, T. Ruf, M. Cardona, K. Ploog, and D. S. Katzer, *Phys. Rev. B*, **59**, 8105 (1999).

41. L. D. Hicks and M. S. Dresselhaus, *Phys. Rev. B*, **47**, 16631 (1993).

42. Yu-Ming Lin, Xiangzhong Sun, and M. S. Dresselhaus, *Phys. Rev. B* **62**, 4610 (2000).

43. H. B. G. Casimir, *Physica* **5**, 495 (1938).

44. D. Li, Y. Wu, P. Kim, L. Shi, P. Yang, and A. Majumdar, *Appl. Phys. Lett.* **83**, 2934 (2003).

45. D. Li, Y. Wu, R. Fan, P. Yang, and A. Majumdar, *Appl. Phys. Lett.* **83,** 3186 (2003).

46. E. D. Devyatkova and I. A. Smirnov, *Sov. Phys. — Solid State* **3**, 1675 (1962).

47. Purdue University. Thermophysical Properties Research Center, *Thermophysical Properties of Matter*, Y. S. Touloukian, ed., (IFI/Plenum, New York, 1970-1979).

48. D. Greig, *Phys. Rev.* **120**, 358 (1960).

49. C. J. Glassbrenner and G. A. Slack, *Phys. Rev.* **134,** A1059 (1964).

50. D. Song and G. Chen, *Appl. Phys. Lett.* **84**, 687 (2004).

51. B. P. Pandey and B. Dayal, *J. Phys. C: Solid State Phys.* **6**, 2943 (1973).

52. G. Dolling, *Inelastic scattering of neutrons in solids and liquids* (Vienna: IAEA), vol. II, pg. 37 (1963).

Chapter 4: 1ω, 2ω, and 3ω methods for measurements of thermal properties

4.1. Introduction

3ω methods have proven to be valuable for measuring the thermal properties of various systems. In the basic method, a line heater is driven by a sinusoidal current source at angular frequency ω, causing a temperature fluctuation at 2ω related to the thermal properties of the heater and/or its surrounding environment [4, 7, 8]. This perturbs the heater resistance at 2ω, leading to a voltage signal at 3ω. By varying the configuration of heater and surroundings, 3ω methods have been used to measure the specific heat c [1, 2] and thermal conductivity k of a suspended wire [3], k of solids [4] and thin films [5, 6], and k and c of liquids [7, 8]. To achieve a good signal to noise ratio, the much larger Ohmic signal at 1ω is typically canceled either by nulling a bridge [1,2,8] or by subtraction with a multiplying digital-to-analog converter [4], although when using a lock-in amplifier with sufficient dynamic reserve it is simpler to omit this cancellation step [3]. Another issue in implementing 3ω methods is that some lock-in amplifiers do not have 3rd harmonic detection built-in, requiring an external frequency-tripler [2, 4, 8].

A different class of experiments involves Joule heating of a serpentine on a platform using a large DC current, and measuring the resulting temperature rise using lock-in detection of a small AC current superposed through the same heater. As reported by Shi *et al.* [9], the proportionality between temperature and voltage can vary by a factor of three depending on the period of the AC sensing current compared to the thermal time constant of the system.

In this chapter the various traditional 3ω methods as well as the DC-heating/AC-detection experiments are united under a more general framework of thermal and electrical transfer functions. This framework can be applied to any thermal system containing a line heater that is also used to sense temperature. A related transfer function approach is used in hot-wire anemometry, with a focus on DC currents only [10]. Here, voltages at 1ω and 2ω are shown to contain the same information about thermal properties as the 3ω voltage does. The 2ω signal requires a DC offset at the driving current source. The 1ω signal eliminates the need for higher-harmonic detection and may also be useful for systems with very fast thermal response, such as nanowires. The 1ω, 2ω, and 3ω methods are verified experimentally using both a line heater on a Pyrex substrate, and a suspended platinum wire, without any common-mode subtraction.

The usual 3ω analysis assumes that the circuit is driven with an ideal current source, but it is more common and convenient to use a voltage source instead. The important distinctions between current and voltage sources have not been adequately discussed in the literature. Here we also derive and verify a correction factor that permits the usual current-source analysis to be adapted to experiments performed with a voltage source. This correction factor is important whenever the electrical resistance of the sample is a significant fraction of the total resistance of the circuit.

This chapter is based very closely on recent work by Dames and Chen [14], but includes more explanations about the concept of thermal transfer functions. Some of the techniques developed in this chapter are also important for the single-nanowire measurements described in Chapter 5.

4.2. General transfer function framework

4.2.1. Thermal transfer functions

We are interested in systems containing a single heater that is also used to sense temperature through changes in its electrical resistance. Such systems may be described quite generally by a linear thermal transfer function, Z, relating the average temperature rise of the heater, θ_{avg}, to the heat input, Q. In the frequency domain,

$$\theta_\omega(\omega) = Q_\omega(\omega) Z(\omega) \tag{4-1}$$

where the ω subscript denotes Fourier-transformed quantities. In the time domain,

$$\theta_{\text{avg}}(t) = Q(t) \otimes Z_t(t) \tag{4-2}$$

where ⊗ denotes convolution and Z_t is the inverse Fourier transform of Z. For example, sinusoidal heating at frequency ω_H

$$Q(t) = Q_0 \sin(\omega_H t) \tag{4-3}$$

leads to a temperature response in the time domain

$$\theta_{\text{avg}}(t) = Q_0 \,\text{Re}(Z) \sin(\omega_H t) + Q_0 \,\text{Im}(Z) \cos(\omega_H t)\,. \tag{4-4}$$

The thermal transfer function may be complex and frequency dependent. It contains information about the thermal properties of the system, such as thermal conductivity and/or specific heat of the heater and/or its surroundings.

In general the full frequency-dependent, complex transfer function of Eq. (4-1) can be determined from basic heat transfer analysis. For readers unfamiliar with convolution, Z can also be defined through Eqs. (4-3) and (4-4), and understood as a generalization of the familiar concept of thermal resistance. For example, for a system where heat capacity effects can be neglected, the system can be modeled in the quasi-static limit. Stated another way, when we can neglect the thermal mass, the temperature response is always in-phase with the heating. In this case Z is purely real, and is simply the thermal resistance measured between the temperature of the surroundings and the average temperature of the heater. Another elementary example is an isolated, adiabatic mass of heat capacity C (units of J/K). In this case energy conservation requires that $Q(t) = C(\partial\theta/\partial t)$. Analysis of Eqs. (4-3) and (4-4) then shows that $Z=1/j\omega C$ for this system, with $j = \sqrt{-1}$. Two more examples of Z for more complicated systems are given below in Eqs. (4-24) and (4-33).

4.2.2. Electrical transfer functions

By measuring the electrical current I and voltage V across the heater, we can determine the thermal properties of the system. First the thermal transfer function must be related to an electrical transfer function.

The traditional 3ω approaches are summarized in Figure 4-1(a). A sinusoidal current at frequency ω leads to Joule heating with a 2ω component. The magnitude and phase of the resulting temperature rise at 2ω depends on Z. Due to the temperature coefficient of resistivity α, the electrical resistance of the heater also contains a modulation at 2ω. Finally, the current at ω mixes with the resistance at 2ω leading to a voltage signal at 3ω. Here we derive the analogous results for the more general case of a sinusoidal current with a DC offset. As shown in Fig. 4-1(b), we will see that the DC offset leads to Joule heating at 1ω and a voltage at 2ω.

In general, the electrical resistance of the heater is given by

$$R_e(t) = R_{e0}\left(1 + \alpha\theta_{avg}(t)\right) \tag{4-5}$$

where R_{e0} is the electrical resistance in the limit of zero current and θ_{avg} is averaged over the length of the heater. The temperature fluctuations within the heater must be small enough so that α may be treated as a constant. It is easily shown that Eq. (4-5) holds even if the temperature profile $\theta(x)$ varies along the length of the heater, as long as the cross-section is uniform. Because $\alpha\theta_{avg} << 1$, to leading order Q can be approximated as

$$Q(t) = I^2(t)R_{e0}\,. \tag{4-6}$$

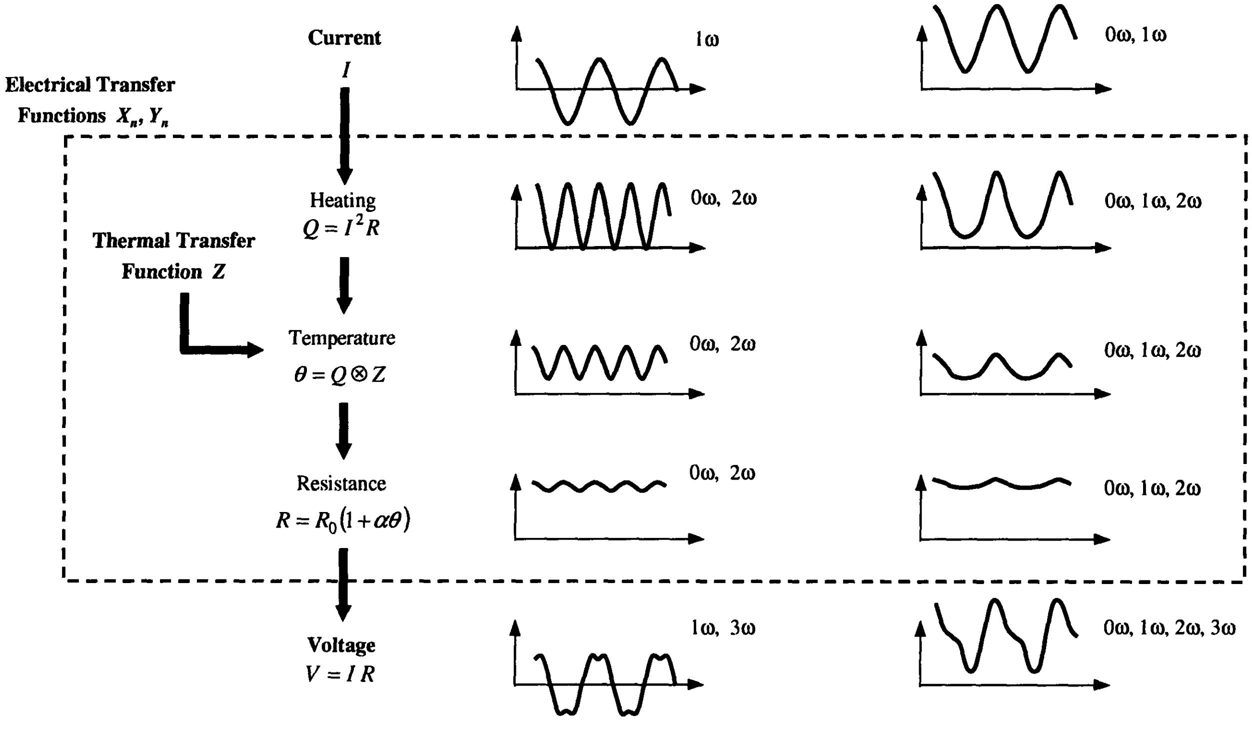

(a) Traditional 3ω **(b) Add DC offset to Current**

Figure 4-1. Schematic relationship between current, voltage, and thermal transfer functions for 1ω, 2ω, and 3ω methods. (a) Traditional 3ω methods. (b) Addition of a DC offset to the driving current, resulting in additional terms for 1ω heating and 2ω voltage.

Combining Eqs. (4-5) and (4-6), the voltage drop across the heater is

$$V(t) = I(t)R_{e0}\left(1 + \alpha R_{e0} Z \otimes I^2(t)\right), \tag{4-7}$$

Finally, using the frequency convolution theorem of Fourier transforms, the voltage in the frequency domain is given by

$$V_\omega = (R_{e0}/2\pi)I_\omega \otimes \left[2\pi\delta(\omega) + \alpha(R_{e0}/2\pi)(I_\omega \otimes I_\omega)Z\right] \tag{4-8}$$

where δ is the Dirac delta function.

Equation (8) applies to any current. Because it is nonlinear in I, we cannot use superposition, and instead focus on the particular case of heating by a sinusoidal current at frequency ω_1 with a DC offset:

$$I(t) = I_{DC} + I_1 \sin(\omega_1 t) \tag{4-9}$$

where it is convenient to define

$$\eta = I_{DC} / I_1 . \tag{4-10}$$

In the frequency domain,

$$I_\omega = I_1\left(\eta 2\pi\delta(\omega) + j\pi\left[\delta(\omega+\omega_1) - \delta(\omega-\omega_1)\right]\right), \tag{4-11}$$

where $j = \sqrt{-1}$.

Applying this current to the analysis described above, the voltage response occurs at DC and three harmonics

$$V(t) = V_{DC} + V_{1\omega}(t) + V_{2\omega}(t) + V_{3\omega}(t) \tag{4-12}$$

which can be expressed as

$$V(t) = \alpha R_{e0}^2 I_1^3 \sum_{n=0}^{3}\left[X_n(\omega_1,\eta)\sin(n\omega_1 t) + Y_n(\omega_1,\eta)\cos(n\omega_1 t)\right] \tag{4-13}$$

where the summation is over the harmonics n. Here X_n and Y_n are the in-phase and out-of-phase electrical transfer functions. In terms of RMS quantities as usually measured by lock-in amplifiers,

$$\frac{V_{n\omega,rms}}{2\alpha R_{e0}^2 I_{1,rms}^3} = X_n(\omega_1,\eta) + jY_n(\omega_1,\eta) \tag{4-14}$$

The resulting X_n and Y_n are given in Table 4-1. This is the most important result of the paper. It shows that the various electrical harmonics are rich with information about any thermal transfer function. For example, at 3ω the in-phase (X_3) and out-of-phase (Y_3) voltages are proportional to the real and imaginary parts of the thermal transfer function, respectively. Because they are a response to the Joule heating at twice the driving current, Z is probed at $2\omega_1$.

The 2ω voltages X_2 and Y_2 are only present in the case of a DC offset ($\eta \neq 0$). The in-phase 2ω voltage is sensitive to the imaginary part of Z, while the out-of-phase 2ω voltage is sensitive to the real part of Z. Furthermore, each 2ω voltage has contributions from the thermal response at both ω_1 and $2\omega_1$. This is because the Joule heating now has components at both $1\omega_1$ and $2\omega_1$, as seen in Fig. 4-1(b). The heating at $1\omega_1$ becomes a voltage at $2\omega_1$ after mixing with the $1\omega_1$ component of the current; and the heating at $2\omega_1$ becomes a voltage also at $2\omega_1$, after mixing with the DC component of the current.

The 1ω voltages X_1 and Y_1 are somewhat more complicated. Similar to Y_3, Y_1 has information about the imaginary part of $Z(2\omega_1)$, arising from the 2ω heating which is mixed back to 1ω by the 1ω component of the current. Whenever there is a DC offset in the current Y_1 has an additional contribution from $Z(\omega_1)$, due to the mixing of 1ω heating and DC current. The in-phase voltage X_1 has analogous

Harmonic, n	In-phase electrical transfer function, $X_n(\omega_1,\eta)$	Out-of-phase electrical transfer function, $Y_n(\omega_1,\eta)$
0	0	$\eta\sqrt{2}\left[\frac{1}{2\alpha R_{e0} I_{1rms}^2} + (\eta^2 + (1/2))Z(0) + \mathrm{Re}(Z(\omega_1))\right]$
1	$\frac{1}{2\alpha R_{e0} I_{1,rms}^2} + (\eta^2 + (1/2))Z(0) +$ $2\eta^2 \mathrm{Re}(Z(\omega_1)) + (1/4)\mathrm{Re}(Z(2\omega_1))$	$(1/4)\mathrm{Im}(Z(2\omega_1)) + 2\eta^2 \mathrm{Im}(Z(\omega_1))$
2	$\eta(1/2)[\mathrm{Im}(Z(2\omega_1)) + 2\,\mathrm{Im}(Z(\omega_1))]$	$-\eta(1/2)[\mathrm{Re}(Z(2\omega_1)) + 2\,\mathrm{Re}(Z(\omega_1))]$
3	$-(1/4)\mathrm{Re}(Z(2\omega_1))$	$-(1/4)\mathrm{Im}(Z(2\omega_1))$

Table 4-1. 0ω, 1ω, 2ω, and 3ω electrical transfer functions defined by Eq. (4-14), for a thermal transfer function Z driven by current $I=I_1[\eta+\sin(\omega_1 t)]$. This very general result applies to any system with a line heater that is also used to measure temperature.

contributions from both of these effects (the final two terms of X_1 in Table 4-1), plus two other terms. The first term of X_1 is simply the large Ohmic response $V=I_1R_{e0}$, after normalizing according to Eq. (4-14). The second term of X_1, multiplying $Z(0)$, is the response to DC heating. This arises from both DC current (the η^2 term), and, importantly, the DC component of $[I_1 \sin(\omega_1 t)]^2$.

The in-phase 1ω voltage is unique because it contains information about the DC thermal response even in the high frequency limit. Because of thermal capacitance effects, most thermal transfer functions should become small at high frequencies. Thus X_2, X_3, Y_1, Y_2, and Y_3 should die out at high frequency. But X_1 retains a term multiplying Z(0), allowing the DC thermal response to be measured at high frequency. This is because there is always a DC component in the I^2R heating of Eq. (4-9), even at high frequencies. For example, with $I_{DC}=0$ ($\eta=0$), the high-frequency limit of X_1 has an Ohmic voltage plus $Z(0)/2$, while in the low-frequency limit the contribution is $3Z(0)/4$. The opposite limit is $I_{DC}>>I_1$ ($\eta>>1$). In this case the high-frequency limit of X_1 is dominated by the contribution of $\eta^2 Z(0)$, while the dominant contribution at low frequency is $3\eta^2 Z(0)$. This shows that the factor of three difference between low- and high-frequency resistances reported by Shi *et al.* [9] ($\eta\approx 10$) is a general result, further indicating the broad applicability of the current transfer function framework.

Finally, in the presence of a DC offset in the current there is also a DC voltage across the sample. This is labeled as out-of-phase in Table 4-1 because of the convention introduced in Eq. (4-13). The three terms of Y_0 comprise: a large Ohmic voltage; a contribution from the same DC heating as the second term of X_1; and the mixing of 1ω heating and 1ω current back to DC. These DC signals are not expected to be useful because they are subject to low-frequency drifts and thermoelectric voltages.

4.2.3. Current source vs. voltage source

The derivation above follows the usual assumption of an ideal current source at 1ω. In practice it is often easier to use a voltage source, such as a function generator or the reference signal of a lock-in amplifier. Although an op-amp circuit may be used to convert this voltage source to a current source,[3] it is more common to use the voltage source directly while analyzing the data as if a current source had been used. Here we show that this simplification is valid only if the sample resistance is small compared to the total resistance of the circuit, and give a correction factor to use when the sample resistance is larger. Holland and Smith have also briefly considered the case of a voltage source for the special case of a suspended wire [11].

Referring to Figure 4-2(a), the total electrical resistance of the circuit R_{Total} consists of the time-varying sample resistance, $R_e(t)$, plus all other "ballast" resistances, R_b, which are assumed constant over time. The ballast resistance includes the leads, the output impedance of the voltage source, and any additional resistors. For this voltage divider it is always true that

$$\frac{V(t)}{V_s(t)} = \frac{R_e(t)}{R_b + R_e(t)} \tag{4-15}$$

where $V_s(t)$ is the time-varying voltage source.

In the usual way, we neglect the small resistance perturbations when calculating the Joule heating,:

$$Q(t) \approx \frac{V^2(t)}{R_{e0}} = \frac{V_s^2(t)}{R_{e0}}\left(\frac{R_{e0}}{R_b + R_{e0}}\right)^2 \tag{4-16}$$

Eqs. (4-2) and (4-5) still hold, so

$$R_e(t) = R_{e0}\left(1 + \alpha Z \otimes Q(t)\right) \tag{4-17}$$

The current through the circuit is then

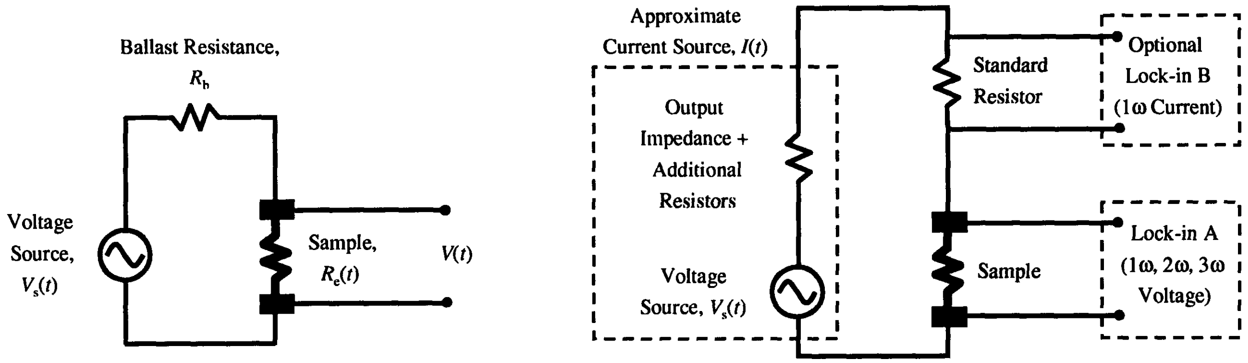

(a)

(b)

Figure 4-2. (a) Circuit for analyzing the effects of using a voltage source rather than a current source which is usually assumed. (b) Schematic of equipment for simple 1ω, 2ω, and 3ω experiments. No steps were taken to remove the large 1ω common-mode voltage. A voltage source was used to approximate a current source. Lock-in B was used to infer current from the voltage across a standard resistor. If Lock-in B is omitted, the current can be estimated from the ratio of source voltage to total circuit resistance.

$$I(t)=\frac{V_s(t)}{R_b+R_e(t)}\approx\frac{V_s(t)}{R_b+R_{e0}}\left(1-\left(\frac{R_{e0}}{R_b+R_{e0}}\right)\alpha Z\otimes Q(t)\right) \tag{4-18}$$

where the negative sign arises from the leading order Taylor-series expansion of $(1+\alpha Z\otimes Q)^{-1}$. This shows that, if R_{e0} is a small fraction of (R_b+R_{e0}), the true current is approximated well by the usually-assumed $V_s/(R_b+R_{e0})$, but that an adjustment must be made otherwise. Comparing Eq. (4-18) with Eq. (4-7) further suggests that in the case of a voltage source at 1ω, it would be more appropriate to measure the harmonics of *current* to determine the thermal transfer function. Results analogous to Table 4-1 could be derived to give the electrical transfer function for a current in response to a voltage input of

$$V_s(t)=V_{s,DC}+V_{s,1}\sin(\omega_1 t) \tag{4-19}$$

However, it is perhaps more useful to summarize this analysis by providing a correction factor to the results previously derived for a current source. To see this combine Eqs. (4-15) and (4-17), again using leading order expansions, yielding

$$V(t)\approx V_s(t)\left(\frac{R_{e0}}{R_{e0}+R_b}\right)\left[1+\left(\frac{R_b}{R_{e0}+R_b}\right)\alpha Q(t)\otimes Z\right] \tag{4-20}$$

Finally, recognizing that the usual analysis assumes the current to be given by

$$I(t) \approx V_s(t)/(R_b + R_{e0}) \tag{4-21}$$

then the voltage across the sample can be expressed as

$$V(t) = I(t)R_{e0}\left[1 + \alpha R_{e0} I^2(t) \otimes Z_t\left(1 - \frac{R_{e0}}{R_{e0} + R_b}\right)\right]. \tag{4-22}$$

This is identical to Eq. (4-7), except for the factor of $1-R_{e0}/(R_{e0}+R_b)$ multiplying Z_t. Thus, even when using a voltage source, it is still possible to use the current-source analysis of Table 4-1 for data processing as long as the resulting calculated Z_{Apparent} is corrected using

$$Z_{True} = Z_{Apparent}\left(1 - \frac{R_{Sample}}{R_{Total}}\right)^{-1} \tag{4-23}$$

The R_{Sample} term should include all current-carrying resistances that exhibit 3ω harmonics, even if they lie outside the voltage probes, and thus may actually be larger than R_{e0}. This important point is clarified in Section 4.3. The relative importance of the correction factor is seen to be the same as the relative contribution of the sample resistance to the total resistance of the circuit. This correction factor applies to any 3ω system using a voltage source for experiment but assuming a current source for data processing.

4.3. Experiment

To demonstrate the validity and generality of the analysis summarized in Table 4-1 and Eq. (4-23), these 1ω, 2ω, and 3ω methods were applied to two traditional 3ω systems: an isolated suspended wire (SW), and a line heater on a substrate (LHOS). In the former system the goal is to measure both *k* and *c* of the heater itself, while in the latter system the goal is to measure *k* of the substrate.

The experimental apparatus is summarized in Fig. 4-2(b). The various voltage harmonics across the sample were measured using Lock-in A (Stanford Research Systems SR850). A sinusoidal voltage source at 1ω was used to approximate a current source. The 1ω current was determined by measuring the 1ω voltage across a heat-sunk 10 Ω precision resistor (Vishay Dale, $\alpha \sim 10^{-5}$ K^{-1}) using Lock-in B (SR830), which was also useful for precise phase corrections of the 1ω signals. The correction of Eq. (4-23) was applied whenever the sample resistance was more than a few percent of the total circuit resistance. When DC offsets were required the voltage source was a function generator (HP 33120a); otherwise the sine wave output of Lock-in A was preferred to minimize phase errors.

Samples were mounted in a vacuum chamber and the temperature controlled to 300 K (Lakeshore 330). Radiation losses were minimized by shielding, convection losses by operating in vacuum of typically $\sim 10^{-5}$ torr, and conduction losses by using small diameter alloy wires for electrical connections.

For the suspended wire experiment the sample was a 50.8 μm (2 mil) diameter, 28.7 mm long platinum wire (99.99% purity, R_{e0}~1.5 Ω) soldered in a four-point configuration directly to the prongs of the sample holder. For the line heater on substrate experiment, the sample was Pyrex, about 3 mm thick, with a microfabricated metal heater about 33 μm wide. The voltage drop was measured across the central 1000 μm (R_{e0}~54 Ω) of the 3000 μm long heater. For both systems the temperature coefficient of resistivity was determined by measuring the resistance at several temperatures between 300 K and about 320 K.

Similar to Lu, Yi, and Zhang's approach for suspended wires [3] but counter to common practice for 3ω measurements, we have not used any noise cancellation scheme, such as nulling a bridge [1, 2, 8], or subtraction of the voltage across a series resistor using a multiplying digital-to-analog converter [4]. This omission is successful only because of the high resolution and large dynamic reserve of Lock-in A. With the optimal settings of maximum gain and minimum dynamic reserve, we routinely observe stable voltage steps of approximately 0.06 parts-per-thousand (ppt) of the full-scale sensitivity, corresponding to 1 part in 2^{14}. This is far better than the specified 1% absolute accuracy of the instrument, and highlights an important detail when studying the 1ω signals: to avoid absolute errors between the various gain settings, we always keep the gain constant when sweeping frequency and/or amplitude at any one temperature point.

Other experimental details include DC coupling the input and turning off all line filters, to keep from distorting these signals over the typical frequency range of 0.01 Hz to 100 Hz. We assumed that the phase reported by Lock-in B for the current represented the true value, and so some of the measurements were affected by phase disagreements between Lock-ins A and B of ~0.1 degree. We have confirmed that the phase accuracy could be improved to ~0.02 degree in the future, by zeroing the phase of each lock-in at each frequency while driving a small-amplitude 1ω current. This is especially important for 1ω measurements and when using an external function generator. Finally, it is possible to omit Lock-in B, and instead measure the current simply by the ratio of the source voltage to the total resistance of the circuit. This gives sufficient accuracy for most purposes, but requires knowledge of the circuit resistance at each temperature of measurement, and may lead to unacceptable phase errors in the out-of-phase 1ω signal.

4.4. Results

The suspended wire and line-heater-on-substrate systems are discussed separately. For each, the theoretical thermal and electrical transfer functions are first derived. Then, data are presented to validate the expected dependencies on AC and DC currents. Finally, the measured electrical transfer functions are presented, and the corresponding thermophysical properties of platinum (*k* and *c*) and Pyrex (*k*) are extracted according to 1ω, 2ω, and 3ω methods independently. The correction factor of Eq. (4-23) is also verified below.

4.4.1. Suspended wire (SW)

Theoretical transfer functions

The thermal transfer function for an isolated, suspended wire (SW) with thermally clamped ends was given by Lu, Yi, and Zhang as a series solution [3]. A closed-form solution for the spatial temperature profile is derived in Appendix A. The resulting thermal transfer function for a wire of length $2l$ and cross-sectional area S is

$$Z_{SW}(\omega_H) = \frac{[\sinh(\beta) - \sin(\beta)] + j[\sinh(\beta) + \sin(\beta) - \beta(\cosh(\beta) + \cos(\beta))]}{\beta C \omega_H [\cos(\beta) + \cosh(\beta)]} \tag{4-24}$$

where C is the thermal capacitance of the wire,

$$\beta = \sqrt{\omega_H \tau / 2}\,, \tag{4-25}$$

the characteristic diffusion time is

$$\tau = 4l^2 / \kappa\,, \tag{4-26}$$

and κ is the thermal diffusivity.

This transfer function is depicted by the solid lines in Fig. 4-3. The shape is reminiscent of a lumped first order (RC) system, so we are motivated to determine the lumped transfer function $Z_{SW,Lump}$ that is the best approximation to Z_{SW}. As derived in Appendix B, the appropriate transfer function is

$$Z_{SW,Lump}(\omega_H) = \frac{R_{th}}{12}\left(\frac{1 - j\omega_H \tau / 10}{1 + (\omega_H \tau / 10)^2}\right), \tag{4-27}$$

where

$$R_{th} = 2l / kS\,. \tag{4-28}$$

As shown by the dots in Fig. 4-3, $Z_{SW,Lump}$ is an excellent approximation to Z_{SW} over most frequencies.

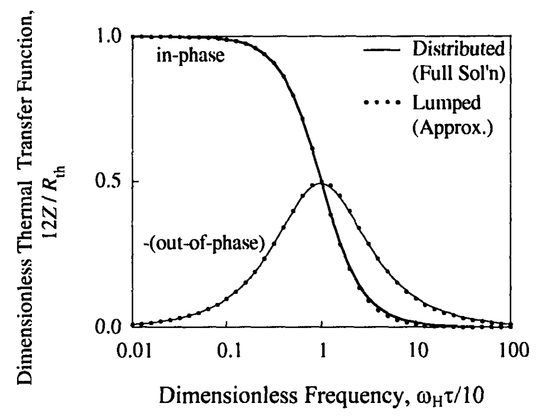

Figure 4-3. Thermal transfer functions (average temperature rise per unit heat input) as a function of heating frequency, for an isolated, suspended wire with thermally clamped ends. The transfer function is nondimensionalized using the thermal resistance $R_{th}=2l/kS$, and the frequency using the thermal diffusion time $\tau=4l^2/\kappa$. The solid lines are the exact solution, and the dots are a lumped approximation.

Harmonic, n	Dimensionless in-phase electrical transfer function, $\tilde{X}_{n,SW,Lump}(\tilde{\omega}_1,\eta)$	Dimensionless out-of-phase electrical transfer function, $\tilde{Y}_{n,SW,Lump}(\tilde{\omega}_1,\eta)$
0	0	$\eta\sqrt{2}\left[\frac{6}{\alpha R_{th}R_{e0}I_{1,rms}^2}+\left(\eta^2+1/2\right)+\frac{1}{1+\tilde{\omega}_1^2}\right]$
1	$\frac{6}{\alpha R_{th}R_{e0}I_{1,rms}^2}+\left(\eta^2+1/2\right)+\frac{(1/4)}{1+4\tilde{\omega}_1^2}+\eta^2\frac{2}{1+\tilde{\omega}_1^2}$	$-\frac{(1/2)\tilde{\omega}_1}{1+4\tilde{\omega}_1^2}-\eta^2\frac{2\tilde{\omega}_1}{1+\tilde{\omega}_1^2}$
2	$-(\eta/2)\left[\frac{2\tilde{\omega}_1}{1+4\tilde{\omega}_1^2}+\frac{2\tilde{\omega}_1}{1+\tilde{\omega}_1^2}\right]$	$-(\eta/2)\left[\frac{1}{1+4\tilde{\omega}_1^2}+\frac{2}{1+\tilde{\omega}_1^2}\right]$
3	$(-1/4)\frac{1}{1+4\tilde{\omega}_1^2}$	$(1/4)\frac{2\tilde{\omega}_1}{1+4\tilde{\omega}_1^2}$

Table 4-2. Dimensionless 0ω, 1ω, 2ω, and 3ω electrical transfer functions defined by Eq. (4-14), for the special case of a suspended wire in the lumped approximation [Eq. (4-31)].

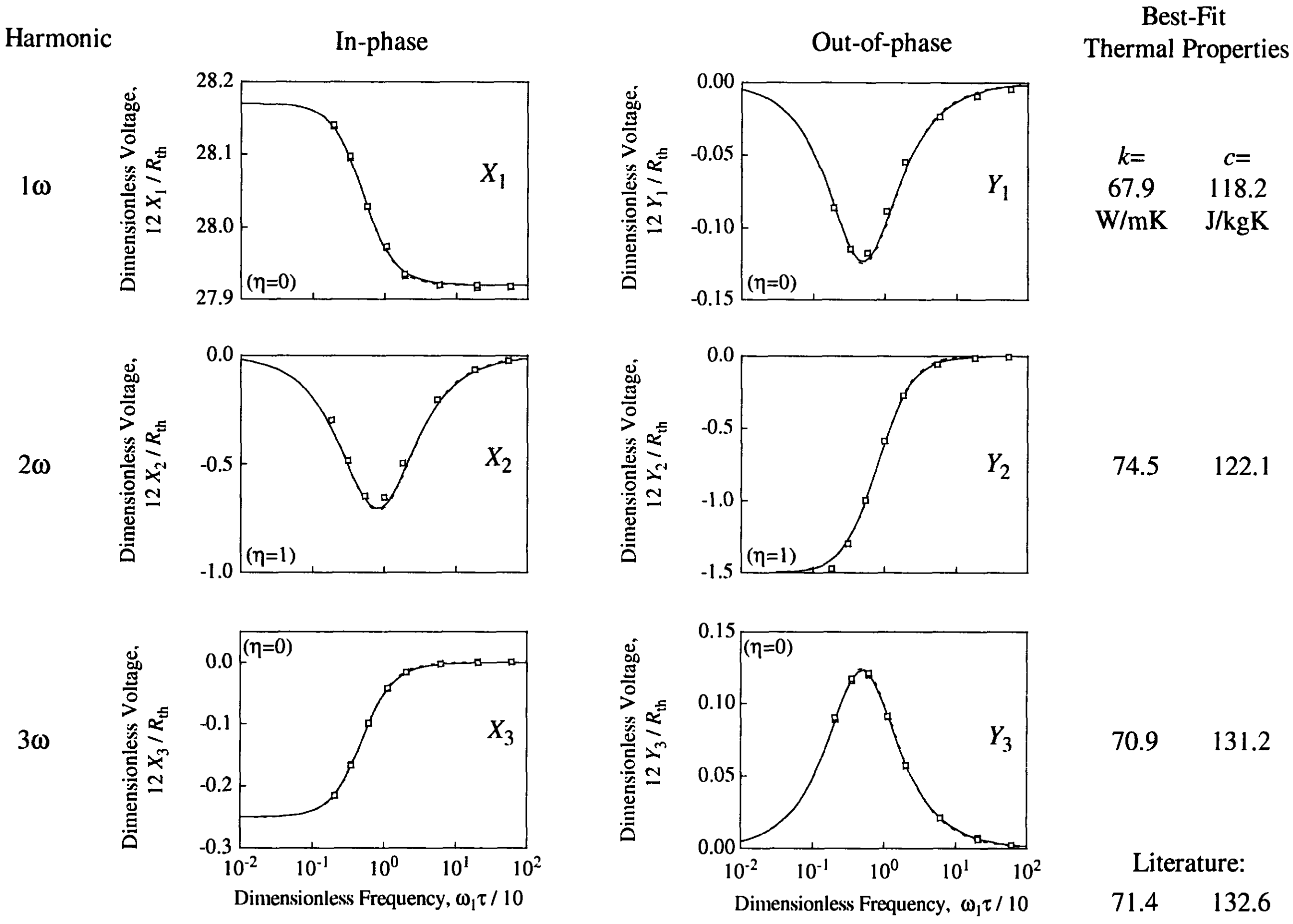

Figure 4-4. 1ω, 2ω, and 3ω electrical transfer functions (voltage divided by the cube of the current) for a suspended wire. The solid lines are the exact solution, the dashed lines are a lumped approximation, and the points are experimental data for a platinum wire at 300 K. The lumped approximation is almost indistinguishable from the exact solution. The values of thermal conductivity and specific heat used to fit the data from each harmonic are given on the right, and compared with literature values [12].

It is convenient to nondimensionalize Z_{SW}, X_n, and Y_n using $R_{th}/12$:

$$\tilde{Z}_{SW} = 12 Z_{SW} / R_{th}, \tag{4-29a}$$

$$\tilde{X}_n = 12 X_n / R_{th}, \tag{4-29b}$$

$$\tilde{Y}_n = 12 Y_n / R_{th}. \tag{4-29c}$$

Similarly, define

$$\tilde{\omega}_H = \omega_H \tau / 10. \tag{4-30}$$

Then Eq. (4-27) becomes

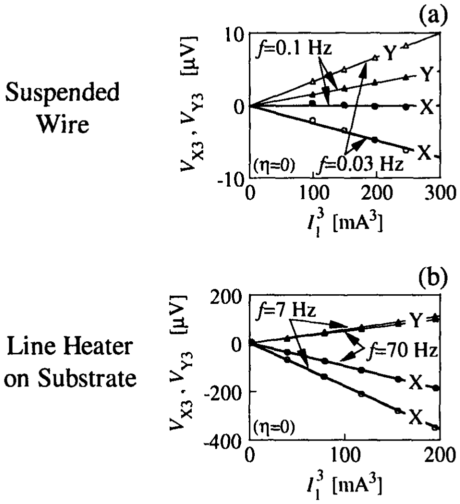

Figure 4-5. 3ω voltage vs. 1ω current, at constant frequency, showing the expected I^3 trend. (a) Suspended platinum wire at 300 K. (b) Line heater on a Pyrex substrate at 300 K.

$$\tilde{Z}_{SW,lump}(\tilde{\omega}_H) = \frac{1 - j\tilde{\omega}_H}{1 + \tilde{\omega}_H^2} \tag{4-31}$$

The electrical transfer functions obtained by substituting Eq. (4-24) into Table 4-1 are easily evaluated but cumbersome to write out. On the other hand, Eq. (4-31) is so simple that it is worthwhile to give the electrical transfer functions explicitly for the lumped approximation (Table 4-2). As shown in Fig. 4-4, the exact (solid lines) and lumped (dashed lines) electrical transfer functions are essentially identical at low frequencies, and still agree very closely even at high frequencies. Although the data analysis in the present work uses the exact solution, the lumped solution is simpler to use and should be adequate for most purposes.

Current dependencies

The various electrical transfer functions of Table 4-1 show different scalings with I_1 and I_{DC} (through η). The scalings are compared with SW experiments in Fig. 4-5(a) for 3ω, Fig. 4-6(a-b) for 2ω, and Fig. 4-7(a-d) for 1ω. Fig 5 confirms that at constant frequency, both in-phase (V_{X3}) and out-of-phase voltages (V_{Y3}) at 3ω are proportional to I_1^3. Similarly, Fig 4-6(a-b) confirms that the 2ω voltages scale with I_1^3 and are linearly proportional to η.

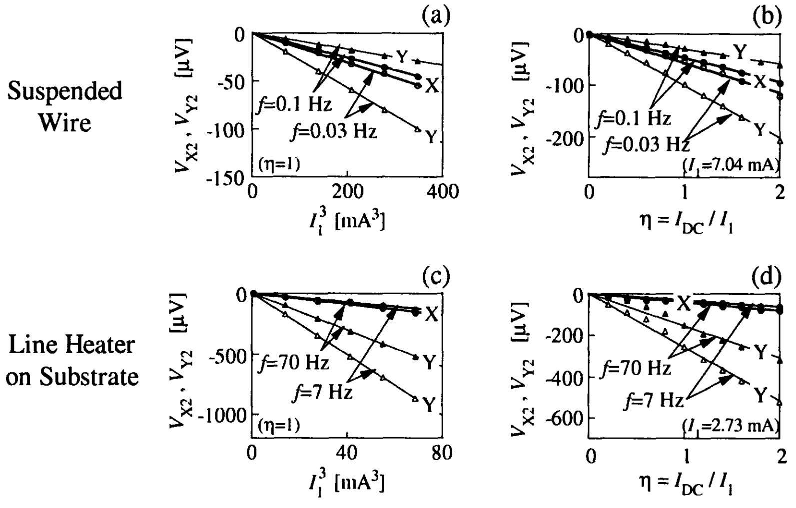

Figure 4-6. (a,c) 2ω voltage vs. 1ω current, at constant frequency and constant current ratio $\eta = I_{DC}/I_1$, showing the expected I^3 trend. (b,d) 2ω voltage vs. current ratio η, at constant frequency and constant AC current I_1, showing the expected linear trend. (a,b) are for a suspended platinum wire at 300 K, while (c,d) are for a line heater on a Pyrex substrate at 300 K.

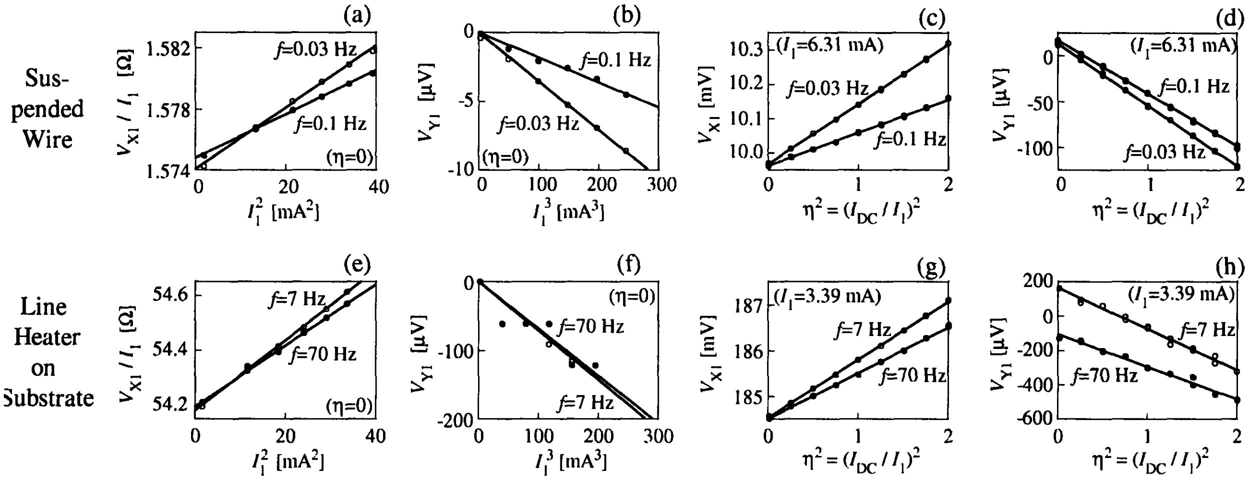

Figure 4-7. (a,e) In-phase 1ω voltage vs. 1ω current, at constant frequency, showing the expected trend of $a_1 I + a_2 I^3$. (b,f) Out-of-phase 1ω voltage vs. 1ω current, at constant frequency, showing the expected I^3 trend. (c,g) In-phase 1ω voltage vs. current ratio $\eta = I_{DC}/I_1$, at constant frequency and constant AC current I_1, showing the expected trend of $a_3 + a_4\eta^2$. (d,h) Out-of-phase 1ω voltage vs. current ratio η, at constant frequency and constant AC current I_1, showing the expected trend of $a_5 + a_6\eta^2$. (a-d) are for a suspended platinum wire at 300 K, while (e-g) are for a line heater on a Pyrex substrate at 300 K.

Figure 4-7(a-d) also shows the expected scaling with I_1^3 and η^2. Figure 4-7(a) in particular shows that the small change in V_{X1} due to Joule heating can be distinguished from the much larger Ohmic signal, without any common-mode subtraction. The intercepts at I_1=0 of the two curves of Fig. 4-7(a) should in principle be identical, and the slight disagreement of approximately 1 ppt is an indication of the uncertainties in phase and amplitude at the two different frequencies. The fact that the η=0 intercepts of Fig. 4-7(d) are positive rather than negative as predicted by Table 4-2 is due to the phase error between Lock-in A and the function generator. The phase uncertainty between Lock-in A and Lock-in B was typically ~0.1 degree, corresponding to a coupling of about 2 ppt from V_{X1} into V_{Y1}. Figure 4-7(c) shows that V_{X1} was typically 10 mV, corresponding to an uncertainty of ~20 μV coupled into V_{Y1}. This value is consistent with the offset in Fig. 4-7(d). Particularly for the 1ω methods, this shows that it is not the absolute values of X_n and Y_n, but rather their slopes with respect to I_1 and/or I_{DC}, that are most reliable for determining the thermal transfer functions.

Measured transfer functions

Having confirmed the expected dependencies on I_1 and I_{DC} at constant frequency, the electrical transfer functions at 1ω, 2ω, and 3ω were then measured at constant current while sweeping frequency. The results are compared to the theoretical transfer functions in Fig. 4-4. The lowest frequency measured was 0.01 Hz. Because of the long thermal diffusion time ($\tau \approx 30$ s), it was inconvenient to measure data at lower $\omega\tau$ because of the long settling times involved.

For each harmonic, a least squares fit was used to determine the R_{th} and τ that give the best match between measured and theoretical transfer functions. The fit was applied to both in-phase and out-of-phase transfer functions of a given harmonic simultaneously, although either could also be fit separately. The thermal conductivity is calculated directly from R_{th} using Eq. (4-28). The specific heat is calculated from

$$c = \frac{\tau}{mR_{th}} \tag{4-32}$$

where m is the mass of the sample based on measured geometry and the literature value of density. Because c involves two different experimentally measured parameters its uncertainty is larger than the uncertainty in k.

The resulting values of k and c are included in Fig. 4-4 and compared with literature values [12]. The values calculated from the 3ω method are within about 1% of the literature values for both k and c. The errors in values calculated from 1ω and 2ω methods are somewhat worse, about 5% for k and 10% for c. This is consistent with the fact that there is slightly more scatter of the measured points about the

Harmonic, n	In-phase electrical transfer function, $X_{n,LHOS}(\omega_1,\eta)$	Out-of-phase electrical transfer function, $Y_{n,LHOS}(\omega_1,\eta)$
0	0	$\eta\sqrt{2}\left[\frac{1}{2\alpha R_{e0} I_{1rms}^2}+\left(\eta^2+(1/2)\right)Z(0)-\frac{\ln\omega_1+const}{2\pi k_{Subs}L}\right]$
1	$\frac{1}{2\alpha R_{e0} I_{1,rms}^2}+\left(\eta^2+(1/2)\right)Z(0)$ $-\left(8\eta^2+1\right)\frac{\ln\omega_1+const}{8\pi k_{Subs}L}-\frac{\ln 2}{8\pi k_{Subs}L}$	$\left(-1/16k_{Subs}L\right)\left(1+8\eta^2\right)$
2	$-3\eta/8k_{Subs}L$	$\left(\eta/4\pi\, k_{Subs}L\right)\left[3\ln\omega_1+\ln 2+3\,const\right]$
3	$(1/8\pi\, k_{Subs}L)\left(\ln\omega_1+\ln 2+const\right)$	$1/16k_{Subs}L$

Table 4-3. 0ω, 1ω, 2ω, and 3ω electrical transfer functions defined by Eq. (4-14), for the special case of a line heater on a substrate. The unknown constant *const* is the same for all terms.

theoretical curves of Fig. 4-(4) for 1ω and 2ω. The increased uncertainty at 1ω may be due to the greater demands it places on the stability of both amplitude and phase of the voltage source (in this case Lock-in A). The increased uncertainty at 2ω may be due to the necessity of using the external function generator as the voltage source.

4.4.2. Line heater on substrate (LHOS)

Theoretical transfer functions

The most widely known 3ω method is that popularized by Cahill [4] and Birge and Nagel [7, 8] to measure the thermal conductivity of a substrate adjacent to a line heater. For the case of a heater of length L on a semi-infinite substrate of thermal conductivity k_{Subs}, the thermal transfer function is given by [4]

$$Z_{LHOS}(\omega_H)=\left(-1/2\pi k_{Subs}L\right)\left[\ln\omega_H+j\pi/2+const\right] \tag{4-33}$$

where the unknown constant *const* is purely real, and the frequency must be such that the thermal wavelength $\lambda=(\kappa_{Subs}/\omega_H)^{1/2}$ is large compared to the heater width yet small compared to the substrate dimensions. This transfer function is depicted in Fig. 4-8. When $\omega_H=0$ Eq. (4-33) diverges, but $Z_{LHOS}(0)$ is actually limited to some finite value due to the finite substrate size. Table 4-3 gives the specific electrical transfer functions obtained by substituting Eq. (4-33) into Table 4-1. They are depicted

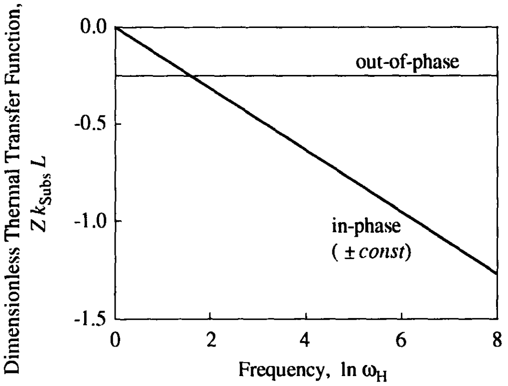

Figure 4-8. Thermal transfer functions (average temperature rise per unit heat input) as a function of heating frequency, for a line heater on a substrate. The transfer function is nondimensionalized using the product of the substrate's thermal conductivity k_{Subs} and the heater length L. An arbitrary constant has been subtracted from the in-phase transfer function.

graphically by the solid lines of Fig. 4-9. For each harmonic, one of the (X_n, Y_n) signals is expected to vary linearly with ln(ω_1), while the other signal is expected to be a constant.

Current dependencies

The scalings of the LHOS voltages with current at two different frequencies are shown in Fig 5(b) for 3ω, Fig. 4-6(c-d) for 2ω, and Fig. 4-7(e-h) for 1ω. Fig 5(b) shows that the 3ω voltages are proportional to I_1^3 as expected. Fig. 4-6(c) shows that the 2ω voltages also scale with I_1^3 as expected. However, the scatter of the experimental points about the expected linear η dependence shown in Fig. 4-6(d) is larger than expected.

Figure 4-7(e) also shows the expected scaling with I_1^3, with the two resistance estimates (the intercepts at $I_1 = 0$) agreeing to better than 1 ppt. The out-of-phase voltages in Fig. 4-7(f) show large scatter in discrete steps because they are at the limit of the sensitivity of the instrument. To detect the in-phase voltages [Fig 7(e)] of ~300 mV the full scale sensitivity was set to 500 mV. The 0.06 ppt voltage steps mentioned early are then 30 μV, consistent with the limiting resolution apparent in Fig 7(f). The variation with DC current in Fig. 4-7(g-h) shows the expected η^2 scaling for both in-phase and out-of-phase voltages. According to Table 4-3, the two curves of Fig. 4-7(h) should be identical. The errors are due to the residual ~0.1 degree phase uncertainty between the function generator and Lock-in A after using Lock-in B for phase correction. This coupling of about 2 ppt of V_{X1} into V_{Y1} corresponds to about

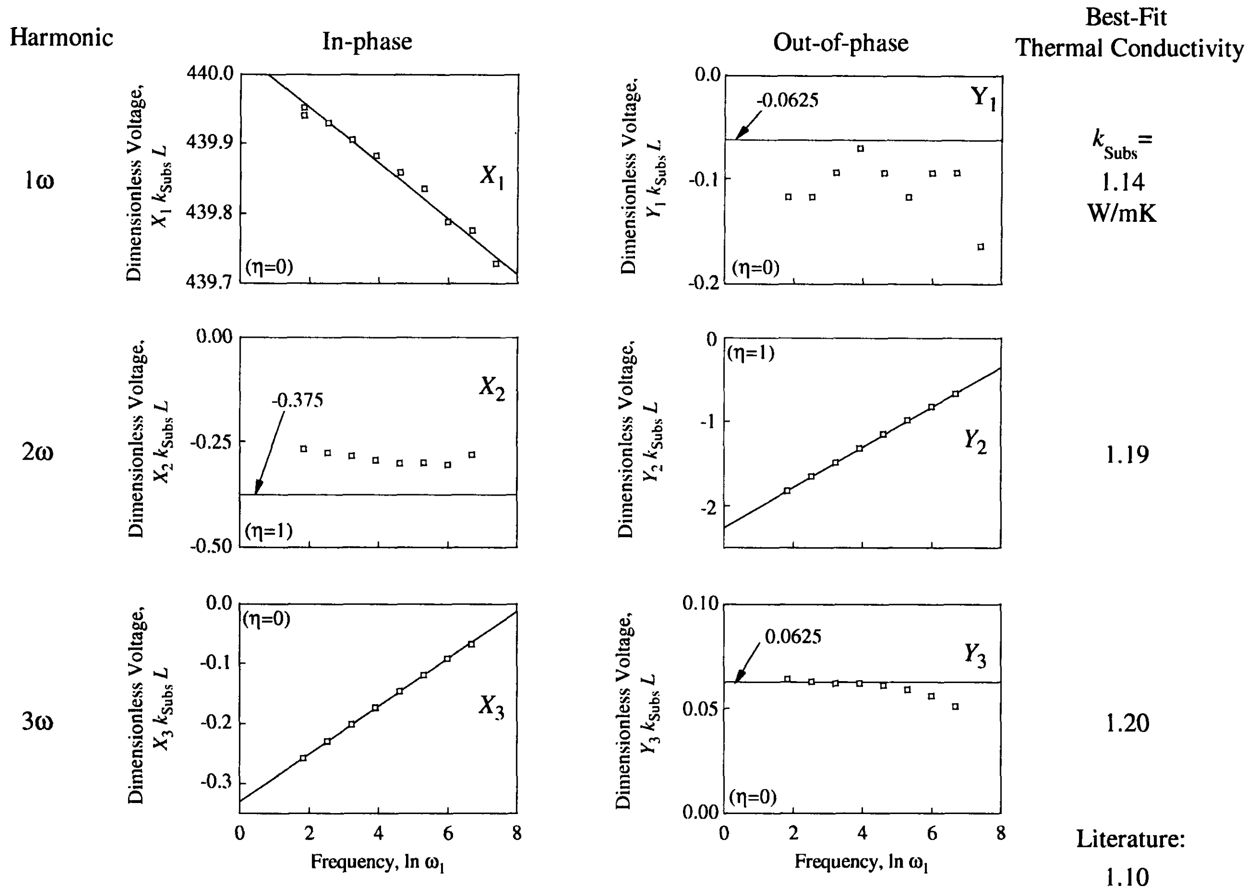

Figure 4-9. 1ω, 2ω, and 3ω electrical transfer functions (voltage divided by the cube of the current) for a line heater on a substrate. The solid lines are the exact solution, and the points are experimental data for a Pyrex substrate at 300 K. The values of thermal conductivity used to fit the data from each harmonic are given on the right and compared to literature values [12].

400 μV of uncertainty in the intercept at $\eta = 0$ in Fig. 4-7(h). Again, for the 1ω signals in particular, the slopes with respect to η^2 and/or I_1^3 are more reliable than the intercepts for determining thermal properties.

Measured transfer functions

Figure 4-9 compares the measured and theoretical electrical transfer functions at 1ω, 2ω, and 3ω. For each harmonic the thermal conductivity was found by fitting the slope of the appropriate signal (X_1, Y_2, and X_3) with respect to ln(ω_1). This is a generalization of the "slope method" commonly used in traditional 3ω analysis [6]. The other signal (Y_1, X_2, and Y_3) was not used in the fitting, and the measurements show large deviations from the theoretical value at 2ω (-0.375) and especially at 1ω (-

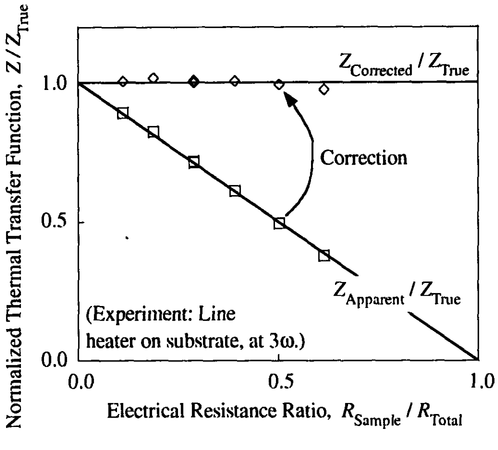

Figure 4-10. Apparent and corrected thermal transfer functions (average temperature rise per unit heat input), according to Eq. (4-23). The sample resistance R_{Sample} includes the full length of the line heater, which may be longer than the portion spanned by the voltage probes. This correction applies to any 1ω, 2ω, or 3ω experiment that uses a voltage source but assumes a current source for analysis and data processing.

0.0625). As with the suspended-wire system, these deviations may be due to the phase disagreements between function generator and Lock-in A at 2ω, and the extreme sensitivity of Y_1 to phase errors. For the traditional 3ω method, Cahill also reported that the slope method gives more accurate results than using the magnitude of the constant out-of-phase voltage [4]. The resulting values of thermal conductivity agree with each other to within 5%, and are about 5-10% higher than a literature value of 1.10 W/mK [12]. Again, the 1ω data shows the largest scatter compared to the theoretical curve, because of the large offset voltage which is not canceled. The root-mean-square deviation of the measurements in Fig. 4-9(a) from the theoretical curve is only about 0.02 ppt rms. However this is enough to contribute significantly to the uncertainty because the total range of the data only spans ~0.5 ppt (439.73 to 439.95).

4.4.3. Current source vs. voltage Source

Figure 4-10 shows an example of measured thermal transfer functions both with and without the correction of Eq. (4-23) for using a voltage source instead of an ideal current source. These data were taken by varying the additional resistors [Fig 2(b)] in the line-heater-on-substrate experiment described above. Although only 3ω data are used in this example, the correction should be the same for any harmonic and any type of thermal transfer function that can be described using Table 4-1. For each measurement, the total resistance was determined along with the apparent thermal transfer function $Z_{Apparent}$, calculated assuming an ideal current source according to Table 4-3. Using the measured resistance ratio the thermal transfer function was corrected to $Z_{Corrected}$ using Eq. (4-23). Finally, the average of these $Z_{\text{Corrected}}$ was taken as the true thermal transfer function Z_{True}. When making this correction it is essential to correctly account for the other portions of the electrical circuit which are subject to the same thermal transfer function as the test section. In this line-heater-on-substrate example, the voltage taps of the four-point probe at the sample only span the central 1000 μm of a 3000 μm long heater line. However, the remaining 2000 μm of the heater still respond thermally in a similar way (neglecting end effects), so we may think of the effective sample as being 3000 μm long, with triple the resistance as measured by the four-point probe. In effect, those extra 2000 μm of current-carrying leads should not be counted as stable ballast resistance, but instead exhibit 3ω behavior like the sample resistance. Therefore, in this example, when making the correction of Eq. (4-23), $R_{\text{Sample}} = 3\ R_{e0}$. This can also be understood by considering the sample itself to be the 3000 μm long line, and simply multiplying the four-point probe voltages by a factor of 3. In the case of a suspended wire, however, this adjustment for leads should not be necessary, because any extra leads are likely to be heat sunk and/or have much lower resistance than the test section.

The raw and corrected Z of Fig. 4-10 are clearly in good agreement with the analysis of Eq. (4-23). The correction factor is unimportant when the sample resistance is negligible compared to the total resistance of the circuit. On the other hand, when the sample resistance is a significant fraction of the total resistance, the correction becomes large. The latter situation is undesirable because it is more sensitive to experimental uncertainties in measuring R_b and in measuring the unnecessarily small values of $X_{n,Apparent}$, and $Y_{n,Apparent}$. If a voltage source must be used with $R_{\text{Sample}} >> R_b$, it would be better to either measure the current harmonics directly as suggested in Eq. (4-18), or use an op-amp to implement a true current source [3]. In practice R_b is likely to be at least 50 Ω due to the output impedance of most voltage sources, suggesting that the correction of Eq. (4-23) may be an important consideration whenever R_{e0} is more than a few Ohms, unless additional ballast resistance is used.

Finally, we note that even with the widespread practice of common-mode subtraction it is still necessary to consider the correction for using a voltage source instead of a current source. This is evident from Eq. (4-22). To implement common-mode subtraction a "series resistor" is introduced into the circuit [4]. This R_{series} is chosen to have nearly the same resistance as R_{e0}, but with good heat sinking and/or a small temperature coefficient so that its resistance is constant and its voltage drop is always simply $I(t)R_{\text{series}}$. Lock-in A is then used to measure the difference in voltage drops across the sample and the series resistor. This has the effect of canceling the first term in Eq. (4-22), but it does not affect the $(1-R_{e0}/(R_{e0}+R_b))$ term multiplying Z. Therefore the correction of Eq. (4-23) is still necessary.

To Maximize:	Filter DC at lock-in?	At this harmonic 1ω, in-phase	 1ω, out-of-phase	 2ω	 3ω
Signal	No filter	$\eta=0$	$\eta=1+\sqrt{5/8}\approx1.79$	$\eta=1/2$	$\eta=0$
Signal	Filter DC	$\eta=0$	$\eta=1+\sqrt{5/8}\approx1.79$	$\eta=1/2$	$\eta=0$
Signal-to-background	No filter	$\eta=0$	$\eta=1+\sqrt{5/8}\approx1.79$	$\eta=1/2$	$\eta=0$
Signal-to-background	Filter DC	$\eta=\infty$	$\eta=\infty$	$\eta=1$	$\eta=0$

Table 4-4. Optimal values of the current ratio $\eta=I_{DC}/I_1$ for best signal, or signal-to-background, for various harmonics. In some cases the optimum η depends on whether the DC portion of the voltage is filtered at the lock-in amplifier. The temperature rise is assumed to be constrained to $\theta_{avg}<\theta_{max}$, which is equivalent to constraining the total current $I_1+I_{DC}<I_{max}$. The experiment is further assumed to include low frequencies.

4.5. Discussion and Recommendations

4.5.1. Selection of optimal DC current

As shown in Table 4-1, the voltage signals at 1ω and 2ω increase with increasing DC current (increasing η). However, this also increases the common-mode voltage, and the temperature variations within the sample, both of which may be undesirable. Calculations for the optimum values of η for several different constraints are discussed below and summarized in Table 4-4. However, these optimization calculations still have to be confirmed experimentally. Future work should also consider the effects of operating with η away from the calculated optimum value, and determine an allowable range of η for reasonable uncertainty.

Maximum signal for a limited temperature rise

The maximum temperature fluctuations of the sample, θ_{max}, should generally be limited to a few Kelvins in order to avoid ambiguity about the temperature of the measurement. This limits the currents as well. To simplify the analysis we assume that the experiment will include low frequencies, so that $Z(\omega)$ and $Z(2\omega)$ can be approximated with $Z(0)$. This should be the maximum value of Z. In this case the largest temperature rise is given by

$$\theta_{avg}(t)=\left[I_{DC}+I_1\sin(\omega_1 t)\right]^2 R_{e0}Z(0) \tag{4-34}$$

leading to the constraint

$$I_1+I_{DC}\le I_{max} \tag{4-35}$$

where $I_{\max} = \sqrt{\theta_{\max} / R_{e0} Z(0)}$.

From Table 4-1 and Eq. (4-14), the 3ω signals are not enhanced by I_{DC}, and so should always operate with $\eta=0$. The 2ω voltages, on the other hand, are proportional to $I_1^2 I_{DC}$. Subject to Eq. (4-35), the optimum currents are found to be $I_1=2I_{\max}/3$ and $I_{DC}=I_{\max}/3$, that is, $\eta=1/2$. With these optimizations, the 2ω and 3ω voltages have similar magnitudes for the two transfer functions considered in Tables 4-2 and 4-3.

The useful part of the 1ω signals has terms proportional to $I_1 I_{DC}^2$ as well as I_1^3. Optimization constrained by Eq. (4-35) now leads to $\eta=0$ to maximize the in-phase signal (V_{1X}), and $\eta = 1+\sqrt{5/8} = 1.791$ to maximize the out-of-phase signal (V_{1Y}). DC currents are more important in the optimized V_{1Y} compared to the optimized V_{1X}, because the η^2 terms are relatively more important in Y_1 than in X_1.

Maximum signal-to-background for a limited temperature rise

Instead of maximizing the signal voltage itself, we may wish to maximize the signal-to-background ratio. This makes the best use of the gain and dynamic reserve of the lock-in amplifier, which is especially important when common mode subtraction is omitted, as in the present work. If the voltages are not filtered at the lock-in, then the peak background voltage for all harmonics is $I_{\max}R_{e0}$, and optimization for maximum signal-to-background is equivalent to the optimization for maximum signal just discussed. However, if the DC component is filtered at the lock-in amplifier, then the background voltage contains only the Ohmic 1ω component I_1R_{e0}. In this case the 2ω signal-to-background is optimized at $\eta=1$, and is approximately 1.5 times larger than the optimized 3ω signal-to-background.

For the 1ω signal with DC filtering at the lock-in, the optimization leads to $\eta \to \infty$, i.e. a small AC sense current combined with a much larger DC heating current.

Other limitations

Sometimes the experiment will be constrained by the current or voltage limits of the equipment. For example, the current will be limited when a voltage source is used with large ballast resistances to approximate a current source. In other cases the background signal voltages may be so large as to saturate the input of the lock-in amplifier. These situations are equivalent to the $I_{\max}$ constraint already discussed. For a current-limited power supply, $I_{\max}$ is the equipment limitation, while for a voltage-limited power supply, $I_{\max}=V_{s,\max}/(R_{e0}+R_b)$. For a saturated lock-in, $I_{\max}=V_{\text{Lock-in},\max}/R_{e0}$.

	3ω (I_{DC}=0)	2ω ($I_{DC}\neq0$)	1ω (I_{DC}=0)	1ω with DC offset ($I_{DC}\neq0$)
Higher-harmonic detection	Requires 3rd	Requires 2nd	Not necessary	Not necessary
Current source	Use lock-in's own reference	Requires DC offset (extra hardware)	Use lock-in's own reference	Requires DC offset (extra hardware)
Stability of current source	Not important	Not important	Very important (subtracting 2 large numbers)	Very important (subtracting 2 large numbers)
Sensitivity to phase errors	Insensitive	Insensitive	Very sensitive	Very sensitive
Probes Z purely at one frequency, or combines several?	One frequency	Combines two	One frequency (plus DC)	Combines two (plus DC)
Frequency of voltage signal compared to heating	Higher (good for thermally slow systems)	Higher and same	Lower (good for thermally fast systems)	Lower and same
Precedents	Well-established [1-8]	New	New	η>>1 used previously [9]
Recommendation	Most straightforward method. Use when not limited by fast system frequencies or need for 3rd harmonic detection.	Niche application: use instead of 3ω when hardware has frequency doubler, but not frequency tripler, built-in.	Use for systems with very fast characteristic frequencies. Use to avoid implementing higher-harmonic detection. Be wary of phase errors.	Use for systems with very fast characteristic frequencies. Use to avoid implementing higher-harmonic detection. Be wary of phase errors.

Table 4-5. Recommendations and comparison of 1ω, 2ω, and 3ω methods for thermal properties measurements.

4.5.2 Relative merits of 1*ω*, 2*ω*, and 3*ω* methods

Some of the strengths and weaknesses of these 1ω, 2ω, and 3ω methods are outlined in Table 4-5. The table highlights some important differences in the need for higher-harmonic detection, DC offset, and stability of the current source. The various methods also have important distinctions when studying the frequency response of systems with very slow, or very fast, characteristic thermal times. For example, k and c of a single nanowire might be studied with the suspended wire technique. However, the longitudinal thermal diffusion time is on the order of microseconds, corresponding to frequencies on the order of 100s of kHz. To minimize electrical noise from inductive and capacitive coupling, it is desirable to conduct the experiment at as low a frequency as possible. Table 4-1 shows that a 1ω study with η =0 probes the thermal response at twice the electrical detection frequency, in contrast to a 3ω study which probes the thermal response at 2/3 of the detection frequency. That is, the thermal response at 100 kHz is detected electrically at 50 kHz using 1ω, but at 150 kHz using 3ω. This shows that 1ω may be advantageous for systems with very fast dynamics. The argument is reversed for thermally very slow systems, where 3ω may be preferred.

Overall, the basic 3ω method is still the best option for most experiments. The 2ω method may be preferred for certain lock-in amplifiers which have frequency doubling built-in but not frequency tripling. 1ω methods place greater demands on the stability of the current supply, but eliminate the need for higher-harmonic detection, and are an important option when studying the dynamics of thermally fast systems. If a direct measurement of the thermal transfer function is desired, without combining the thermal response at multiple frequencies, then 3ω or 1ω with $\eta=0$ should be used.

4.6. Summary

In this portion of the thesis, a new framework of thermal transfer functions was developed to describe any thermal system containing a line heater that is also used to sense temperature (Table 4-1). This includes the traditional 3ω systems of a suspended wire (Fig. 4-4) and a line heater on a substrate (Fig. 4-9), as well as experiments combining a large DC heating current with a small AC sense current [9]. The analysis naturally identifies 1ω, 2ω, and 3ω variations which each have their own benefits in certain situations (Table 4-5).

This chapter also demonstrated that this class of thermal experiments can be simplified considerably [3] compared to traditional implementations, which relied on noise cancellation via a bridge or multiplying digital-to-analog converter [Fig. 4-2(b)]. Thanks to the excellent accuracy and dynamic reserve of modern lock-in amplifiers, we saw that good experimental accuracy can now be obtained without any noise cancellation.

Finally, this chapter showed that the widespread practice of using a voltage source to approximate a current source can lead to large errors if the sample resistance is not negligibly small compared to the total circuit resistance. These potential errors have not been discussed previously. A correction factor was derived [Eq. (4-23)] and verified (Fig. 4-10), which allows the usual current-source analyses to be rigorously adapted to the more common situation of a voltage-source experiment.

4.7. Appendix A: Temperature profile in a suspended wire

When a thin isolated wire is driven at a frequency much faster than the longitudinal thermal diffusion time the resulting temperature rise is related to c [1, 2, 11]. Similarly, the DC temperature rise is related to k [13]. A series solution for all frequencies was recently given by Lu, Yi, and Zhang [3]. Here we derive a closed-form solution and give a lumped approximation.

The unsteady, one-dimensional heat conduction equation neglecting convection and radiation losses, for a wire of length $2l$, is

$$\rho c\frac{\partial\theta}{\partial t}=k\frac{\partial^2\theta}{\partial x^2}+\frac{Q(t)}{2Sl}. \tag{4-A1}$$

Here $\theta(x,t)$ is the temperature rise at a position x along the wire axis, and ρ is the density. The cross-sectional area of the wire is S, which must be constant but need not be circular. Assuming perfect thermal contact at $x=\pm l$, the boundary conditions are

$$\begin{aligned}\frac{\partial\theta(0,t)}{\partial x}&=0\\ \theta(l,t)&=0\end{aligned} \tag{4-A2}$$

Taking the Fourier transform with respect to time and defining

$$W(x,\omega)=\theta_\omega-\frac{Q_\omega}{j\omega C} \tag{4-A3}$$

the governing equation becomes

$$\frac{j\omega}{\kappa}W=\frac{\partial^2 W}{\partial x^2} \tag{4-A4}$$

with transformed boundary conditions

$$\begin{aligned}\frac{\partial W(0,\omega)}{\partial x}&=0\\ W(l,\omega)&=-\frac{Q_\omega}{j\omega C}\end{aligned} \tag{4-A5}$$

For heating given by Eq. (4-3), Eqs. (4-A3) through (4-A5) can be solved for θ. After considerable manipulation, the temperature profile in response to heating is found to be

$$\begin{aligned}\theta(x,t)=&\left(\frac{Q_0}{C\omega_H}\right)\left(\frac{-\sin(q_0(x+l))\sinh(q_0(x-l))-\sin(q_0(x-l))\sinh(q_0(x+l))}{\cos(2q_0l)+\cosh(2q_0l)}\right)\sin(\omega_H t)\\ &+\left(\frac{Q_0}{C\omega_H}\right)\left(\frac{\cos(q_0(x-l))\cosh(q_0(x+l))+\cos(q_0(x+l))\cosh(q_0(x-l))}{\cos(2q_0l)+\cosh(2q_0l)}-1\right)\cos(\omega_H t)\end{aligned} \tag{4-A6}$$

where the thermal wavevector q_0 is given by

$$q_0=\sqrt{\frac{\omega_H}{2\kappa}}. \tag{4-A7}$$

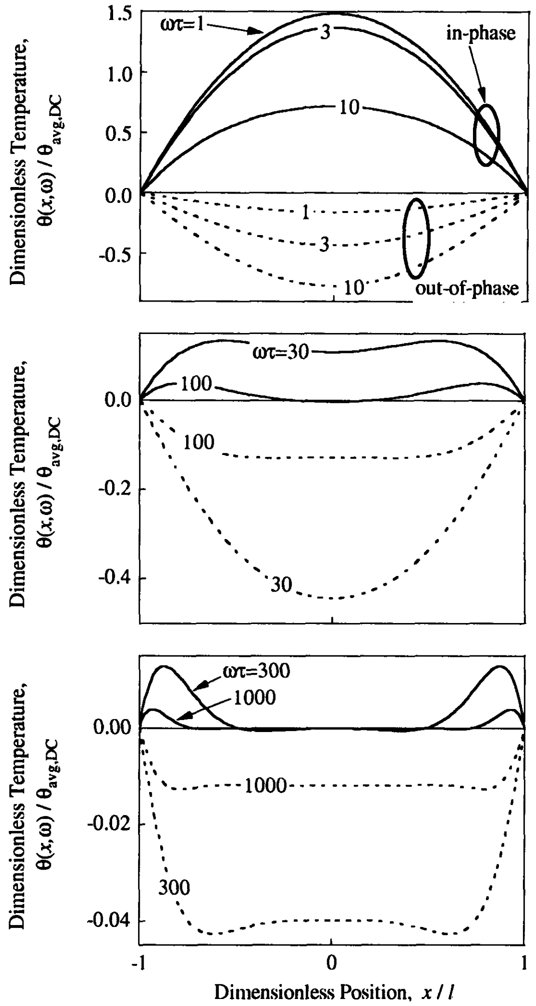

Figure 4-11. Temperature profiles for a suspended wire driven by sinusoidal heating at various frequencies. The solid lines are the in-phase temperature, and the dashed lines out-of-phase. The temperature rise is nondimensionalized by the average value at DC, and the frequency is nondimensionalized by the thermal diffusion time $\tau=4l^2/\kappa$. At low frequencies the response is large, parabolic, and in-phase, while at high frequencies the response is smaller, flatter, and out-of-phase.

Temperature profiles are depicted in Fig. 4-11 for various frequencies. At low frequencies the temperature response is a quasi-static parabola typical of a uniformly heated wire, in phase with the heating. At high frequencies the temperature profile is nearly flat and out-of-phase with the heating, because there is very little time for heat diffusion compared to the heating period. Interestingly, in the high frequency case the peak value of temperature occurs not at the center, but near the wire ends. This is also evident in the perturbation solution given by Holland and Smith for a semi-infinite wire [11]. It can be understood by considering the 90 degree phase difference between the heat source $Q(t)$ and conduction down the temperature gradient.

The spatially averaged temperature is given by:

$$\theta_{avg}(t) = \left(\frac{Q_0}{C\omega_H}\right)\left[\left(\frac{\sinh(\beta)-\sin(\beta)}{\beta(\cos(\beta)+\cosh(\beta))}\right)\sin(\omega_H t)\left(\frac{\sinh(\beta)+\sin(\beta)-\beta(\cosh(\beta)+\cos(\beta))}{\beta(\cos(\beta)+\cosh(\beta))}\right)\cos(\omega_H t)\right] \tag{4-A8}$$

where β is defined in Eq. (4-25). This leads directly to the transfer function given in Eq. (4-24).

4.8. Appendix B: Lumped approximation for suspended wire

Consider a lumped thermal mass with temperature $\theta_{Lump}(t)$ and total heat capacity C_{Lump} connected to $\theta_\infty=0$ by an external thermal resistance $R_{th,Lump}$. The well-known transfer function for this system is

$$Z_{SW,Lump}(\omega_H) = R_{th,Lump}\left(\frac{1-j\omega_H\tau_{Lump}}{1+(\omega_H\tau_{Lump})^2}\right) \tag{4-B1}$$

As shown in Fig. 4-3, $Z_{SW,Lump}$ is a remarkably good approximation to Z_{SW} over most frequencies as long as $R_{th,Lump}=R_{th}/12$, and $\tau_{Lump}=\tau/10$. These relations are justified mathematically by requiring $Z_{SW,Lump}$ and Z_{SW} to have the same asymptotic behavior at low frequencies, for both real and imaginary parts. These constraints are not unique. For example, if instead the correct magnitude of Z_{Lump} was desired at both low and high frequencies, the constraints would be $R_{th,Lump}=R_{th}/12$ and $\tau_{Lump}=\tau/12$ (that is, $C_{Lump}=C$).

An expression similar to Eq. (4-B1) was derived by Lu, Yi, and Zhang [3] by retaining only the first term of a series expansion. In particular, Eqs. (4-B1) and (4-14) lead to

$$\sqrt{V_{X3}^2+V_{Y3}^2} = \frac{\alpha R_{e0}^2 I_1^3 R_{th}}{24\sqrt{1+(2\omega\tau/10)^2}} \tag{4-B2}$$

which is slightly more accurate than Eq. (19) of Ref. [3]. That equation has $\pi^4/4$ in place of 24 in the denominator (too large by 1.47%) and π^2 in place of 10 inside the radical (too small by 1.30%).

4.9 References

1. L. A. Rosenthal, *Rev. Sci. Instrum.* **32**, 1033 (1961).
2. L. R. Holland, *J. Appl. Phys.* **34**, 2350 (1963).
3. L. Lu, W. Yi, and D. L. Zhang, *Rev. Sci. Instrum.* **72**, 2996 (2001).
4. D. G. Cahill, *Rev. Sci. Instrum.* **61**, 802 (1990).
5. D. G. Cahill, M. Katiyar, and J. R. Abelson, *Phys. Rev. B* **50**, 6077 (1994).

6. T. Borca-Tasciuc, A. R. Kumar, and G. Chen, *Rev. Sci. Instrum.* **72**, 2139 (2001).
7. N. O. Birge, *Phys. Rev. B* **34**, 1631 (1986).
8. N. O. Birge and S. R. Nagel, *Rev. Sci. Instrum.* **58**, 1464 (1987).
9. L. Shi, D. Li, C. Yu, W. Jang, D. Kim, Z. Yao, P. Kim, and A. Majumdar, *J. Heat Transf.* **125**, 881 (2003).
10. A. E. Perry, *Hot-wire anemometry* (Oxford Science Publications, Oxford, 1982).
11. L. R. Holland and R. C. Smith, *J. Appl. Phys.* **37**, 4528 (1966).
12. Purdue University. Thermophysical Properties Research Center, *Thermophysical Properties of Matter*, Y. S. Touloukian, ed., (IFI/Plenum, New York, 1970-1979).
13. Y. C. Tai, C. H. Mastrangelo, and R. S. Muller, *J. Appl. Phys.* **63**, 1442 (1988).
14. C. Dames and G. Chen, *Rev. Sci. Instrum.* **76**, 124902 (2005).

Chapter 5: Thermoelectric measurements of individual nanowires and nanotubes

5.1 Introduction

Previous chapters of this thesis have described some of the quantum (wave) and classical (particle) size effects that are expected to cause dramatic changes in the thermoelectric properties of nanowires (NWs) and nanotubes (NTs) compared to their bulk counterparts. It is essential to test these models experimentally, and the most compelling experiments are those on individual NWs and NTs rather than samples comprising thousands or millions of NWs or NTs. This chapter introduces some of the challenges in single-NW measurements and then presents the detailed thermal and mechanical design of a new type of thermal probe developed as a part of this thesis work. The probe is based on commercially-available Wollaston wire, a marked departure from the microfabricated measurement platforms previously described in the literature. The Wollaston wire probes are easier to assemble than the microfabricated measurement platforms, and have the potential for better sensitivity as well. Wollaston wire probes can be used to measure the thermal conductivity, electrical conductivity, and Seebeck coefficient of individual NWs and NTs, and they have been deployed inside of a high-resolution transmission electron microscope (TEM) to correlate the measurements with detailed observations of atomic structure. Some preliminary thermoelectric measurements are presented below.

Because the techniques described in this chapter apply equally well to measurements of nanowires and nanotubes, in this chapter the terms "NW" and "NT" should be treated interchangeably.

5.1.1 Challenges in the thermal measurements of individual nanowires and nanotubes

The two greatest challenges in measuring the thermal resistance of a single NW or NT are: (1) that the thermal resistance of a single NW is very large, requiring very high levels of thermal isolation; and (2) the difficulty in obtaining good thermal contact to the ends of the NW. These two challenges can be understood from Fig. 5-1(a,b), which depicts a generic system for thermal measurements of single NWs. A suspended NW bridges between a hot platform and a cold sink. Heat is generated at the hot platform and flows through the NW, causing a temperature difference between the hot platform and cold sink. By measuring the temperature difference across the NW and the heat flow through the NW, the

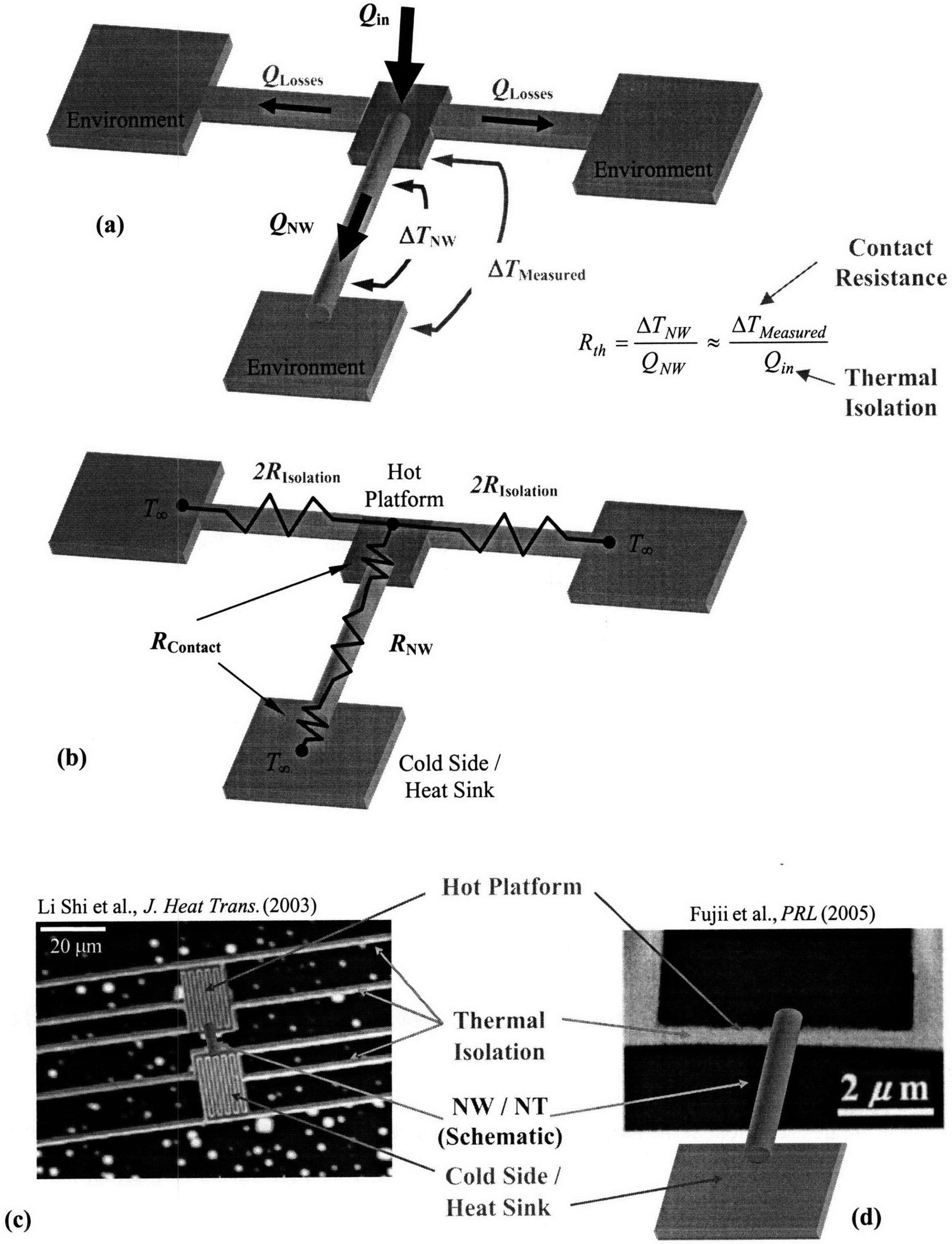

Figure 5-1. (a) Schematic of a generic experiment to measure the thermal resistance of a single nanowire or nanotube. Some of the heat input at the hot platform is lost, rather than flowing through the nanowire. The measured temperature drop includes the temperature drop across any thermal contact resistance. (b) Equivalent thermal circuit of (a). (c&d) Two previous approaches to measure the thermal resistance of a single nanowire or nanotube [2, 7]. Both of these systems rely on microfabrication to achieve sufficiently large thermal isolation resistance.

thermal resistance of the NW can be calculated. Finally, using knowledge of the NW geometry, its thermal conductivity can be calculated. One problem is that some of the heat generated at the hot platform may flow through the supports of the hot platform, rather than through the NW. This heat leakage can be corrected for if the thermal resistance of these supports (the "isolation resistance") is known [Fig. 5-1(b)]. For best sensitivity the isolation resistance should be much larger than the NW resistance, and in fact the measurement will fail if the isolation resistance is much smaller than the NW resistance. Furthermore, the measured temperature difference is generally that between the hot platform and cold sink, and thus includes the undesired temperature drop across any thermal contact resistances. In theory this issue could be bypassed by implementing a four-point temperature measurement, but it would be considerably more difficult to create and align two more temperature probes at the scale of an individual NW. If the contact resistances were known they could be subtracted from the total measured thermal resistance, but it is difficult to estimate the contact resistances and they also may not be very repeatable between different measurements. The only satisfactory solution is to create contacts with much lower thermal resistance than the NW. Besides the problems of heat leakage and contact resistance, additional experimental issues include physically aligning the target NW to the measurement apparatus, measuring the geometry of the NW accurately, and devising a measurement scheme sensitive enough to detect the small thermal signals of a single NW.

5.1.2 Previous thermal measurements of individual nanowires and nanotubes

Although the field of single-NW thermal measurements is still young, the challenges just described have been addressed in two types of experimental systems reported in the literature. Li Shi and co-workers [1-6] pioneered the field by using microfabrication to create two platforms suspended on long, slender beams made of silicon nitride [Fig. 5-1(c)]. Each platform has a serpentine (i.e. meandering) metallic heater, which is also used to measure the temperature of the platform using resistive thermometry. A single NW is deposited somewhat randomly between the two platforms by allowing a drop of a NW suspension to dry in place. In some cases a carbon NT can be grown in-situ. The thermal contacts are improved by local deposition of amorphous carbon and/or platinum by an electron beam or ion beam technique. More recently, Fujii and co-workers [7] used electron-beam lithography to pattern a very thin metallic line heater which is also used to measure temperature [Fig. 5-1(d)]. A manipulation probe inside a scanning electron microscope (SEM) is used to suspend a NT between a heat sink and the midpoint of the line heater. The thermal contacts are again improved by local deposition of amorphous carbon.

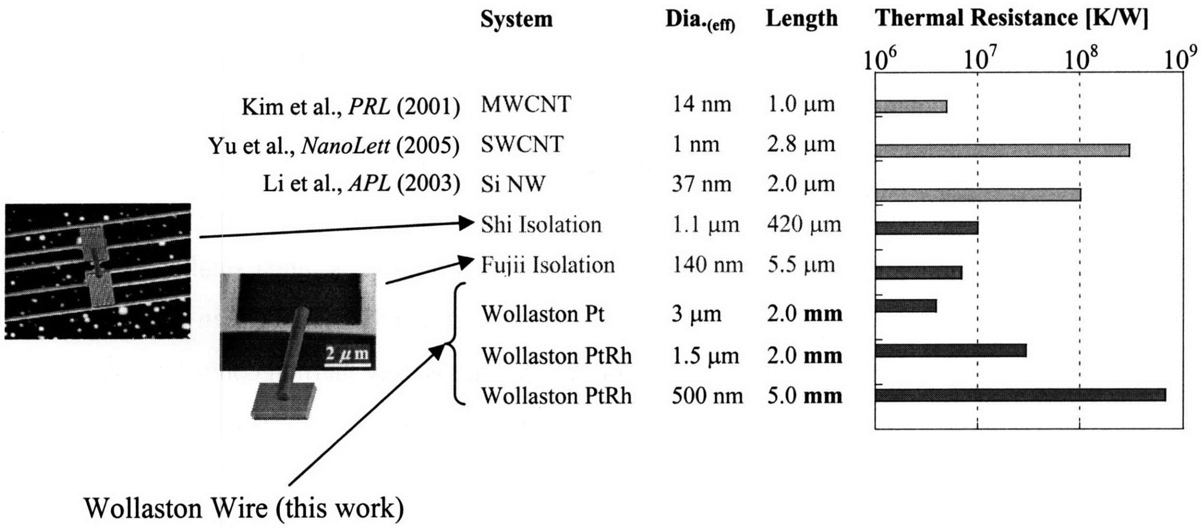

Figure 5-2. Thermal resistances of several representative NT and NW, compared with the isolation thermal resistances of the Shi *et al.* and Fujii *et al.* platforms and several Wollaston wire probes.

The Shi *et al.* and Fujii *et al.* platforms have proven valuable for the first measurements of the thermal resistance of individual NWs and NTs. However, they do have some limitations. Fig. 5-2 compares the thermal isolation resistance of both the Shi *et al.* and the Fujii *et al.* measurement platforms with the resistance of several NWs and NTs. It is clear that even with such long and slender measurement platforms, the isolation resistance is still smaller than, or at best comparable to, the NW resistance. Thus these measurements require significant corrections for the heat leakage through the supports, especially for the NWs with large thermal resistances. A second limitation is that both schemes require time and resources to be invested in the microfabrication. Also, implementations that rely on deposition of suspended NWs out of solution have a significant degree of randomness in getting a NW of desired geometry (length and diameter) to deposit onto one of the measurement platforms. This inherent randomness also limits the speed at which multiple samples can be prepared and measured. The Fujii *et al.* approach may have higher throughput because of the ability to select individual NWs for measurement, but lacks the ability of Shi *et al.*'s platform to measure the Seebeck coefficient. Finally, in most prior schemes the NW geometry was measured by SEM or atomic force microscopy (AFM), both of which may have limited accuracy in certain dimensions: SEM measurements have several nanometers of uncertainty for in-plane distances and cannot measure out-of-plane distances, while AFM measurements also have nanometer-level uncertainty in-plane but improve to Ångstrom-level uncertainty out-of-plane.

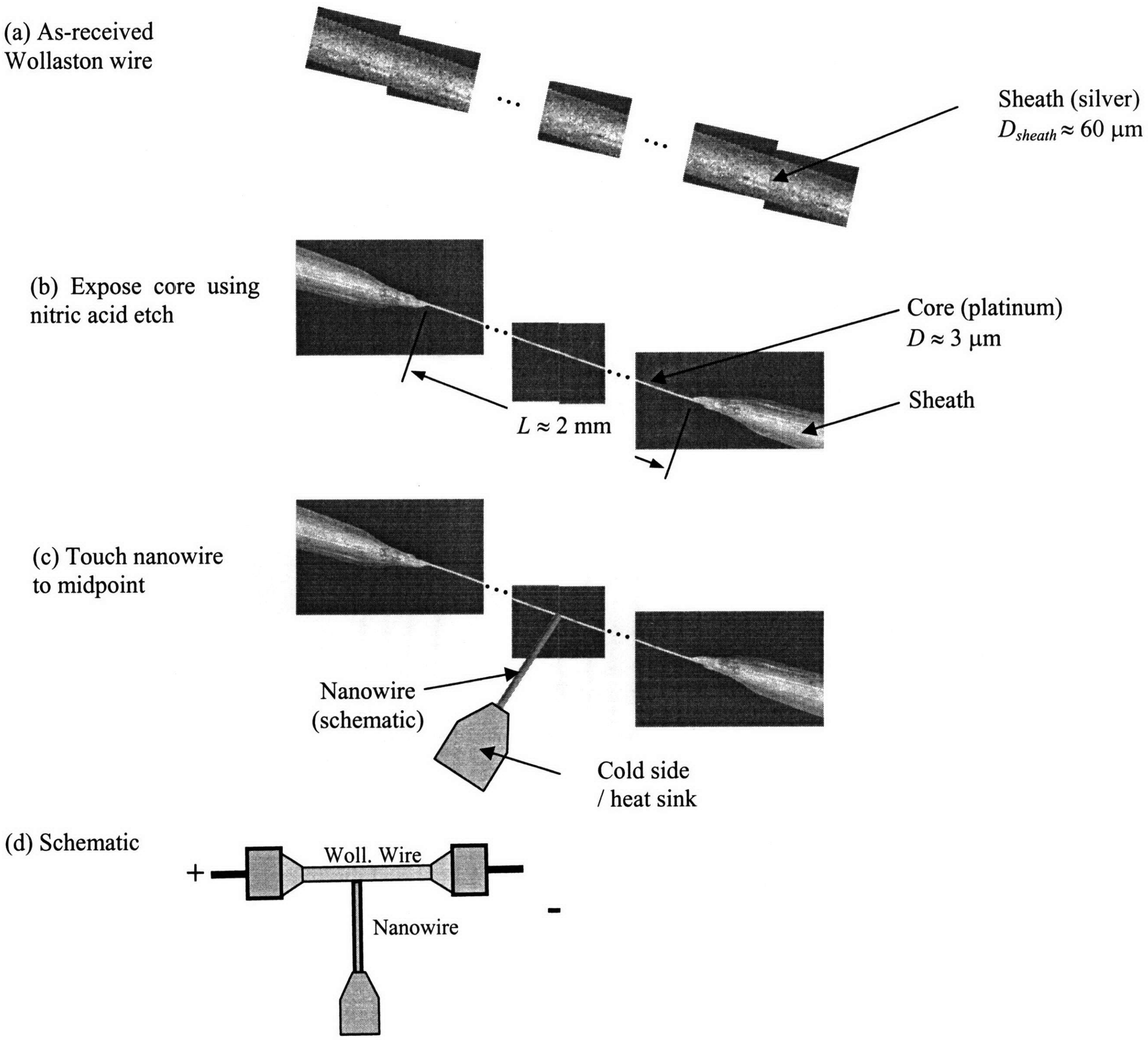

Figure 5-3. Etching Wollaston wire to make a thermal probe. (Diagrams are for the sake of illustration only: some micrographs were duplicated and shifted.)

5.2 Basic concept of the Wollaston wire thermoelectric probe

The Wollaston wire probe developed in this thesis has several advantages compared to the earlier techniques of Shi *et al.* [1-4] and Fujii *et al* [7]. As described below, it offers comparable or higher thermal isolation resistance yet requires no microfabrication, has the potential for high throughput, has the ability to select an arbitrary NW or NT for measurement, can measure the Seebeck coefficient, and, as currently implemented inside a high-resolution TEM, has atomic-level accuracy in determining the geometry of the sample. Disadvantages compared to the prior approaches include the need for skilled

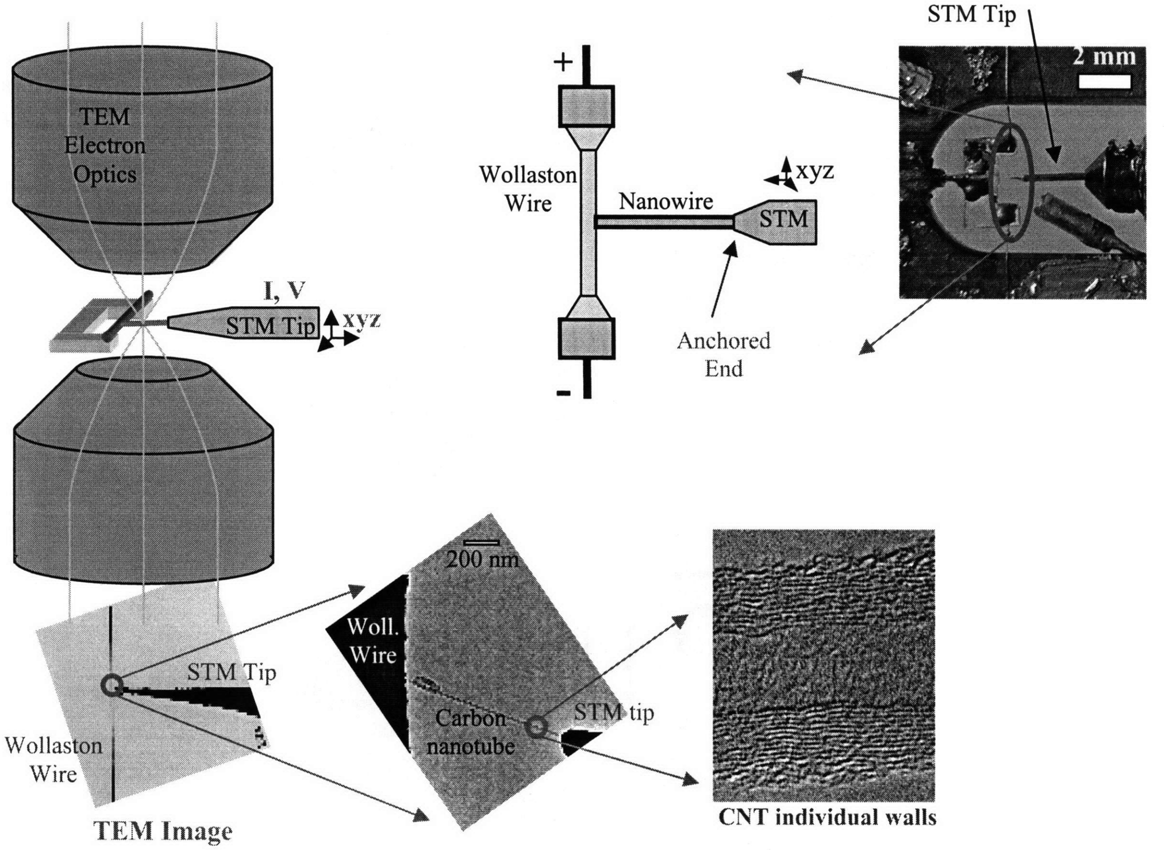

Figure 5-4. Schematic of Wollaston wire probe integrated inside a high-resolution TEM for in-situ thermoelectric measurements of individual nanowires and nanotubes. STM=scanning tunneling microscope.

manual assembly of one delicate Wollaston wire probe at a time, the need to pretension the Wollaston wire, and the lack of on/off control when depositing contacts in-situ.

Wollaston wire is normally used in hot-wire anemometry to measure the velocity and/or temperature of a flowing gas [8-11]. A typical, commercially-available Wollaston wire (Sigmund-Cohn Corp., Mount Vernon, NY) comprises a silver sheath (outer diameter about 50 - 100 μm) surrounding a core of platinum or platinum-rhodium alloy (Fig. 5-3). The as-received core diameters range from a few tens of microns down to around 0.5 micron, and they can be drawn down even smaller [12]. A simple etch in nitric acid is used to remove the silver sheath from a select region, exposing the platinum core. Platinum and platinum-rhodium are not etched by nitric acid. With practice it is fairly easy to control the length of this etched region from several millimeters down to hundreds of microns. Because the core diameter is so small, and the etched lengths can be relatively long, the thermal isolation resistance of such a length of Pt or Pt/Rh core can be similar to or even much larger than the isolation resistance of the

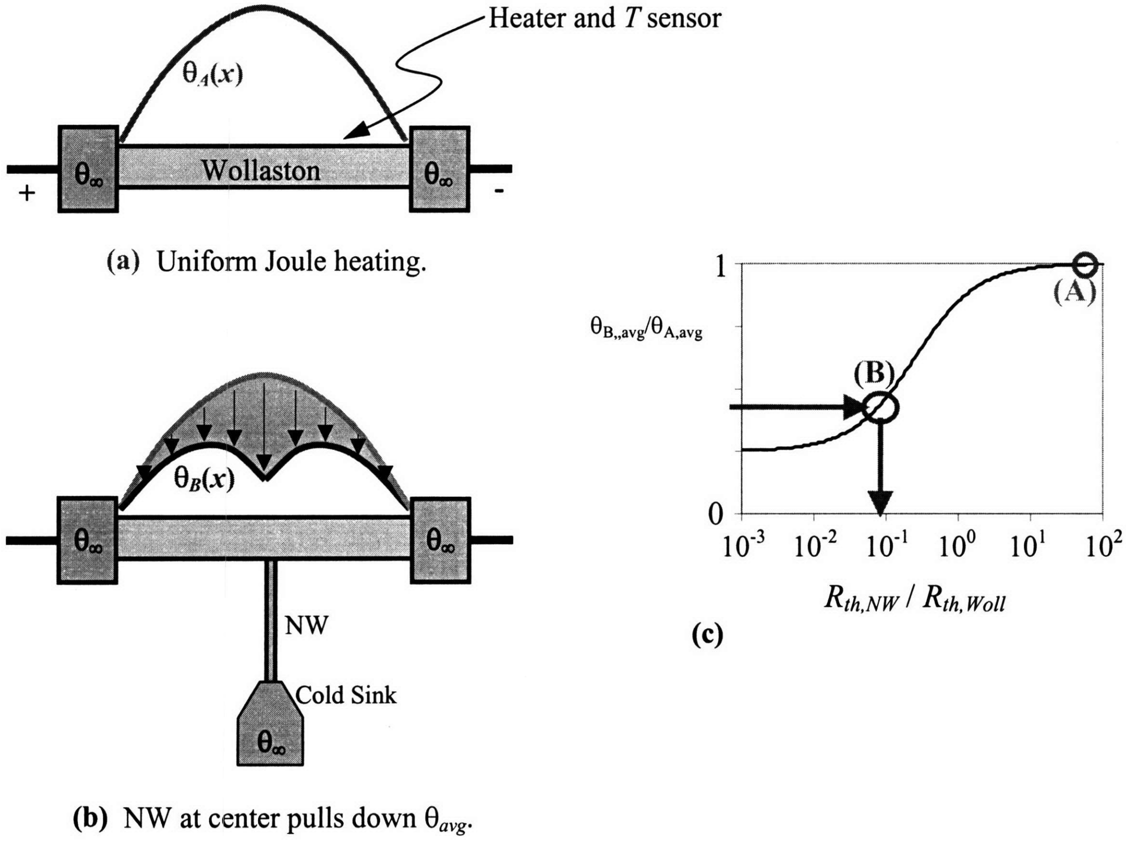

(a) Uniform Joule heating.

(b) NW at center pulls down θ_{avg}.

(c)

Figure 5-5. Basic concept of thermal conductivity measurements using a Wollaston wire probe. (a) Baseline temperature profile $\theta_A(x)$ for a bare Wollaston wire with steady DC current, neglecting convection and radiation. The Wollaston wire is both the heat source and, through resistance thermometry, the temperature sensor. (b) Depressed temperature profile $\theta_B(x)$ after touching a nanowire to the center of the Wollaston wire. (c) Ratio of the spatially averaged temperatures $\theta_{B,avg} / \theta_{A,avg}$ as a function of the ratio of thermal resistances $R_{th,NW}/R_{th,Woll}$. By measuring the temperature ratio, the thermal resistance ratio can be determined.

previously reported measurement platforms (Fig. 5-2). This opens up the possibility of fundamentally better sensitivity when studying NWs of very high thermal resistance (> 10^8 K/W).

The basic Wollaston wire thermoelectric probe, depicted inside a TEM in Fig. 5-4, can be used to measure the thermal conductance of an individual NW with a technique very similar to that of Fujii *et al.* [7], although conceived independently. Figure 5-5 presents the basic concept. The essential idea is to pass a steady DC current through the Wollaston wire, and to measure the resulting temperature rise of the Wollaston wire both with [Fig. 5-5(b)] and without [Fig. 5-5(a)] the bridging NW. Without the NW, and assuming perfect contacts and no losses to radiation or convection, the steady-state temperature profile will be a parabola. By measuring the electrical resistance of the Wollaston wire, its average temperature can be determined using the temperature coefficient of resistivity. Then, with the NW in place, some of the joule heat from the Wollaston wire can leak out through the NW, rather than conducting through the length of the Wollaston wire. The temperature profile now consists of two parabolic regions joined with a kink at the point where the NW touches the Wollaston wire. The average temperature is reduced due to this heat leakage, and a simple calculation yields the thermal resistance of the NW. The detailed thermal and mechanical analysis of this system are described in the next section.

Although it is possible to implement the Wollaston wire measurement inside a cryostat and use an optical microscope to align the NW to the Wollaston wire, we are currently pursuing experiments inside a high-resolution transmission electron microscope (Fig. 5-4). This TEM, a JEOL 2010F located at Boston College, has a special sample holder with a built-in scanning tunneling microscope (STM) (Nanofactory Instruments). The STM is normally used to probe current and voltage with very high spatial resolution (~Ångstrom-level) in 3 dimensions. We have modified this sample holder by adding a Wollaston wire probe. A length of the Pt core about 2 mm long is electrically and thermally anchored at each end through its unetched leads to the surrounding environment. The manipulation capabilities of the STM are used to select a NW and attach one end to the approximate midpoint of the Wollaston wire. The other end of the NW is anchored electrically and thermally to the STM probe, which itself is well-coupled to the surrounding environment. Electrical connections are made to both ends of the Wollaston wire as well as to the STM tip. The rest of this chapter describes how this experimental configuration can be used to measure the thermal conductance, electrical conductance, and Seebeck coefficient of the NW.

5.3 Thermal and mechanical design of a Wollaston wire probe

5.3.1 Solution of the heat equation for a Wollaston wire with bridging nanowire

Neglecting convection and radiation, the steady, one-dimensional heat equation for a Wollaston wire of length L and constant cross sectional area S is

$$k\frac{d^2\theta_x}{dx^2}=-\frac{I^2R_{e0}}{SL} \tag{5-1}$$

Here x is the coordinate along the NW length, k is the thermal conductivity of the Wollaston wire, I is the electrical current, and R_{e0} is the electrical resistance of the Wollaston wire at the reference temperature. Also $\theta_x(x)$ is the local temperature of the Wollaston wire minus the reference temperature of the surrounding environment (θ_∞=0), to be contrasted with θ (no subscript) which is the spatially averaged temperature, used later. Expressing the heat source term in this way neglects the higher-order effects on the joule heating due to small changes in electrical resistance with temperature [13], which is a good approximation in the present circumstances. One end of a NW of thermal resistance $R_{th,NW}$ is placed at x=0, the midpoint of the Wollaston wire, and the other end of the NW is anchored to a heat sink at θ_∞=0 This boundary condition can be expressed as

$$\frac{\theta_x(0)-\theta_\infty}{R_{th,Woll}} = kS\left(\left.\frac{\partial\theta_x}{\partial x}\right|_{x=0^+} - \left.\frac{\partial\theta_x}{\partial x}\right|_{x=0^-}\right). \tag{5-2}$$

Because the Pt core and Ag sheath of the Wollaston wire are in intimate contact at both ends of the exposed core, for the other boundary condition we assume perfect thermal contacts:

$$\theta_x(+L/2) = \theta_x(-L/2) = 0\,. \tag{5-3}$$

The solution of Eqs. (5-1) - (5-3) is

$$\theta_x(x,\gamma) = \left(\frac{I^2 R_{e0} L}{8kS}\right)\left[\left(1-\left(\frac{x}{L/2}\right)^2\right)+\left(\frac{\gamma}{1+\gamma}\right)\left(-1+\left|\frac{x}{L/2}\right|\right)\right], \tag{5-4}$$

and is depicted in Fig. 5-6(a). It is convenient to introduce a dimensionless parameter, γ, defined as one-quarter of the ratio of the Wollaston wire thermal resistance to the NW thermal resistance:

$$\gamma \equiv \frac{R_{th,Woll}}{4R_{th,NW}}\,. \tag{5-5}$$

The reason for the factor of 4 will become apparent later, below Eq. (5-27).

The electrical resistance of the Wollaston wire, R_e, depends only on the spatial average of its temperature:

$$R_e = R_{e0}\left[1+\alpha\left(\frac{1}{L}\int_{-L/2}^{L/2}\theta_x(x)dx\right)\right] = R_{e0}(1+\alpha\theta) \tag{5-6}$$

where α is the temperature coefficient of resistivity and θ is the spatially averaged temperature. Thus, measurements of the electrical resistance of the Wollaston wire reveal the *average* temperature of the Wollaston wire. This is not ideal, because to analyze the thermal properties of the NW we are more interested in the temperature at x=0 than the average along the entire Wollaston wire. Thus, one important goal of the thermal modeling is to relate the average temperature θ to the point temperature $\theta_x(0)$. Because the analysis assumes that the Wollaston wire has homogenous properties, constant cross section, and linear behavior, any non-idealities will introduce some errors in relating the average

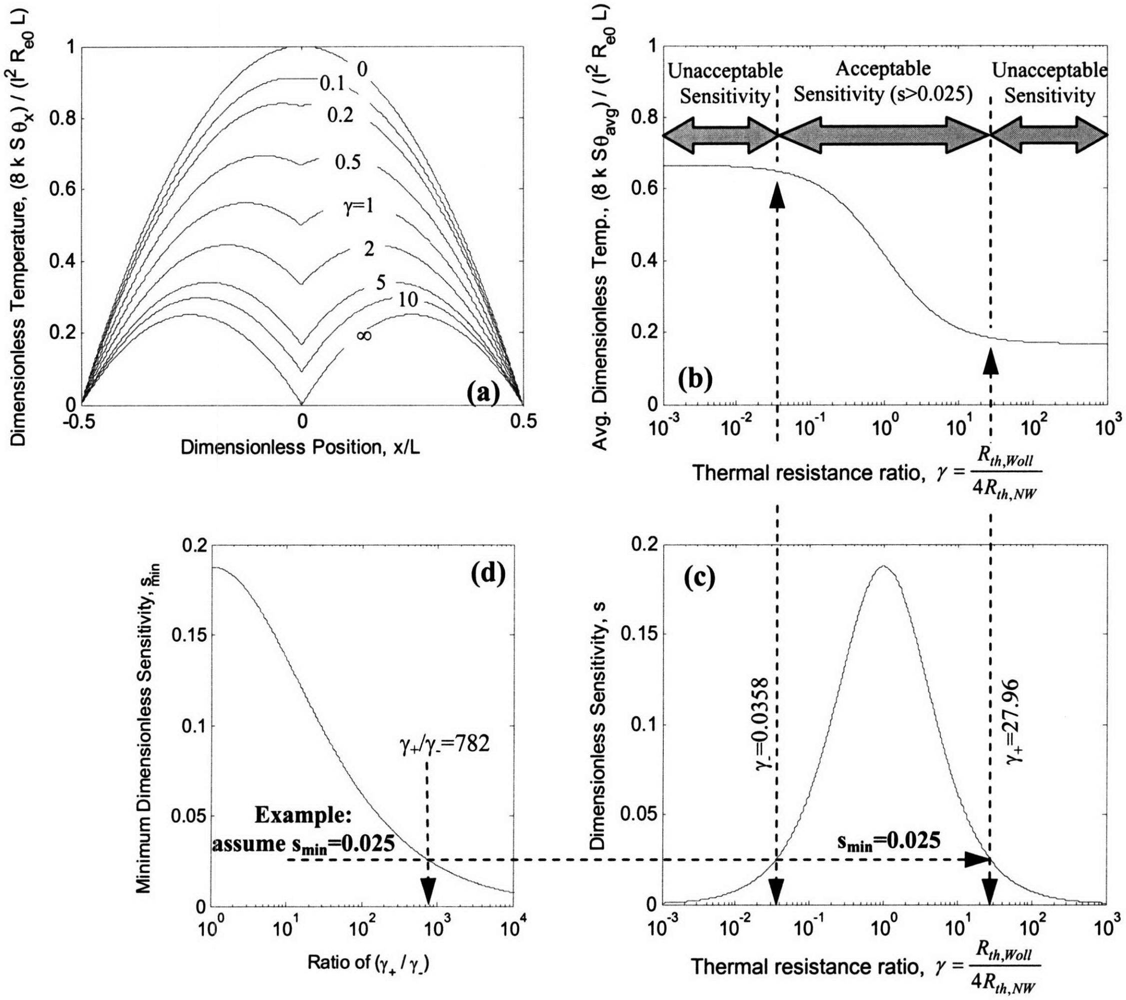

Figure 5-6. Solutions of the heat equation for a Wollaston wire thermal probe with a nanowire or nanotube touching its midpoint. (a) Spatial temperature profiles $\theta_x(x,\gamma)$, for various values of the thermal resistance ratio γ. (b) Dependence of the spatially-averaged temperature rise on the thermal resistance ratio γ. (c) Sensitivity as a function of the thermal resistance ratio, γ, showing that best sensitivity is achieved when $\gamma=1$. (d) Range of permitted thermal resistance ratios (γ_+/γ_-) as a function of the minimum sensitivity, s_{min}. The dashed lines in panels (b)-(d) depict an example calculation for a particular scenario with $s_{min}=0.025$ (see text). For this value of s_{min}, panel (c) shows that γ must lie between 0.0358 and 27.96 in order for the experiment to have acceptable sensitivity. The range of acceptable sensitivity indicated in panel (b) is only relevant for the example scenario where $s_{min}=0.025$. A lower value of s_{min} will give a broader range of acceptable γ.

temperature rise to the NW properties. Ignoring any such non-idealities, the average temperature of the profiles of Eq. (5-4) is given by

$$\theta(\gamma) = \left(\frac{I^2 R_{e0} L}{12kS}\right)\left[1 - \frac{3}{4}\left(\frac{1}{1+\gamma^{-1}}\right)\right], \qquad (5\text{-}7)$$

and is depicted in Fig. 5-6(b).

As described in Chapter 4, this system may also be characterized in terms of a thermal transfer function Z, defined in Eqs. (4-1)-(4-4) as the ratio of θ / Q, where in this chapter the heat input Q is the joule heating of the Wollaston wire, $I^2 R_{e0}$. Depending on the frequency of the heat source compared to the longitudinal thermal diffusion time, the experiment can be treated in low- or high-frequency limits. For quick estimates of the transition frequency, heat loss through the NW can be ignored, making the Wollaston wire experiment identical to the "suspended wire" (SW) configuration considered in Chapter 4. In this limit the thermal diffusion time τ is given simply by

$$\tau \approx L^2 / \kappa \tag{5-8}$$

where κ is the thermal diffusivity of the Wollaston wire. The transition frequencies are then readily estimated from Fig. 4-3 of Chapter 4. That figure shows that the low-frequency limit is a good approximation when $\omega_H \tau < 1$, and the high-frequency limit when $\omega_H \tau > 100$, where the H subscript refers to the frequency of the heater. For a typical Pt Wollaston wire of length 2 mm at 300 K, $\kappa = 2.5 \times 10^{-5}$ m^2/s and $\tau \approx 0.16$ s, resulting in the requirements $(\omega_H / 2\pi) < 1$ Hz (low-frequency limit) and $(\omega_H / 2\pi) > 100$ Hz (high-frequency limit). It is easy to experimentally verify that the limiting behavior has been achieved by varying the frequency by a factor of approximately 10 (for example, from 0.1 Hz to 1 Hz) and confirming that the voltages remain constant.

In the low-frequency limit the thermal mass of the Wollaston wire and NW can be neglected, and the system is described by the quasistatic analysis of Eqs. (5-1)-(5-5). In this case inpsection of Eq. (5-7) reveals that the transfer function is

$$Z(\gamma, \omega \to 0) = \tfrac{1}{12} R_{th,Woll} \left[1 - \frac{3}{4} \left(\frac{1}{1+\gamma^{-1}} \right) \right], \tag{5-9}$$

with no imaginary part. At both small and large γ this transfer function tends to a constant value, but the large-γ limit is four times smaller than the small-γ limit. This is because $\gamma \to \infty$ means $R_{th,NW} \to 0$, which is equivalent to anchoring the midpoint of the Wollaston wire to the temperature of the surroundings, $\theta_x(0) = \theta_\infty = 0$. Because the temperature profile is quadratic in x, reducing the effective length by a factor of 2 reduces the average temperature rise by a factor of 4.

In the high frequency limit, the heating period is so brief that the amplitude of the characteristic temperature rise becomes negligible:

$$\theta(\omega \to \infty) \approx \frac{\pi I^2 R_{e0}}{\omega m c} \to 0 \tag{5-10}$$

where m is the mass of the Wollaston wire and c is its specific heat. Thus, in the high-frequency limit both the real and imaginary parts of Z go to zero:

$$Z(\gamma, \omega \to \infty) \to 0 + 0j\,. \tag{5-11}$$

The thermal transfer function for intermediate frequencies is a more complicated function of the properties of the NW and Wollaston wire, but this regime is easily avoided by selecting the appropriate frequency of the driving current.

Measurements are typically performed in the low-frequency limit (for example, using currents with frequencies below 0.5 Hz). Applying the thermal transfer function of Eq. (5-9) to the in-phase 1ω entry of Table 4-1 of Chapter 4, we see that the ratio of the resulting sinusoidal voltage drop across the Wollaston wire to the driving current is the electrical resistance

$$R_e(\gamma, \omega \to 0) \equiv \frac{V_{1\omega,rms}}{I_{1\omega,rms}} = R_{e0}\left[1 + \tfrac{1}{8}\alpha\, Q_{avg} R_{th,Woll}\left(1 - \frac{\frac{3}{4}}{1+\gamma^{-1}}\right)\right] \tag{5-12}$$

where Q_{avg} is defined as the time-averaged heat input:

$Q_{avg} \equiv I_{1\omega,rms}^2 R_{e0}$

The experiment can also easily be performed in the high-frequency limit (for example, by driving the current faster than 100 Hz). Recall from Table 4-1 of Chapter 4 that $V_{1\omega,rms}$ depends on $Z(0)$ as well as $Z(\omega)$ and $Z(2\omega)$. But according to Eq. (5-11) the latter two terms are negligible in the high-frequency limit, so that the 1ω voltage is only sensitive to the DC behavior of Z. The thermal contribution to the voltage drop is only 2/3 as large as in a low-frequency experiment, and so the factor (1/8) in Eq. (5-12) should be replaced by (1/12):

$$R_e(\gamma, \omega \to \infty) \equiv \frac{V_{1\omega,rms}}{I_{1\omega,rms}} = R_{e0}\left[1 + \tfrac{1}{12}\alpha\, Q_{avg} R_{th,Woll}\left(1 - \frac{\frac{3}{4}}{1+\gamma^{-1}}\right)\right] \tag{5-13}$$

Thus, the high-frequency measurement is only 2/3 as sensitive as the low-frequency measurement. Physically, this is because a very high frequency AC current results only in DC heating, while a very slow AC current results in both DC and AC heating that can be tracked by the Wollaston wire quasistatically.

In either the low- or high-frequency limits, the measured electrical resistance can be used to determine the thermal resistance of the NW. First a baseline measurement is necessary to determine the thermal resistance of the Wollaston wire [Fig. 5-5(a)]. For example, in the low frequency limit the electrical resistance can be plotted as a function of the average heat input. The resulting slope gives $R_{th,Woll}$:

$$R_{th,Woll} = \frac{8}{\alpha R_{e0}} \left(\frac{\partial R_e}{\partial Q_{avg}} \right)_{\text{no NW}} \tag{5-14}$$

while in the high frequency limit the 8 is replaced by 12. Because the geometry and thermal conductivity of the Wollaston wire are presumably already known, this measurement provides a useful check of the equipment and data analysis. After touching a NW to the midpoint of the Wollaston wire [Fig. 5-5(b)], the new slope $(\partial R_e/\partial Q_{\text{avg}})_{touching\ NW}$ gives the thermal resistance of the NW. It is convenient to define the ratio of the slopes as

$$\phi \equiv \frac{\left(\frac{\partial R_e}{\partial Q_{avg}} \right)_{touching\,NW}}{\left(\frac{\partial R_e}{\partial Q_{avg}} \right)_{no\,NW}} \tag{5-15}$$

and also the difference in slopes

$$\varepsilon \equiv 1 - \phi = \frac{\left(\frac{\partial R_e}{\partial Q_{avg}} \right)_{no\,NW} - \left(\frac{\partial R_e}{\partial Q_{avg}} \right)_{touching\,NW}}{\left(\frac{\partial R_e}{\partial Q_{avg}} \right)_{no\,NW}}. \tag{5-16}$$

Finally, the NW thermal resistance is given by

$$R_{th,NW} = \tfrac{1}{4} R_{th,Woll} \left(\frac{\tfrac{3}{4}}{1-\phi} - 1 \right) \tag{5-17}$$

$$= \tfrac{1}{4} R_{th,Woll} \left(\tfrac{3}{4} \varepsilon^{-1} - 1 \right) \tag{5-18}$$

where all quantities on the right-hand-side are known. This formula has not yet been checked experimentally against a standard NW sample such as a silicon nanowire of large diameter. Although Eqs. (5-17) and (5-18) are nonlinear in the measured quantities such as $(\partial R_e/\partial Q_{\text{avg}})_{touching\ NW}$, Eq. (5-18) does lend itself to linearization in the common limit of $R_{th,NW} >> R_{th,Woll}$. In this case $\varepsilon^{-1} >> 1$ and the NW thermal *conductance* is linearly proportional to the change in slopes:

$$R_{th,NW}^{-1} = \tfrac{16}{3} R_{th,Woll}^{-1} \left[\frac{\left(\frac{\partial R_e}{\partial Q_{avg}} \right)_{no\,NW} - \left(\frac{\partial R_e}{\partial Q_{avg}} \right)_{touching\,NW}}{\left(\frac{\partial R_e}{\partial Q_{avg}} \right)_{no\,NW}} \right]. \tag{5-19}$$

Note that using the *ratios* of slopes in Eqs. (5-15) through (5-19) has the benefit of canceling out quantities such as the temperature coefficient of resistance α and the cold-wire resistance R_{e0}, thus reducing the number of parameters which can contribute to experimental uncertainty.

5.3.2 Lorentz number considerations

Because of the wide range of Wollaston wire lengths and diameters that can be fabricated, it is important to consider the relationships between current, voltage, and the geometry and properties of the Wollaston wire. It turns out that the relationship between the average temperature rise θ and the voltage drop across the Wollaston wire is nearly independent of the Wollaston wire geometry and material. This surprising result can be understood by the following argument. The average temperature rise of the Wollaston wire (in the absence of the NW) is given by Eq. (5-7) as

$$\theta = Q_{avg} R_{th,Woll} / 12 \tag{5-20}$$

where as explained in Chapter 4 the factor of 12 arises for this particular configuration of an isolated, uniformly heated wire with thermally-clamped ends. The average heating can be expressed as

$$Q_{avg} = \frac{V_{rms}^2}{R_{e0}}, \tag{5-21}$$

so

$$\theta = \tfrac{1}{12} V_{rms}^2 R_{th,Woll} / R_{e0}. \tag{5-22}$$

But because the Wollaston wire is metallic, we can apply the Wiedemann-Franz law relating the ratio of thermal resistance to electrical resistance:

$$\frac{R_{th,Woll}}{R_{e0}} = \frac{\sigma}{k} \approx \frac{1}{L_0 T} \tag{5-23}$$

where L_0 is the Lorentz number and T is the absolute temperature. Thus

$$\theta \approx \frac{V^2}{12 L_0 T} \tag{5-24}$$

Remarkably, this expression now shows that the average temperature rise is independent of all geometric factors, and, to the extent that the Lorentz number can be considered approximately constant, independent even of the choice of the Wollaston wire material. For quick calculations it is convenient to express this baseline temperature rise as

$$\theta \approx (1\,\mathrm{K})(V/9.4\,\mathrm{mV})^2 \tag{5-25}$$

where the characteristic voltage of 9.4 mV assumes a 300 K ambient and the standard value of 2.45 x 10^{-8} V^2/K^2 for the Lorentz number. Eq. (5-24) should be useful for metallic Wollaston wires over a wide range of temperatures (as long as the Wiedemann-Franz law is approximately valid). If this same measurement technique were used with a semiconducting "Wollaston wire," Eq. (5-24) would not be expected to be valid because the significant contribution of phonons to the total thermal conductivity will invalidate Eq. (5-23).

Equation (5-25) shows that for typical room temperature experiments imposing a temperature rise at the Wollaston wire of approximately 1 - 10 K, the voltages across the Wollaston wire will range from approximately 10 mV to 30 mV, regardless of the geometry or material of the Wollaston wire. This has been verified approximately for several Wollaston wires made from both Pt and PtRh cores, with diameters ranging from about 0.6 μm to about 3 μm. Voltages in this range are convenient for experiments. The magnitudes of the currents are also reasonable, but vary over a much larger range, because the electrical resistance of the Wollaston wire will change depending on its geometry and material (typically about 30 - 300 Ω).

5.3.3 Thermal matching is required for good sensitivity

The analysis of Eq. (5-7) and Fig. 5-6(b) reveals an important limitation of this technique: the thermal resistance of the Wollaston wire needs to be approximately matched to the thermal resistance of the NW in order for the measured temperature to have good sensitivity to *changes* in the thermal resistance of the NW. Consider the change in the temperature of the Wollaston wire for a given change in the thermal conductance of the bridging NW. For a sensitive measurement of $R_{th,NW}$, we would like small changes in $R_{th,NW}$ to result in large changes in the measured temperature. To quantify this concept, we can define a dimensionless sensitivity as

$$s \equiv \frac{(\text{relative change in } \theta \text{ of Wollaston wire})}{(\text{relative change in thermal resistance of nanowire})} = \frac{(\delta\theta/\theta_0)}{(\delta R_{th,NW}/R_{th,NW})} \tag{5-26}$$

where θ_0 is the average temperature of the Wollaston wire before touching it with the NW, $\delta\theta$ is the uncertainty in the measured temperature, and $\delta R_{th,NW}$ is the uncertainty in the calculated $R_{th,NW}$. A large sensitivity minimizes $\delta R_{th,NW}$.

Applying this definition of s to Eq. (5-7), we see that the sensitivity is related to the thermal resistances through

$$s = \frac{3\gamma}{4(1+\gamma)^2} = \tfrac{3}{4}\left(\gamma^{\frac{1}{2}} + \gamma^{-\frac{1}{2}}\right)^{-2} \tag{5-27}$$

This dependence is depicted in Fig. 5-6(c). It is clear that the sensitivity approaches zero in the limit of very large and very small $R_{th,NW}$, which is also apparent from the asymptotically flat regions of Fig. 5-6(b). It is also clear that s is symmetric about γ=1 on a semi-log plot, that is, $s(\gamma)=s(1/\gamma)$. The factor of 4 in the definition of γ [Eq. (5-5)] was introduced in order to provide this symmetry.

An important practical question is just how well $R_{th,Woll}$ must match $R_{th,NW}$ in order to achieve a specified level of experimental accuracy, expressed as

$$\left(\delta R_{th,NW} / R_{th,NW}\right) < \left(\delta R_{th,NW} / R_{th,NW}\right)_{\max} \tag{5-28}$$

As a concrete example, consider an experiment to determine the thermal resistance of the NW with an uncertainty of less than 20%. In order to minimize the ambiguity about which temperature of the NW corresponds to the measured properties, we will limit the average temperature rise of the Wollaston wire before touching the NW to θ_0 =10 K. Furthermore, the experimental configuration and equipment limitations will result in some minimum uncertainty in the measured Wollaston wire temperature, $\delta\theta$, of perhaps ± 0.05 K. What then is the range of γ that can be tolerated to achieve this specified level of uncertainty in $R_{th,NW}$? This condition is equivalent to requiring $s>s_{min}$, where

$$s_{\min} = \frac{(\delta\theta / \theta_0)}{\left(\delta R_{th,NW} / R_{th,NW}\right)_{\max}} \tag{5-29}$$

In this example, s_{min}=(0.05 K / 10K)/(20%)=0.025. Solving Eq. (5-27) for γ yields the two roots

$$\gamma_+ = \frac{3 - 8s_{\min} + \sqrt{9 - 48s_{\min}}}{8s_{\min}}, \tag{5-30}$$

$$\gamma_- = \frac{3 - 8s_{\min} - \sqrt{9 - 48s_{\min}}}{8s_{\min}}. \tag{5-31}$$

For best sensitivity, an ideal Wollaston wire probe should be designed with γ=1. However, the uncertainty in $R_{th,NW}$ will still be less than the allowable uncertainty as long as

$$\gamma_- < \gamma < \gamma_+, \tag{5-32}$$

Note that Eqs. (5-30) and (5-31) only have solutions for s_{min}<3/16: that is, the best possible sensitivity is s=3/16, which is achieved only when γ=1. Also note that γ_- always equals $1/\gamma_+$. In this example, γ_- =0.0358 and γ_+=27.96, so γ is allowed to range from

$$0.0358 < \gamma < 27.96 \qquad (5\text{-}33)$$

to ensure that the uncertainty in $R_{th,NW}$ is less than 20%. Thus, in this example the thermal resistance of the NW must be estimated in advance to within a factor of about 28 of its true value, in order to design the Wollaston wire probe with appropriate thermal resistance. That is, the Wollaston wire probe will be designed to achieve $\gamma=1$ based on the *estimated* $R_{th,NW}$. As long as the *true* $R_{th,NW}$ is within a factor of 28 of the estimate, the true value of γ will lie between 0.0358 and 27.96, and the uncertainty in $R_{th,NW}$ will be less than 20%. In the best case, $\gamma=1$, from Eq. (5-26) we see that the uncertainty in $R_{th,NW}$ would be improved to 2.67%. In general, the range of allowable γ spans

$$\frac{\gamma_+}{\gamma_-} = \frac{3-8s_{\min}+\sqrt{9-48s_{\min}}}{3-8s_{\min}-\sqrt{9-48s_{\min}}} \qquad (5\text{-}34)$$

As shown in Fig. 5-6(d), this range is a very strong function of s_{min}. The range of allowable γ can be greatly increased by (1) tolerating greater relative uncertainty in $R_{th,NW}$, (2) reducing the uncertainty in temperature measurements $\delta\theta$, or (3) increasing the baseline temperature rise θ_0. The latter strategy will also introduce ambiguity about the effective temperature of the NW properties, and may cause problems with thermal expansion if it overwhelms the pretension of the Wollaston wire (described further below). For the most accurate results it may be necessary to perform two measurements: first to determine the approximate $R_{th,NW}$, and then a second measurement with a fresh Wollaston wire probe optimized to have γ close to unity.

5.3.4 Thermal contact resistance and spreading resistance

Thermal contact resistances R_{cont} between the Wollaston wire and the NW, and between the NW and the cold sink, lead directly to errors in the calculated $R_{th,NW}$ [Fig. 5-1(b)]. That is,

$$R_{th,NW,apparent} = R_{th,NW} + R_{cont,Woll-NW} + R_{cont,NW-cold\ sink} \qquad (5\text{-}35)$$

As a first approximation, the expected magnitude of these contact resistances can be estimated from

$$R_{cont} \approx 1/hA_{cont} \qquad (5\text{-}36)$$

where A is the contact area and h_{cont} is the specific contact conductance. This expression assumes a one-dimensional geometry at the contact. Because this assumption may be violated in the current experiment, spreading resistance effects are discussed below. Cahill *et al.* [14] report that typical values of h_{cont} at 300 K range from about 30 - 800 MW/m^{2}K for various material combinations. For a 10 nm diameter NW contacted at the end, $A\approx80$ nm^2, and so R_{cont} might be expected to range from 2 x 10^7 to 4 x 10^8 K/W.

These resistances are comparable to or larger than the expected $R_{th,NW}$, and thus would be a serious experimental obstacle to quantitative measurements of $R_{th,NW}$. The contact resistances may be reduced greatly by increasing the effective contact area. For example, if the same NW can be contacted around its circumference over the last 200 nm of its length, the contact area would become 6300 nm^2, reducing the contact resistance by a factor of 80 to the more acceptable neighborhood of 3×10^5 to 5×10^6 K/W.

Because the contact region is much smaller than the diameter of the Wollaston wire, spreading resistance effects within the Wollaston wire and within the gold STM probe must also be considered. The magnitude of the thermal spreading resistance can be estimated from the conduction shape factor for a disc-shaped contact of diameter D on a semi-infinite substrate [15]:

$$R_{spreading} \approx 1/(2k_{Subs}D) \tag{5-37}$$

where k_{Subs} is the thermal conductivity of the substrate, in this case the Wollaston wire. The semi-infinite substrate assumption is justified because the diameter of the Wollaston wire is more than 5 times larger than the diameter of the contact area. Assuming a platinum Wollaston wire, the spreading resistance portion of the contact resistance is estimated as 7×10^5 K/W for a 10 nm diameter contact. Again, if the area of the contact is increased, the spreading resistance will be reduced. In some cases the size of the contact area may be comparable to or even smaller than the mean free path of the electrons in the Wollaston wire. In this situation the so-called "phonon rarefaction" effect becomes important, and the spreading resistance will increase compared to the ideal calculation of Eq. (5-37) [16].

5.3.5 Radiation corrections

The analysis of Eqs. (5-1) - (5-18) neglected radiation losses from the Wollaston wire. To check this assumption we model the Wollaston wire as a fin, and incorporate the radiation losses through a radiation convection coefficient,

$$h_{rad} = 4\varepsilon_{rad}\sigma_{SB}T^3 \tag{5-38}$$

where ε_{rad} is the emissivity of the Wollaston wire (assumed, conservatively, to exist in black surroundings), σ_{SB} the Stefan-Boltzmann constant (5.67×10^{-8} W/m^{2}K^4), and T the mean absolute temperature of the Wollaston wire and its surroundings. For shiny metals such as platinum at 300 K, the emissivity typically ranges from 0.02 to 0.1 [15], and so for typical experiments:

$$0.1 < h_{rad} < 0.6 \text{ W/m}^2\text{K}. \tag{5-39}$$

From traditional fin analysis [15], we know that radiation/convection losses can generally be neglected if the fin half-length is short compared to the characteristic length β^{-1}, where β is the fin parameter:

$$\beta^{-1} = \sqrt{\frac{kD}{4h_{rad}}} \tag{5-40}$$

For a typical platinum Wollaston wire of 3 μm diameter, this length is about 9 - 23 mm. Because this is much longer than the typical Wollaston wire half-length of about 1 mm, we can expect that radiation losses will be a very small correction.

To proceed further and quantify these potential errors from radiation losses, we can include the radiation/convection term in the original heat equation:

$$\frac{1}{\beta^2}\frac{d^2\theta_x}{dx^2} = -\frac{QD}{4h_{rad}} + \theta_x \tag{5-41}$$

where $Q=I^2R_{e0}/SL$. The boundary conditions at $x=0$ and $x=\pm L/2$ are unchanged from Eqs. (5-2) and (5-3). Radiation losses will be most important when there is no heat loss through a nanowire, that is, when $\gamma=0$, so to be conservative (and simple) we focus on that limit here. The solution of Eqs. (5-2), (5-3), and (5-41) is

$$\theta_x(x, h_{rad}, \gamma = 0) = \frac{QD}{4h_{rad}}\left(1 - \frac{\cosh(\beta x)}{\cosh(\beta L/2)}\right) \tag{5-42}$$

The average temperature is then

$$\theta_{avg}(h_{rad}, \gamma = 0) = \frac{QL^2}{4k(\beta L/2)^3}\left[\frac{\beta L}{2} - \tanh\left(\frac{\beta L}{2}\right)\right]. \tag{5-43}$$

By performing a Taylor series expansion for small h_{rad} (that is, small β), it is readily verified these two expressions give the correct limiting behavior in the absence of radiation [(Eqs. (5-4) and (5-7) with $\gamma=0$]. The fractional error in the estimated temperature can be expressed as

$$\textit{fractional error in } \theta_{avg} = \frac{\theta_{avg,neglect\ radiation} - \theta_{avg,include\ radiation}}{\theta_{avg,include\ radiation}} \tag{5-44}$$

which, considering Eqs. (5-7) and (5-43) turns out to be

$$\begin{aligned} \textit{fractional error in } \theta_{avg} &= \frac{(\beta L/2)^3}{3[(\beta L/2) - \tanh(\beta L/2)]} - 1 \\ &\approx \frac{2}{5}(\beta L/2)^2 \qquad (\text{for } \beta L < 5) \end{aligned} \tag{5-45}$$

where in the second step we have performed a Taylor series expansion for small βL. Thus, to keep the error in temperature measurements less than 10%, it is necessary to keep $\beta L/2 < 1/2$, or simply $\beta L<1$. For the 3 μm x 2 mm Wollaston wire discussed previously, $\beta L/2$ ranges from 0.043 to 0.11, so the fractional error is expected to be between 0.073% and 0.48%. Clearly, radiation errors should be negligible for this type of Wollaston wire.

However, in order to measure NW of very high thermal resistance, a more sensitive Wollaston wire probe might be fabricated with a diameter of 0.5 μm and a length of 5 mm, made out of PtRh with a lower thermal conductivity of 38 W/mK ($R_{th,Woll}$=6 x 10^8 K/W, see Fig. 5-2). In this case, for an emissivity of 0.02 to 0.1, $\beta L/2$ would range from 0.36 to 0.89, resulting in temperature errors between 5.2% and 32%.

Thus, we can conclude that radiation corrections at 300 K are negligible for the standard 3 μm x 2 mm Wollaston wires, may become significant for the most sensitive Wollaston wires, but should not be overwhelming. There is tradeoff when optimizing the thermal design of the Wollaston wire for negligible radiation losses compared to sensitive measurements of $R_{th,NW}$. This is clearly seen by expressing $\beta L/2$ in terms of $R_{th,Woll}$ and eliminating L:

$$\frac{\beta L}{2}=\frac{\pi}{2}R_{th,Woll}\sqrt{hkD^3}\,. \tag{5-46}$$

$R_{th,Woll}$ is already constrained by the thermal matching with the expected NW thermal resistance. For radiation considerations we would like to keep $\beta L/2 < 0.5$. Eq. (5-46) shows that we should do this by choosing Wollaston wire materials with small h_{rad}, and, less obviously, small k. Furthermore, we should choose small diameter Wollaston wires, which also means that they will be shorter (because we should hold constant $R_{th,Woll} \propto L/D^2$)

5.3.6 Mechanical aspects of probe design

Although the thermal calculations above show that a Wollaston-wire thermal probe should be able to measure the thermal resistance of individual NWs, the mechanical design of the Wollaston wire probe also requires some care.

The need for pretensioning

The thermal design described above assumes that the Wollaston wire is rigidly fixed throughout the experiment. However, in practice there are three effects which tend to make the Wollaston wire move: thermal expansion, thermal vibrations due to fundamental thermodynamics, and, when deployed inside the TEM, Lorentz forces. A good solution to overcome these mechanical stability issues is to pretension the Wollaston wire. Additional challenges of the high-vacuum, high-magnetic field TEM environment are described later.

Thermal expansion

The coefficient of thermal expansion (CTE) of Pt is about 9 x 10^{-6} K^{-1} (9 parts-per-million per K, ppm/K) and the CTE of PtRh alloy is likely about double this value. For a Wollaston wire of length L=2 mm and a temperature rise of $\theta \approx 10$ K, the change in length would be about $\delta L \approx 180$ nm if only one end were fixed:

$$\delta L = (\mathrm{CTE}) \cdot L\theta \tag{5-47}$$

However, because both ends are fixed, this will cause a lateral shift of much larger deflection. This lateral shift can be estimated from Euler-Bernoulli beam theory for a buckled column [17]. For a perfect column whose ends are constrained to not rotate (i.e. fixed-fixed boundary conditions), the deformed beam will have a shape

$$y(x) = \tfrac{1}{2} y_0 (1 + \cos(2\pi x / L)). \tag{5-48}$$

as shown in Fig. 5-7(a). Note that the maximum lateral deflection is denoted y_0, and occurs at x=0. The total arc length, λ, of a curved beam is given by

$$\lambda = \int_{-L/2}^{+L/2} \sqrt{\left(\frac{dy}{dx}\right)^2 + 1}\ dx \tag{5-49}$$

which for small deflections simplifies to

$$\lambda \approx \int_{-L/2}^{+L/2} 1 + \tfrac{1}{2}\left(\frac{dy}{dx}\right)^2\ dx \tag{5-50}$$

For the profile given in Eq. (5-48), the resulting arc length is

$$\lambda \approx L\left[1 + \left(\frac{\pi y_0}{2L}\right)^2\right] \tag{5-51}$$

so we can equate

$$\frac{\delta L}{L} \approx \left(\frac{\pi y_0}{2L}\right)^2 \tag{5-52}$$

Thus,

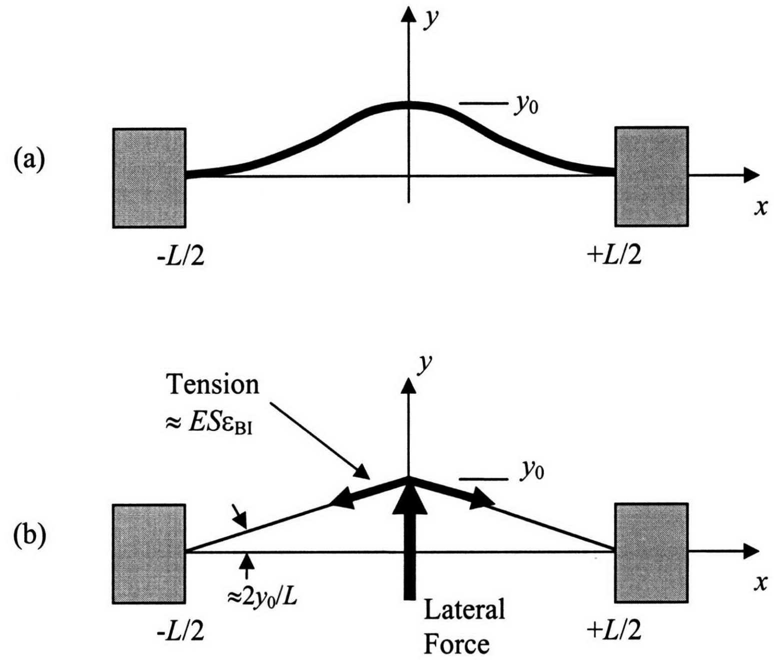

Figure 5-7. Mechanical issues in the design of a Wollaston wire probe. (a) Lateral buckling due to thermal expansion. (b) Force balance to determine an approximate, effective spring constant for lateral deflections.

$$y_0 \approx \frac{2L}{\pi}\sqrt{\frac{\delta L}{L}} \tag{5-53}$$

For the typical Pt Wollaston wire example described here, the lateral deflection of $y_0 \approx 12$ μm is more than 60 times larger than the axial elongation of $\delta L \approx 180$ nm. Lateral and longitudinal deflections of the Wollaston wire may be acceptable if they are small compared to the length of the NW. Because typical NWs are only about 0.5 - 5 μm long, a lateral deflection of 12 μm would pose serious challenges. Fortunately, it is easy to avoid this problem by pretensioning the Wollaston wire by more than the anticipated thermal δL. For a wire in tension, the built-in stretch δL_{BI} is given by

$$\delta L_{BI} = L\varepsilon_{BI} = L\sigma_{BI}/E, \tag{5-54}$$

where ε_{BI} is the built-in strain, σ_{BI} is the built-in stress, and E is the Young's modulus of the Wollaston wire. As long as the built-in strain exceeds the thermal expansion strain, ε_{TE}=(CTE)θ, the wire will remain in tension rather than buckling, and there should ideally be no deflections in either the lateral or longitudinal directions. For the representative example considered here, the requirement becomes $\varepsilon_{BI} > 9$

x $10^{-5} \approx 0.01\%$. Because of the small cross-sectional area S of the Wollaston wire, this strain corresponds to a fairly small force:

$$F_{BI} = S\sigma_{BI} = SE\varepsilon_{BI} \, . \tag{5-55}$$

For example, the common 3 μm diameter Pt Wollaston wire requires only about 100 μN of force to achieve 0.01% of built-in strain. This force is equivalent to the weight of a 10 mg mass, which suggests one practical approach to pretensioning. First, one end of the Wollaston wire is anchored to the supporting frame with epoxy, and a 10 mg mass is attached to the other end of the Wollaston wire. Next, the frame and Wollaston wire assembly are tilted 90 degrees to orient the Wollaston wire vertically, with the etched portion of the Wollaston wire supporting the weight of the mass. At this stage the epoxy joint is uppermost. Then, a second small droplet of epoxy is applied to the lower support of the frame, anchoring the Wollaston wire. Finally, after the second epoxy joint has hardened, the mass can be removed, transferring the load to the epoxy joint.

This deadweight approach has been used to successfully pretension 3 μm Wollaston wires, using masses that typically range from 10-30 mg. The quality of pretensioning can be observed experimentally by noting the relationship between the lateral deflection and applied temperature at the Wollaston wire, in the absence of any NW. For a poorly-tensioned 3 μm diameter Wollaston wire, typical lateral deflections are about 50 - 100 nm/K, while the best-tensioned Wollaston wires made so far have deflections of about 2 - 5 nm/K.

Fundamental thermal vibrations

It is well-known that a simple spring-mass system at finite temperature exhibits small random fluctuations in position, due to the thermal population of the vibrational modes. This is analogous to Johnson noise in a resistor. An intuitive understanding comes from equating the thermal energy, $k_B T$, to the sum of kinetic and potential energies. From equipartition of energy [18], we know that the average values of kinetic and potential energies are the same, so this condition becomes

$$\tfrac{1}{2} g y_{Th}^2 \approx \tfrac{1}{2} k_B T \, , \tag{5-56}$$

where g is the spring constant and y_{Th} is the average thermal displacement. Thus, a rough estimate for y_{Th} is

$$y_{Th} \approx \sqrt{\frac{k_B T}{g}} \, . \tag{5-57}$$

Notice that this result is independent of the mass attached to the spring.

A more sophisticated analysis has been used by Treacy *et al.* [19] to estimate the stiffness of a single carbon NT from its vibrations under a TEM, and is described in detail by Krishnan *et al.* [20]. The analysis can be presented briefly in terms of conditional probabilities. For example, $P(y|T)$ is the probability that the oscillator will be found at a location y, given that it is in a bath of temperature T. This can be expressed as an integral over energy,

$$P(y\,|\,T) = \int_{\varepsilon} P(y\,|\,\varepsilon) P(\varepsilon\,|\,T) d\varepsilon \tag{5-58}$$

where $P(\varepsilon|T)$ is the probability of the oscillator having energy ε, given that it is in a bath of temperature T. This probability is found from the Boltzmann factor [18],

$$P(\varepsilon\,|\,T) d\varepsilon = \frac{1}{k_B T} \exp\left(-\frac{\varepsilon}{k_B T}\right) d\varepsilon \,. \tag{5-59}$$

Also in Eq. (5-58), $P(y|\varepsilon)$ is the probability of finding the oscillator at location y, given that it has a total energy ε. This probability is found from the kinematics of simple harmonic motion,

$$P(y\,|\,\varepsilon) dy = \frac{1}{\pi \sqrt{\dfrac{2\varepsilon}{g} - y^2}} dy \tag{5-60}$$

Combining Eqs. (5-58) - (5-60) leads to a Gaussian probability distribution,

$$P(y\,|\,T) = \frac{1}{\sqrt{2\pi}\,\sigma_{Th}} \exp\left(-\frac{y^2}{2\sigma_{Th}{}^2}\right) \tag{5-61}$$

where the thermal standard deviation σ_{Th} is

$$\sigma_{Th} = \sqrt{\frac{k_B T}{g}} \,, \tag{5-62}$$

identical to the simplistic estimate of Eq. (5-57).

Thus, to ensure that the thermal vibrations are negligibly small, the effective spring constant of the Wollaston wire must be sufficiently large, regardless of its mass. For example, to keep vibrations below 100 nm, g must be greater than 0.4 μN/m, while to keep vibrations below 1 nm, g must exceed 4 mN/m. What is the effective lumped spring constant of a pretensioned Wollaston wire for these lateral thermal vibrations? Although the methods of Krishnan *et al.* [20] could be used to develop a rigorous answer in terms of the normal modes of the Wollaston wire, here we will be content with a rougher estimate. As a first approximation, assume that the profile of the fundamental mode is triangular rather than sinusoidal [Fig. 5-7(b)], and consider the response to a point force applied at the Wollaston wire midpoint. Because the additional strains due to deflection will be far smaller than the built-in strain due to pretensioning, to a very good approximation the tension in the Wollaston wire will remain constant during deflections. From a simple force balance, the spring constant is found to be

$$g \approx 4ES\varepsilon_{BI} / L \tag{5-63}$$

Although Eq. (5-63) shows that decreasing L or increasing S improves the mechanical performance of the Wollaston wire probe, this would be bad for the thermal performance of the probe because it would reduce the thermal resistance of the Wollaston wire, $R_{th,Woll}=L/kS$. It is better to express the spring constant in terms of thermal parameters,

$$g \approx \frac{4E\varepsilon_{BI}}{k\,R_{th,Woll}} \tag{5-64}$$

This shows that geometric factors have canceled out. Assuming that $R_{th,Woll}$ is already fixed by the thermal requirements, Eq. (5-64) shows that to achieve good mechanical performance, a Wollaston wire material should have large Young's modulus, low thermal conductivity, and tolerate a large built-in strain. For Pt, the quantity $E\varepsilon_{max}/k$ is approximately 7 x 10^5 (N/m)/(K/W). Thus, to keep σ_{Th} less than 1 nm (requiring g greater than 4 mN/m), $R_{th,Woll}$ is restricted to be smaller than about 2 x 10^8 K/W. Fortunately, this upper limit on $R_{th,Woll}$ is still large enough to permit accurate measurements of a wide range of NW and NT, as shown in Fig. 5-2.

Additional mechanical issues when used inside a TEM

Designing a Wollaston probe to work inside a TEM brings three additional challenges. First, a standard TEM sample holder only allows a very small volume in which to add the Wollaston probe. The allowed volume is approximately (5 mm) x (3 mm) x (1.5 mm), which must include clearances to avoid colliding with the sample holder, or worse, one of the TEM lenses. A second issue is that the TEM operates at a base pressure of typically 1.5 x 10^{-5} Pa (~10^{-7} torr or mbar). Thus all materials of the Wollaston probe must be compatible with high-vacuum conditions, ruling out certain polymers and epoxies. The third challenge is the very high magnetic fields present near the final lens of the TEM, of the order of 0.1 - 1 Tesla. This requires that the Wollaston probe be free of all magnetic materials, which could be torn off of the sample holder and collide with a lens. A related concern is the Lorentz forces exerted on a Wollaston wire. Experience has shown that a Wollaston wire with good pretension is not affected by Lorentz forces as long as the TEM lens is in low-magnification mode, but in the high-magnification mode, the Lorentz forces are strong enough to destroy the Wollaston wire if any current is flowing. Thus, as a precaution the Wollaston wire is short circuited to itself whenever the TEM is operated in the high-magnification mode.

5.4 Thermal resistance measurements using the Wollaston wire probe

5.4.1 Experimental procedure to measure thermal conductivity

Mounting the Wollaston probe, powder source, and sample

The first step in preparing for a Wollaston wire measurement inside the TEM (Fig. 5-4) is to mount the Wollaston probe, sample, and powder source for in-situ contact deposition (described later). First, the wire supporting the powder source is soldered to part of the TEM sample holder frame. This is primarily for mechanical support, although there may also be some benefit in grounding the powder source in order to prevent charging effects. Next the powder source is gently filled with precursor powder. Then, the gold wire attached to the Wollaston wire probe is inserted into its cylindrical sleeve at the far end of the sample holder frame. The two leads from the probe are carefully soldered to the appropriate electrodes on the frame. Excess heating from the soldering iron appeared to result in loss of pretension in the Wollaston wire in several trials, especially when the Wollaston wire was mounted on a quartz substrate thinner than the usual 500 μm. Finally, the sample itself is mounted. The sample consists of a single NW that was previously attached to the sharp end of a gold wire. In most cases the gold wire has already been etched down to a very sharp point for use as a scanning tunneling microscope (STM) tip, but adequate results may also be possible simply by using scissors to cut a sharp end on gold wire. This gold probe wire is then attached to the xyz piezoelectric manipulator that is built in to this TEM holder.

Instrumentation

The existing TEM sample holder has 4 auxiliary electrodes in addition to the electrode on the STM tip. This would permit 4-point electrical measurements of the Wollaston wire, but for simplicity in the current experiments we limit ourselves to 2 point measurements. The typical lead resistances are several ohms, which represents an important correction for some of the Wollaston wires, whose resistances range from about 30 - 300 Ω depending on material and geometry. A homemade cable and breakout box are used to access the necessary electrical leads for our measurements, but by setting the appropriate switches, full control can be reverted to the manufacturer's hardware.

The basic circuit used for Wollaston wire thermal measurements is depicted in Fig. 5-8(a). An AC voltage source, such as the reference signal from a lock-in amplifier, is used to drive the circuit. A ballast resistance, typically 1000 Ω, is often used so that the voltage source behaves like a current source. A lock-in amplifier is used to measure the resulting voltage drop across the Wollaston wire, including the effects of lead resistances. Finally, for precise current measurements, an optional second lock-in amplifier can be used to measure the voltage drop across a 10.00 Ω standard resistor. Alternatively, the current can be estimated from the magnitude of the source voltage and an estimate for the total resistance of the circuit. For experiments where the total circuit resistance is dominated by the well-known ballast resistance, this should be a good estimate. The experiment is most conveniently performed at frequencies slower than the characteristic longitudinal diffusion frequency of the Wollaston wire. For example, operating at 0.5 Hz for the typical 2 mm long Wollaston wire ensures the low-frequency limiting behavior of Eq. (5-12). On the other hand, the high frequency limit of Eq. (5-13) is also sometimes useful. For example, operating at 102 kHz (the limit of our SR830 lock-in amplifier) is much faster than the mechanical resonance of the Wollaston wire, ensuring that there is very little lateral displacement due to Lorentz forces. This is particularly important in the high magnification mode, because the local magnetic fields seem to be much stronger and could easily cause a Wollaston wire to go slack.

Checking the mechanical stability

After inserting the sample holder into the TEM and reaching base pressure, a few preliminary checks are in order prior to beginning thermal experiments. The most important issue is to confirm that the Wollaston wire retains adequate pretension. To check this, the magnitude of the thermally-driven displacement can be estimated. Several values of drive voltage are set, covering the expected range of the experiment. For each drive voltage, the peak-to-peak lateral displacement of the Wollaston wire is estimated by observing it in the low-magnification mode of the TEM. The average temperature rise can be estimated from the guideline of Eq. (5-25). A plot of displacement versus temperature yields an estimate for a thermal displacement coefficient in units of nm/K. Experience has shown that the best Wollaston wire probes so far respond at about 5 nm/K, while bad probes exhibit thermal expansion of around 100 nm/K or worse.

If the thermal expansion is adequately small, it is also appropriate to check for thermal vibrations at very high magnification. This should be done with zero current and the Wollaston wire shorted to itself for additional security. In a slack Wollaston wire it is impossible to image the Wollaston wire at high resolution, not only due to its thermal vibrations but also because the focal spot of the electron beam tends to "push" the Wollaston wire around when the beam is focused near the wire. The origin of this lateral force is unclear. However, we believe the displacement is real, and not some artifact of the electron

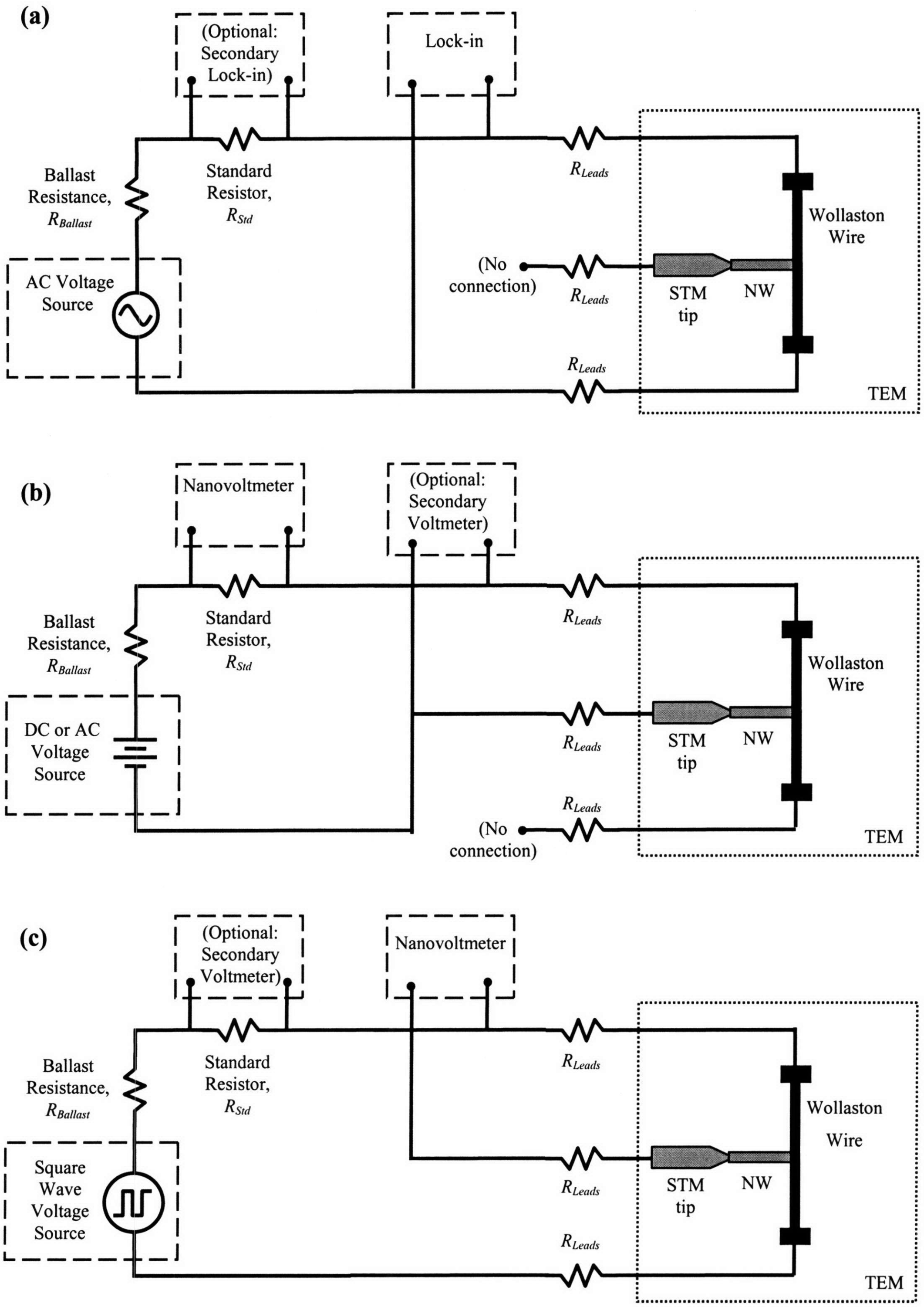

Figure 5-8. Circuit diagrams for measuring the thermoelectric properties of a single nanowire with a Wollaston wire probe inside a TEM. (a) Thermal resistance of the NW. (b) Electrical resistance of the NW. (c) Seebeck coefficient of the NW. By using knowledge of the source voltage and assuming that the electrical resistances obey $R_{NW} >> R_{Ballast} >> R_{Woll}$, the optional secondary equipment can be omitted (see text).

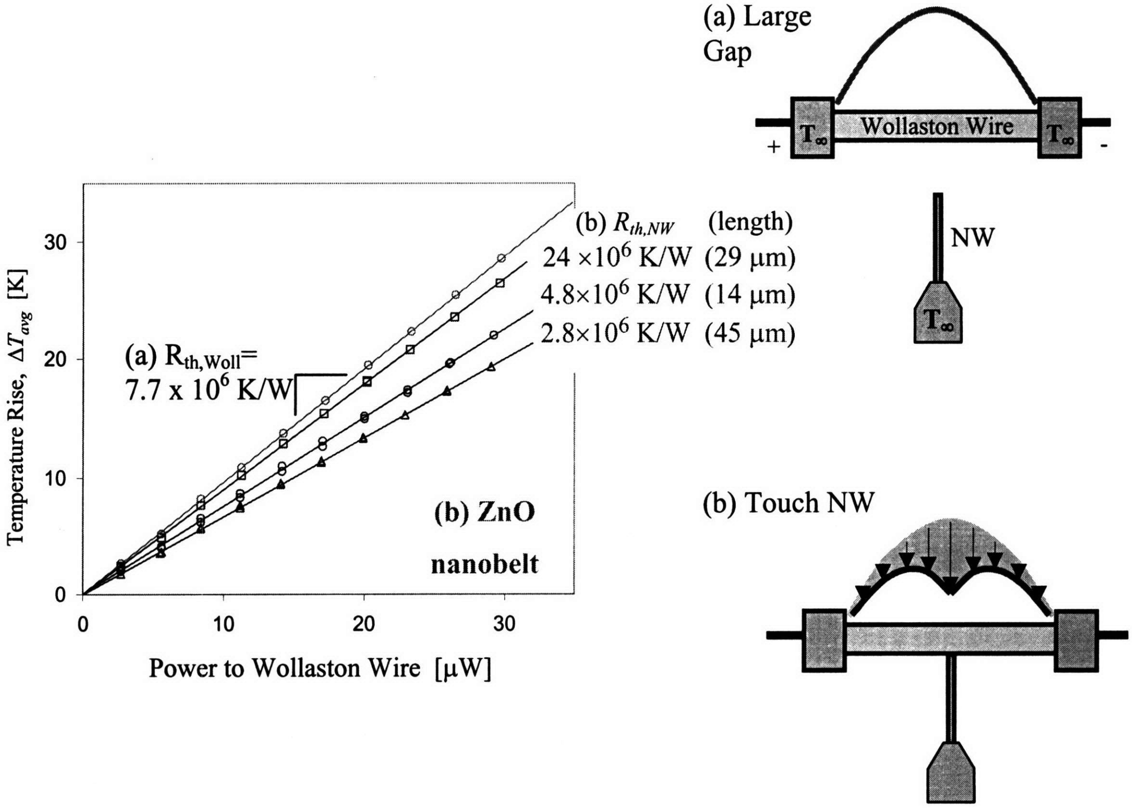

Figure 5-9. Preliminary thermal measurements of a ZnO nanobelt using a Wollaston wire probe inside a TEM. (a) Baseline thermal response of a bare Wollaston wire. (b) Preliminary thermal resistance data for an individual ZnO nanobelt. The three curves correspond to three different trials with different lengths of the same nanobelt, and show that the non-repeatable contact resistance dominates the measurement.

optics, because in these situations the Wollaston wire is "pushed" around even though an adjacent rigid feature such as the STM tip remains fixed.

5.4.2 Preliminary measurements of thermal conductivity

Representative preliminary data are shown in Fig. 5-9 for measurements of the thermal conductance of a ZnO nanobelt using a 3 μm diameter Wollaston wire. First the bare Wollaston wire is calibrated by itself (uppermost line). Several driving currents were chosen to give a temperature rise of up to approximately 25 K. By measuring the changes in electrical resistance and dividing by the temperature coefficient of resistivity, the average temperature rise of the Wollaston wire was determined. The slope of temperature versus power input gives the thermal resistance of the Wollaston wire according to Eq. (5-14),

$$R_{th,Woll} = 8\left(\frac{\partial\theta}{\partial Q_{avg}}\right)_{no\ NW,\ \omega\to 0} \tag{5-65}$$

while in the high frequency limit the factor of 8 should be replaced by 12.

Next a ZnO nanobelt of ~3 μm width but uncertain thickness (very likely < 100 nm) was brought into contact with the Wollaston wire. In contrast to the usual configuration of end contact, here it was the side of the nanobelt that was contacted to the Wollaston wire by bringing the belt down from above. With the belt in contact a new θ-Q curve was measured. The slope of the new curve was normalized by the slope of the uncontacted Wollaston wire θ-Q curve to calculate ϕ from Eq. (5-15), and then finally the thermal resistance of the nanobelt was estimated from Eq. (5-17) or (5-18).

Because no special measures were taken to improve the quality of the thermal contacts in this set of experiments, the results were not repeatable when the contact was broken and remade. The middle curve corresponds to an approximately 14 μm length of ZnO, with a calculated thermal resistance (including contacts) of 4.8×10^6 K/W. The curve above corresponds to doubling the length of nanobelt to about 29 μm, but the calculated thermal resistance increased by about a factor of 5, to 2.4×10^7 K/W. However, the lowermost curve corresponds to an even *longer* length of about 45 μm, but has the *lowest* thermal resistance of 2.8×10^6 K/W. These data show that the contact resistances must be the dominant contribution to the total thermal resistance, and vary greatly from trial to trial whenever the nanobelt was removed and then replaced on the Wollaston wire. Clearly, the thermal contact resistance must be improved.

5.5 Electrical conductance measurements using the Wollaston wire probe

5.5.1 Experimental procedure to measure electrical conductivity

The same "T" shaped configuration used to measure the thermal conductance of a NW can also be used to measure its electrical conductance. The electrical measurement is considerably simpler than the thermal measurement. As shown in Fig. 5-8(b), a DC or AC current is passed in one end of the Wollaston wire, through the NW, and then out from the cold sink. The current may be measured with an ammeter, or determined from the voltage drop across the 10.00 Ω standard resistor. Because the electrical resistance of a single NW is expected to be tens of kΩ if not much larger, the resistance of the rest of the circuit can often be neglected in comparison to the resistance of the NW. In this limit the voltage across the nanowire is taken to be the same as the voltage of the DC or AC source. This

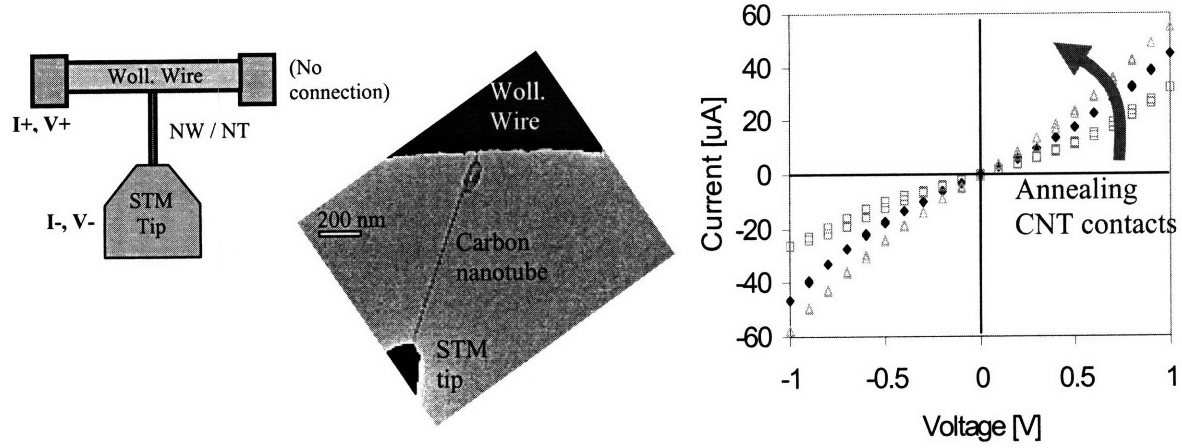

Figure 5-10. Preliminary electrical measurements of a carbon nanotube using a Wollaston wire probe inside a TEM. Further annealing of the carbon nanotube contacts results in linear *IV* curves (not shown).

assumption is easily checked for self-consistency in any data set and turns out to be appropriate for our measurements so far. Of course, it would be better to use a second voltmeter to measure the voltage across the NW directly.

5.5.2 Preliminary measurements of electrical conductivity

Representative *I-V* curves for a carbon nanotube with carbon contacts are shown in Fig. 5-10. The technique to deposit amorphous carbon is described in the next section. It is clear that the IV curves of Fig. 5-10 are nonlinear but fairly symmetric. This is due to the poor electrical properties of the amorphous carbon contacts. The amorphous carbon can be partially graphitized, and its electrical properties improved, by passing a relatively large annealing current (of the order of 100 μA) through the CNT for several minutes [22]. This is the reason for the three different curves of Fig. 5-10: they correspond to successive attempts at annealing. Although not shown here, further annealing is known to reliably result in ohmic *I-V* curves for these CNT with amorphous carbon contacts [22].

5.6 Seebeck measurements using the Wollaston wire probe

Calculations of the Seebeck coefficient require measurements of both the voltage and temperature differences across the NW. In conventional macro-scale experiments this is readily achieved with separate temperature probes and voltage probes at each end of a sample. However, for single-NW measurements it would be very difficult to make more than one contact at each end of the NW. Shi *et al.*

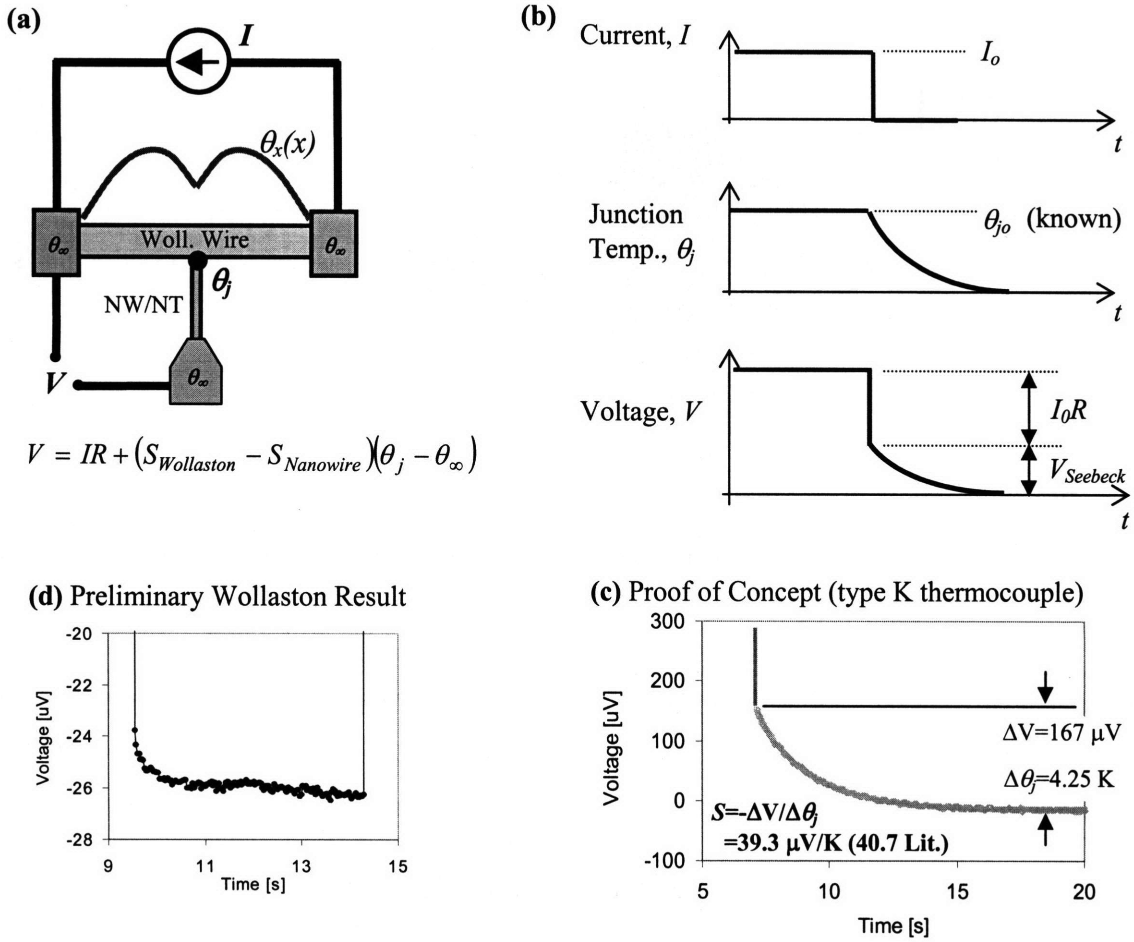

Figure 5-11. Preliminary Seebeck measurements using a Wollaston wire probe. (a) Measurement circuit. (b) Evolution of current, junction temperature, and voltage when the current is suddenly turned off. (c) Proof-of-concept data taken in a benchtop experiment for a millimeter-scale thermocouple (type K: chromel-alumel). (d) Preliminary data for a single carbon nanotube taken with the Wollaston wire probe. Although the decay signal is clearly resolved, the Seebeck coefficient cannot be estimated quantitatively because of the large thermal contact resistance.

[2] addressed this problem by microfabricating a heater/thermometer and a voltage probe at the platforms on either end of the NW, with a total of 10 electrical leads.

The Wollaston wire probe used in this work (Fig. 5-4) includes only 3 electrical leads and is simpler than the Shi *et al.* system. However, with some additional assumptions, the Seebeck coefficient can still be measured by a technique similar to Harman's method [21]. A key concept is that each measurement is a sequence of two steps, and so by multiplexing the measurement in time we can essentially double the functionality of the leads.

In the first step, a NW is touched to the midpoint of the Wollaston wire and a DC current is passed through the Wollaston wire [Figs 5-11(a,b)]. From the thermal analysis described above (Eq. 5-4), the temperature θ_{j0} at the NW-Wollaston wire junction is

$$\theta_{j0}(\gamma) = \left(\frac{I^2 R_{e0} L}{8kS}\right)\left(1 - \frac{1}{1+\gamma^{-1}}\right). \tag{5-66}$$

where all quantities on the right-hand side are known from calibration and earlier measurements. This NW-Wollaston wire junction is also one junction of a thermocouple formed between the Wollaston wire and the NW. The voltage ΔV measured between the STM tip and either end of the Wollaston wire contains both an Ohmic term and a Seebeck voltage:

$$\Delta V = \tfrac{1}{2} I R_{e0} + \left(\theta_{j0} - \theta_\infty\right)\left(S_{Woll} - S_{NW}\right) \tag{5-67}$$

where θ_∞ is the temperature of the surrounding environment, including the STM and the ends of the Wollaston wire.

In the second step, the electrical current is set to zero. Now the voltage difference decays according to

$$\Delta V(t) = \left(\theta_j(t) - \theta_\infty\right)\left(S_{Woll} - S_{NW}\right). \tag{5-68}$$

As the heat flows out of the Wollaston wire, the temperature difference $\left(\theta_j - \theta_\infty\right)$ decays to zero in an approximately exponential fashion. Importantly, the timescale of this decay is determined by the thermal diffusion time along the *length* of the *Wollaston wire* [Eq. (5-8)], and *not* by the diameter of the Wollaston wire or length of the nanowire. For a typical Wollaston wire probe made from platinum and 2 mm long, $\tau \approx 160$ ms. This is slow enough that the transient can be measured with reasonable accuracy, using, for example, a nanovoltmeter. In principle the microfabricated "T" platform of Fujii *et al.* could also measure the Seebeck coefficient using this technique, but would require much faster instrumentation because the thermal diffusion time for a 6 μm long Pt heater is only around 1 μs. Although Eq. (5-68) could be combined with a solution of the transient heat conduction equation to fit the entire voltage transient, it is simpler to measure only the magnitude of the voltage decay:

$$\Delta V_{trans} = \left(\theta_{j0} - \theta_\infty\right)\left(S_{Woll} - S_{NW}\right) \tag{5-69}$$

Assuming that the Seebeck coefficient of the Wollaston wire is known (from handbook values or previous calibration), the only unknown is the NW Seebeck coefficient.

This technique, which has not been reported previously, depends on several assumptions and has several limitations. The greatest difficulty is that good thermal and electrical contacts are required for quantitative measurements. In addition, previous measurements or estimates of γ are necessary, though this method actually works better in the common limit of large $R_{th,NW}$ because θ_{j0} becomes independent of γ for γ<<1. The duration of the transient decay is brief enough that some care is necessary in the instrumentation, though this is not a major problem.

5.6.1 Experimental procedure to measure Seebeck coefficient

The circuit of Fig. 5-8(c) can be used to measure the Seebeck coefficient of a NW. A function generator is used to generate a square wave with DC offset equal to the amplitude. Thus, the current is some constant I_0 during the first half of the period, and zero during the second half of the period. The period is typically around 10-20 s, chosen to be much longer than the thermal decay time τ. The nanovoltmeter monitors the voltage between the STM/cold sink and one end of the Wollaston wire, as described in Eq. (5-67). A program was written in Labview to average many transients of the nanovoltmeter data and obtain time resolution as fine as approximately 10 ms.

5.6.2 Preliminary measurements of Seebeck coefficient

Because this is a new technique, to prove the concept a benchtop experiment was performed using macro-sized type-K thermocouple wire. The voltage decay curve is shown in Fig. 5-11(c). It is important to measure the voltage decay to whatever the constant asymptote value is, even if this is not actually zero. Non-zero asymptotes are most likely due to static thermoelectric voltages elsewhere in the circuit, and as such only add a constant offset term to the analysis of Eqs. (5-67) - (5-69). Non-zero asymptotes would also occur if the function generator voltage at "zero" has an offset. Because the heating is proportional to the square of this off-state current, small residual currents will have a negligible impact on the off-state temperature. This argument has been confirmed experimentally for several values of the off-state current. For the data shown in Fig. 5-11(c), the magnitude of the voltage decay is 167 μV. The thermal analysis described above was used to estimate the corresponding temperature decay of the junction as $(\theta_{j0}-\theta_{\infty})=4.25$ K. The implied Seebeck coefficient is then 39.2 μV/K, which is within 4% of the nominal value of 40.7 μV/K, validating the basic approach.

A preliminary attempt to measure the Seebeck coefficient of a CNT is shown in Fig. 5-11(d). The voltage and temperature decay is only about 2 μV over about 1 second, but is still resolved adequately by the nanovoltmeter. However, these data cannot be interpreted quantitatively because this experiment had a large thermal contact resistance, and so we do not know how much of the measured temperature drop occured across the CNT and how much across the contact resistance.

5.7 Improving the thermal contact resistance through electron-beam induced deposition (EBID)

The above discussion has shown that poor electrical and thermal contacts are a great challenge to quantitative thermoelectric measurements of individual NWs. NW measurement schemes that place a NW in contact with a prefabricated metal contact, such as the Shi *et al.* and Fujii *et al.* platforms and the Wollaston wire probe described in this chapter, are likely to have large electrical and thermal contact resistances unless special care is taken. To reduce these resistances, it is common to deposit additional material around the two endpoints of the NW where it meets the contacts. This is usually achieved by local chemical vapor deposition (CVD), where a focused beam of energy (ions, electrons, or photons) induces vapors of a precursor molecule to deposit locally as a solid. When the energy source is ions, the process is known as focused ion beam (FIB) deposition. When the energy source is electrons, the process is commonly known as electron-beam induced deposition (EBID). A laser beam can also be used. Because many single-NW experiments involve some fabrication steps inside an SEM and/or TEM, EBID is a natural choice for local CVD because the electron beam is already present. FIB deposition, on the other hand, requires additional hardware. In this thesis, EBID was implemented in the high-resolution TEM at Boston College. Although amorphous carbon was deposited in the preliminary experiments, this was found to give unreliable contacts, and so subsequent work focused on EBID of tungsten.

5.7.1 EBID of carbon

The vacuum chambers used in SEM and TEM often contain significant levels of residual organic vapors even at the operating pressures of $\sim 10^{-5}$ - 10^{-3} Pa ($\sim 10^{-7}$ - 10^{-5} torr or mbar). These organics are a natural precursor for the simplest form of EBID, the local deposition of amorphous carbon. This is the first form of contact improvement implemented by Shi *et al.*, and is still in use [1-6]. However, our attempts at EBID of carbon inside the TEM met with mixed results. The greatest problem was that the carbon deposition rate varied greatly from trial to trial. In some cases the deposition rate was virtually zero, while in other cases the deposition was very fast (several nm/s). Sometimes a faster deposition rate could be elicited by applying a small drop of alcohol near the sample immediately prior to inserting it into the TEM vacuum chamber, but even this technique would often fail to lead to carbon deposition. Another problem is that the carbon was amorphous and often resulted in nonlinear I-V curves with very high resistivity. Previous experience from the Boston College group showed that such amorphous carbon deposits could often be "annealed" by passing an electrical current [22]. This treatment commonly resulted in linear *I-V* curves, much lower electrical resistance, and a graphitic crystal structure as imaged by the TEM [22]. However, this approach requires current to be passed through the contact region, and

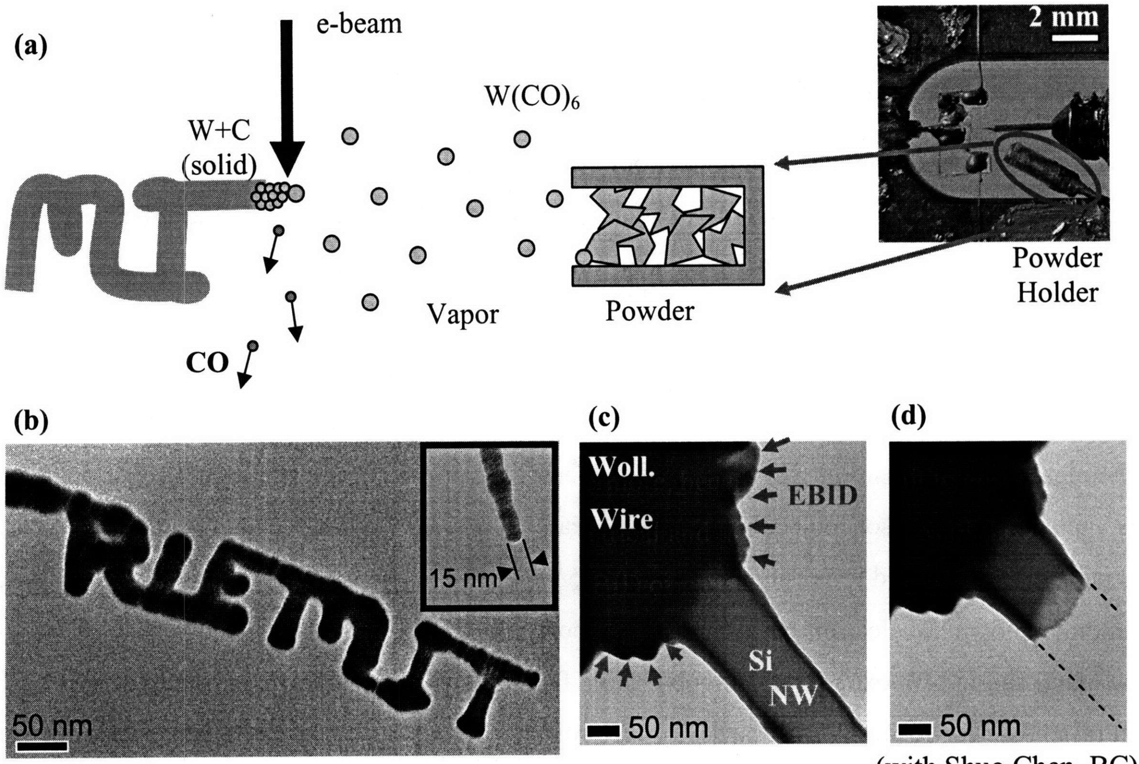

(with Shuo Chen, BC)

Figure 5-12. Electron-beam induced deposition (EBID) of tungsten inside a TEM. (a) Basic deposition process. W(CO)$_6$ powder is loaded in a small holder. The powder sublimes inside the TEM, and where the electron beam strikes the vapor, solid W+C deposits and CO vapor is pumped away. (b) An arbitrary pattern ("RLE MIT") written by manually rastering the TEM focus spot. Inset: Linewidths as small as 15 nm are possible. (c) EBID tungsten at the junction between a Wollaston wire and a silicon nanowire. (d) The same junction after pulling on the nanowire to failure. The EBID joint was stronger than the nanowire itself.

thus is limited to electrically-conducting NWs. Furthermore, because it is difficult to ensure that adequate carbon can be deposited in any given trial, and the electrical and thermal resistances of these contacts may still be larger than what can be achieved with metal, EBID of metals is preferred.

5.7.2 EBID of metals

Deposition of metals using an electron beam may be less well-known than deposition using an ion beam, but the materials and principles are similar. Common precursor materials include tungsten hexacarbonyl [W(CO)$_6$, CAS#14040-11-0], (trimethyl)methyl-cyclopentadienyl-platinum(IV) [(CH$_3$)$_3$(CH$_3$C$_5$H$_4$)Pt, CAS#94442-22-5], iron pentacarbonyl [Fe(CO)$_5$], and gold [PF$_3$AuCl]. These precursors are usually solid powders at standard temperature and pressure, but with a high vapor pressure [~10 Pa (~0.1 mm Hg) for W(CO)$_6$ at 300 K]. Literature precedents show that both SEMs and TEMs can be modified for EBID deposition, and include the creation of a variety of arbitrary shapes in two and three-dimensions [23-27]. Most prior work reports the addition of a separate chamber to store the precursor powder, along with valves, tubing, and possible temperature control to better manage the flow of precursor vapors. However, the work in this thesis follows a few other reports of a much simpler implementation, omitting the extra vacuum hardware and simply placing a small, open vessel of powder within a few millimeters of the sample, inside the TEM. The design of the powder holder is described in more detail below.

Using this system inside the Boston College TEM, we were able to deposit various tungsten shapes with feature sizes as small as 15 nm (Fig. 5-12). In a typical experiment, a charge of about 1 mm^3 of tungsten hexacarbonyl powder was located about 1-2 mm away from the sample. By focusing the electron beam down to a diameter of about 30-100 nm, tungsten deposition progressed at a fairly rapid rate of several nm/s. The location of the irradiated region was scanned manually using the beam shift controls, tracing out various patterns. This process of tracing out shapes could be automated in systems with scanning TEM (STEM) capability. The sublimation rate of the powder was such that the initial rapid deposition rate persisted for tens of minutes, then gradually slowed down to zero. In most cases deposition ceased after about 30-60 minutes. Energy-dispersive x-ray spectroscopy of the resulting deposits confirmed that they contain both tungsten and carbon. Electrical measurements of one deposit showed an ohmic *I-V* curve with a resistivity estimated very roughly as 9000 μΩ-cm, compared to about 5 μΩ-cm for bulk tungsten. Thermal measurements of another deposit suggested a thermal conductivity of the order of 1 W/mK, compared to about 170 W/mK for bulk tungsten.

5.7.3 Powder source for EBID of metals

Most traditional systems with EBID or FIB deposition have special vacuum hardware to control the flowrate of precursor vapors near the sample region. Because it was not practical to make such extensive modifications to the existing TEM, a much simpler system comprising a small, open container of powder was used. Initial trials used a piece of fine glass capillary tubing (about 300 μm inner diameter and a few mm long), coated with conducting epoxy to eliminate charging effects from the electron beam. However, this was difficult to load with powder, and the powder charge typically ran out within just a few minutes of inserting the powder container into the TEM. Stainless steel tubing and/or needles are available in a wide range of appropriate sizes, but unfortunately the various pieces tested all had enough residual magnetism to be a risk if inserted close to the TEM lenses. Heat treating the stainless steel reduced the magnetism significantly, but not enough to be judged safe for the TEM. Aluminum and brass are non-magnetic, but the smallest standard tubing available is 1.59 mm (1/16 inch) in outer diameter, too large for the allowed space. Finally, adequate powder holders were created by rolling small pieces of aluminum foil into cylinders or cones, and sealing with small amounts of silver epoxy as appropriate. A typical foil vessel is a cylinder 1 mm in diameter and 2 mm long, closed at one end. The other end is left open while filling with powder and then crimped partway shut, leaving an orifice about 100-200 μm diameter pointed towards the sample about 1-2 mm away. This foil technique has the advantages of ease of manufacture, arbitrary shapes and sizes, a very thin wall resulting in maximum powder volume, and good vacuum, electric, and magnetic properties. However, the foil vessels are difficult to seal well and can only be reused a few times before they fail.

5.8 Summary

This portion of the thesis presented a new type of probe for thermoelectric measurements of single nanowires and nanotubes, including thermal resistance, electrical resistance, and Seebeck coefficient. Because this probe is based on commercially-available Wollaston wire, it is easier to fabricate than previously-reported probes based on microfabrication. The new probe also has the potential to be more than an order of magnitude more sensitive than the previously reported probes. Detailed thermal and mechanical design calculations also reveal some limitations of the new probe, including: the nonlinear relationship between temperature rise and nanowire thermal resistance; the need to pretension the Wollaston wire to avoid problems from thermal vibrations and thermal expansion; and the likely impact of thermal contact and spreading resistances. The Wollaston wire probe has been implemented inside of a high-resolution TEM with a built-in STM manipulator. This introduces the challenges of high vacuum and strong magnetic fields, but brings the benefits of atomic-level imaging and rapid sample selection. Preliminary experiments have measured the thermal resistance, electrical resistance, and Seebeck coefficient of various samples including a carbon nanotube and ZnO nanobelt, but in most cases the data is qualitative rather than quantitative due to the large and uncertain thermal contact resistance. To improve the contacts the TEM sample holder was modified to facilitate electron-beam induced deposition (EBID) of tungsten from an organo-metallic precursor powder, similar to approaches reported previously for the measurement probes based on microfabrication. Our preliminary attempts at EBID succeeded in patterning arbitrary two-dimensional shapes with linewidths as small as 15 nm. Local EBID at either end of a nanowire/nanotube has been shown to greatly increase the contact area, and in fact to be mechanically stronger than the nanowire itself.

Future work on this project will combine the EBID technique with the thermoelectric measurements to overcome the problem of thermal contact resistance. Then this project will move into its most productive phase: the high-throughput measurement of thermoelectric properties of many different nanowires and nanotubes. One early goal will be to measure the thermal resistance of a multi-walled carbon nanotube as a function of the number of walls, by using electric current to controllably burn off the outermost walls one at a time.

5.9 References

1. P. Kim, L. Shi, A. Majumdar, and P. L. McEuen, *Phys. Rev. Lett.* **87**, 215502 (2001).
2. L. Shi, D. Li, C. Yu, W. Jang, D. Kim, Z. Yao, P. Kim, and A. Majumdar, *J. Heat Trans.* **125**, 881 (2003).
3. L. Shi, Q. Hao, C. Yu, N. Mingo, X. Kong, and Z. L. Wang, *Appl. Phys. Lett.* **84**, 2638 (2004).
4. C. Yu, L. Shi, Z. Yao, D. Li, and A. Majumdar, *Nano Lett.* **5**, 1842 (2005).
5. D. Li, Y. Wu, P. Kim, L. Shi, P. Yang, and A. Majumdar, *Appl. Phys. Lett.*, **83**, 2934 (2003).
6. D. Li, Y. Wu, R. Fan, P. Yang, and A. Majumdar, *Appl. Phys. Lett.*, **83**, 3186 (2003).
7. M. Fujii, X. Zhang, H. Xie, H. Ago, K. Takahashi, T. Ikuta, H. Abe, and T. Shimizu, *Phys. Rev. Lett.* **95**, 065502 (2005).
8. A. E. Perry, *Hot Wire Anemometry* (Oxford, 1982).
9. V. A. Sandborn, *Resistance Temperature Transducers* (Metrology Press, Colorado, 1972).
10. C. G. Lomas, *Fundamentals of Hot Wire Anemometry* (Cambridge University Press, 1986).
11. H. H. Lowell, *NACA Technical Note 2117*, NACA, July 1950.
12. A. C. Sacharoff, R. M. Westervelt, and J. Bevk, *Phys. Rev. B* **26**, 5976 (1982).
13. L. R. Holland and R. C. Smith, *J. Appl. Phys.* **37**, 4528 (1966).
14. D. G. Cahill, W. K. Ford, K. E. Goodson, G. D. Mahan, A. Majumdar, H. J. Maris, R. Merlin, and S. R. Phillpot, *J. Appl. Phys.* **93** (Appl. Phys. Reviews), 793 (2003).
15. Incropera & Dewitt, *Fundamentals of Heat and Mass Transfer* (Wiley, 2002).
16. G. Chen, *J. Heat. Trans.* **118**, 539 (1996).
17. J. E. Shigley, *Mechanical Engineering Design* (McGraw Hill, 1986).
18. C. Kittel and H. Kroemer, *Thermal Physics* (W. H. Freeman, 1980).
19. M. M. J. Treacy, T. W. Ebbesen, and J. M. Gibson, *Nature* **381**, 678 (1996).
20. A. Krishnan, E. Dujardin, T. W. Ebbesen, P. N. Yianilos, and M. M. J. Treacy, *Phys. Rev. B* **58**, 14013 (1998).
21. T. C. Harman, *J. Appl. Phys.* **30**, 1351 (1959).
22. J. Y. Huang, S. Chen, Z. F. Ren, G. Chen, and M. S. Dresselhaus, to appear in *Nano Lett.* (2006).
23. H. W. P. Koops, R. Weiel, D. P. Kern, and T. H. Baum, *J. Vac. Sci. Technol. B* **6**, 477 (1988).
24. H. W. P. Koops, J. Kretz, M. Rudolph, M. Weber, G. Dahm, and K. L. Lee, *Jpn. J. Appl. Phys.* **33**, 7099 (1994).
25. I. Utke, P. Hoffman, B. Dwir, K. Leifer, E. Kapon, and P. Doppelt, *J. Vac. Sci. Technol. B*, **18**, 3168 (2000).

26. Z. Q. Liu, K. Mitsuishi, and K. Furuya, *J. Appl. Phys.* **96**, 619 (2004).

27. M. Takeguchi, M. Shimojo, K. Mitsuishi, M. Tanaka, and K. Furuya, *Superlatt. Microstruct.* **36**, 255 (2004).

Chapter 6: Summary and Future Directions

6.1 Summary

This thesis has made several contributions towards better modeling and measurements of the thermal properties of nanowires and nanotubes, summarized below.

Chapter 2 dealt with phonons as waves, and the quantum effects of confining them in nanostructures. The traditional Debye-Einstein model for three-dimensional phonons was generalized to lower dimensions, resulting in a simple model for the specific heat with few parameters, all of which can be extracted from bulk properties. To test this model the specific heat of TiO_2 (anatase) nanotubes with 2.6 nm wall thickness was measured down to 1.4 K. Although the interpretation of the experimental data was complicated by possible contamination of the nanotubes by ice, overall the model and experiment are in good agreement above about 2.5 K, including enhancements in the nanotube specific heat by more than a factor of 3 compared to bulk. These are the first specific heat measurements on non-carbon nanotubes. The most important conclusion of this chapter was to confirm that quantum / wave effects on thermal properties can be neglected as long as the characteristic thermal wavelength is smaller than the size of the nanostructure. The phonon wavelength at room temperature is only about 1-2 nm for most practical materials, suggesting that quantum / wave effects on the thermal conductivity and specific heat may be neglected at room temperature and above for most nanostructures larger than about 5 nm. Although a few individual phonon modes may still be affected by quantum confinement, these effects are averaged out because the thermal conductivity and specific heat are based on an integration over all of the modes.

Chapter 3 began by analyzing the transition from quantum to classical behavior, considering both nanostructure size and roughness. Kinetic theory and Matthiessen's rule were then used to model the reductions in thermal conductivity due to boundary scattering in nanowires and superlattice nanowires. With no adjustable parameters, the model agrees well with available thermal conductivity data for nanowires of diameters ranging from about 60-115 nm [1], including thermal conductivities 1000 times smaller than bulk.

Considerable care in the modeling was necessary to give good results with minimal complexity. For example, we approximated the experimentally-determined phonon dispersion relations with the Born-von Karman model rather than the Debye model. Although both models use the same input parameters, namely sound velocity and atomic number density, the Born-von Karman model is much better than the Debye model at capturing the high-frequency rolloff in the dispersion relation. As a result, when boundary scattering is dominant, the Born-von Karman model gives much better results for high-temperature thermal conductivity, typically within 10-20% of experimental values. The Debye model, on the other hand, overpredicts the same experimental thermal conductivity by a factor of 2 or more [2]. This chapter also illustrated the importance of accounting for the frequency dependence of the bulk mean free paths. Neglecting the frequency dependence can also lead to large overpredictions of the experimentally measured thermal conductivity.

Chapter 3 also established the concept of a distribution function for the thermal conductivity per unit mean free path. These distributions depict the full range of mean free paths that are important for carrying the heat in bulk and in nanostructures. Long mean free paths play a more important role in heat transfer than may be commonly realized. For example, in bulk silicon at room temperature it is important to consider mean free paths ranging from about 90 nm up to about 12 μm. This range spans over 2 orders of magnitude, and includes mean free paths that are much longer than the naive estimate of about 5 nm or the traditional average value of about 200-300 nm.

Chapter 4 improved and extended the existing "3ω" methods for measurements of thermal properties. In the traditional 3ω methods, an electrical current at frequency ω is used to drive a resistive heater. The resulting voltage signal includes a small contribution at the third harmonic, 3ω, which can be related to the thermal properties of the system. Using both analysis and experiments, this thesis showed that the thermal properties can also be related to the voltages at the second harmonic (2ω) and first harmonic (1ω). Additional analysis and experiments showed that a simple correction factor can be used to reconcile the widespread current-source analyses with the more common voltage-source experiments. This correction appears to have been ignored previously in the literature. Although the 3ω method is still recommended for most situations, the newly identified 1ω method should be simpler to implement, and may be advantageous for studying the thermal dynamics of nanoscale systems.

Chapter 5 presented the detailed thermal and mechanical design of a new probe to measure the thermoelectric properties of individual nanowires and nanotubes inside a TEM. The probe, based on comercially-available Wollaston wire, is easier to fabricate and potentially more sensitive than the microfabricated measurement platforms previously reported in the literature. By analyzing various signals, the probe can measure the thermal conductivity, electrical conductivity, and Seebeck coefficient. Although the preliminary thermoelectric data obtained in this thesis proves the concept, it is not quantitative because of the large and non-repeatable thermal contact resistances at the ends of the nanowire or nanotube. To overcome this problem the TEM sample holder is being modified for local electron beam-induced deposition of metals from a metallorganic precursor vapor such as tungsten carbonyl. By manually scanning the electron beam, this technique was used to pattern arbitrary shapes with line widths as small as 15 nm. The metal bonds have proven to give stronger, more reliable contacts than our previous approach using amorphous carbon.

6.2 Future Directions

This thesis points towards several research directions which may be worthy of further effort.

(a) Thermoelectric measurements of single nanowires and nanotubes

The Wollaston wire probe described in Chapter 5 is nearly complete. The final step is to incorporate the local metal deposition process with the thermoelectric measurements. It is hoped that this will then enable high-throughput thermoelectric measurements of a wide range of nanowires and nanotubes. This is important to build up a broader set of experimental data than is currently available in the literature. One interesting experiment will be to measure the thermal conductivity of a multi-walled carbon nanotube as a function of the number of walls. It will also be important to study the effect of making contacts at the end of the nanotube compared to the nanotube sidewall. Another important objective is to measure ZT for various thermoelectric nanowires, with the hope of observing the largest ZT ever reported.

(b) Thermal conductivity distribution functions

The distribution functions for the thermal conductivity per unit mean free path presented in Chapter 3 made certain assumptions about the dispersion relation and phonon scattering laws, but other assumptions are possible. It would be interesting to repeat this analysis with different assumptions, to learn how sensitive the distribution functions are to the input assumptions. It would also be interesting to compare these analytical curves with some analogous distribution functions obtained from molecular dynamics [3].

(c) Thermal conductivity of silicon nanowires below 40 nm diameter

Although our classical model for nanowire thermal conductivity is in good agreement with available experiments for diameters above 50 nm and temperatures down to about 20 K, there are large disagreements between the model and the only available measurements of smaller Si nanowires (37 and 22 nm) [1]. The data reported for the 22 nm diameter nanowire in particular show a thermal conductivity dependence that is linearly proportional to temperature T, whereas in our model the conductivity is proportional to T^3 in this temperature range. The usual interpretation of this exponent is that it tracks the low-temperature specific heat; however, the work in Chapter 2 of this thesis showed that the specific heat of a 22 nm Si nanowire should clearly be in the T^3 regime over this range of temperatures. To the best of my knowledge no other theory in the literature has been able to explain the T^1 trend either for these nanowires. Therefore, we can conclude that the thermal conductivity of Si nanowires below about 40 nm is still not well understood. More experimental data are necessary, and it is hoped that the Wollaston wire probe will be able to contribute here for nanowires made of silicon as well as many other material systems. If the T^1 trend is confirmed experimentally, then several fundamental aspects of the modeling will have to be reconsidered.

6.3 References

1. D. Li, Y. Wu, P. Kim, L. Shi, P. Yang, and A. Majumdar, *Appl. Phys. Lett.* **83**, 2934 (2003).
2. C. Dames and G. Chen, *J. Appl. Phys.*, **95**, 682 (2004).
3. A. S. Henry and Gang Chen, submitted (2006).